ADDIS ABABA UNIVERSITY
SCHOOL OF GRADUATE STUDIES
SCHOOL OF EARTH SCIENCES

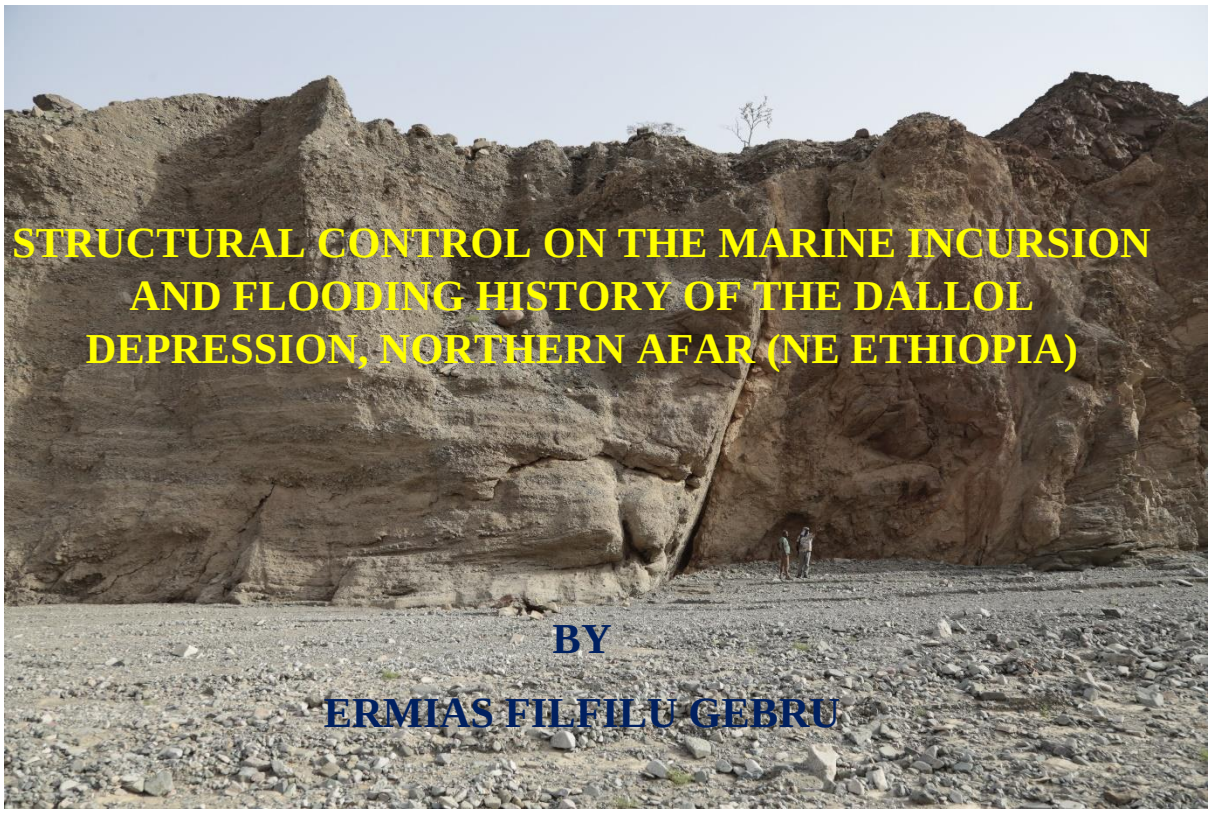

STRUCTURAL CONTROL ON THE MARINE INCURSION AND FLOODING HISTORY OF THE DALLOL DEPRESSION, NORTHERN AFAR (NE ETHIOPIA)

BY

ERMIAS FILFILU GEBRU

A thesis submitted to the School of Graduate Studies of Addis Ababa University in partial fulfilment of the requirements for the degree of Master of Science in Earth Sciences (Structural Geology)

December 2017
Addis Ababa, Ethiopia

ADDIS ABABA UNIVERSITY
SCHOOL OF GRADUATE STUDIES
SCHOOL OF EARTH SCIENCES

STRUCTURAL CONTROL ON THE MARINE INCURSION AND FLOODING HISTORY OF THE DALLOL DEPRESSION, NORTHERN AFAR (NORTHEAST ETHIOPIA)

BY
ERMIAS FILFILU GEBRU

ADVISORS: TESFAYE KIDANE (Prof.)

BINYAM TESFAW (Dr.)

A thesis submitted to the School of Graduate Studies of Addis Ababa University in partial fulfilment of the requirements for the degree of Master of Science in Earth Sciences (Structural Geology)

December 2017
Addis Ababa, Ethiopia

Addis Ababa University
School of Graduate Studies

This is to certify that the thesis prepared by **Ermias Filfilu**, entitled: *Structural Control on the Marine Incursion and Flooding History of the Dallol Depression, Northern Afar (NE Ethiopia)* and submitted in partial fulfilment of the requirement for the Degree of Master of Science (Structural Geology) complies with the regulations of the University and meets the accepted standards with respect to originality and quality.

Signed by the Examining Committee:

Examiner Dr. Bekele Abebe Signature _____ Date _____

Examiner Prof. Gezahegn Yirgu Signature _____ Date _____

Advisor Prof. Tesfaye Kidane Signature _____ Date _____

Co-Advisor Dr. Binyam Tesfaw Signature _____ Date _____

Declaration of Originality

I hereby declare that the thesis "*Structural Control on the Marine Incursion and Flooding History of the Dallol Depression, Northern Afar (Northeast Ethiopia)"* is my original master's degree work under the supervision of Prof. Tesfaye Kidane and Dr. Binyam Tesfaw and has not been presented to any other university or institution for the award of any degree or diploma. All sources and materials used for the thesis have been duly acknowledged.

Ermias Filfilu Gebru _____ _____

Signature Date

This is to certify that the above declaration made by the candidate is correct to the best of our knowledge and it has been submitted for examination with our approval as university advisors.

Prof. Tesfaye Kidane _____ _____

(Advisor) Signature Date

Dr Binyam Tesfaw _____ _____

(Co-Advisor) Signature Date

ABSTRACT

The present study area is situated in the tectonically active Dallol Depression, northern sector of the Danakil Depression, NE of Ethiopia. The main objective of the present study was to evaluate structural control on the Red Sea incursion and flooding history of the Dallol Depression along with production of geological map of the region. To accomplish the so set objective, fieldwork, remote sensing and seismic investigations (from secondary source) were carried out. Structural analysis, band combination and ratio enhancement techniques and DEM analysis enabled the discrimination of different lithologies and delineation of regional structures. Produced geologic map revealed that the northern Danakil Depression and the western margin may represent the complete sequence of rocks spanning from the Neoproterozoic to the Holocene and the dominant structural trend in the study area is NNW followed by N-S and NE trending structures. The study enabled identification of basement rocks, limestone, sandstone, basalt, gypsum and associated coral reefs, alluvial sediments, conglomerate and salt formation. Kinematic analysis of fault-slip data collected from the field indicate NE-SW extension direction coinciding with the regional extension direction in which oblique-slip sense of movement with dominant dip-slip component is exhibited. Dynamic analysis of conjugate fault sets depict that the tensional stress represented by σ_3 is parallel to the overall extension direction across the Red Sea. Observation from DEM and differential GPS measurements showed that the western margin of the Depression has been affected by faulting which lead to the desiccation of the Dallol Depression from the Red Sea in combination sea level drop.

Key words: Dallol Depression; Marine Incursion; Remote Sensing; Enhancement; DEM; Seismic

ACKNOWLEDGEMENT

No research is completed successfully without the support of others and this is no exception. I am greatly indebted to Addis Ababa University for providing financial support to carry out this research. For the invaluable academic support, an enormous thank you is owed to my Advisor Prof. Tesfaye Kidane and my Co-Advisor Dr. Binyam Tesfaw. Thanks, are extended to Dr. Seifu Kebede, former Head of the School of Earth Sciences, and Dr. Balemwal Atnafu, Head of the School of Earth Sciences, and other members of the School for their continuous vital inspiration. This research has also benefited from the research stay at the University of Fribourg, Department of Geosciences through the Ethio-Swiss collaborative research team under the project SERENA (SEdimentary REcord of Northern Afar). I would like to acknowledge the Afar Consortium members Prof. Anneleen Foubert and Jean-Charles Schaegis for their comments on some portion of the manuscript. I wish to sincerely thank the administrators of the Afar National Regional State and the community in Dallol and Hamadela area for their cooperation during the field work. Special thanks are extended to Circum Minerals ltd. Bada Main Camp, potash company where field camp was at, for their support and hospitality. I would like to thank Potash Companies (Allana and Circum) in the region for providing seismic data and their accompanying reports through the cooperation of Ministry of Mines. Appreciation also go to Tadesse Berhanu for providing inaccessible literatures. Thanks are due to friends especially to Samuel Getachew and Surafel Berhanu who supported me with the preparation of the maps and the field photo illustrator sketches respectively. I also acknowledge the help from Selamawit Tadesse and Amdemichael Zafu.

TABLE OF CONTENTS

LIST OF FIGURES

LIST OF TABLES

CHAPTER 1

INTRODUCTION

1.1 Background

The study area belongs to the north sector (Samson Tesfaye et al., 2003; Miruts Hagos, 2010; Warren, 2016) of the Afar Depression, which covers an area of about 200,000 km^2 (Alebachew Beyene & Abdelsalam, 2005; Bosworth et al., 2005). Most of the Danakil Depression was unexplored scientifically until as recently as the 1960s owing to combination of a hostile, hot-and-arid climate and political problems tied to Ethio-Eritrea territory (Clynne et al., 2005; Kalb, 2001; Yasin Mohammed, 2008) that there were only few investigations in the north sector of the Afar Depression prior to the 1960s.

Afar is one of the only two places on the planet earth where spreading axes occur above the sea level; the other being in Iceland. It is a region where you can witness the violent, once-in-a-generation separation of tectonic plates that is responsible for creating new oceans. The region is one of the two world most gifted areas for geothermal energy development; the other being in Iceland. It displays favourable conditions: shallow energy sources, fractured aquifers, and hydrothermal reservoirs for geothermal energy development (Varet et al., 2012; Varet, 2010). Varet (2006) described the region as "the future Gulf region for geothermal energy". The potash deposit which occur within the evaporite sequence, which is essentially confined to the areas below the present sea level, of the Danakil Depression also characterizes the Afar Region. This region is famous for being the cradle of mankind as it was here that various human fossils were discovered: Ardi (Ardipithecus ramidus) and Lucy and Selam (Australopithecus afarensis) (White et al., 1994; Johanson & Taieb, 1976; Zeresenay Alemseged et al., 2005). It is one of the few localities worldwide where one may study the processes of microplate formation on land (Eagles et al., 2002). Fifty-Nine Holocene volcanoes are currently known in Ethiopia, of which just over half lie in the Afar Depression (Siebert et al., 2010 as cited in Vye-Brown et al., 2016) Afar is also home to one of the four long-lived lava lakes, Erta 'Ale, existing across the world; others are Erebus (Antarctica), Nyiragongo (DR Congo) and Ambrym (Vanuatu) (Field et al., 2012) which offers a unique opportunity to study magma convection (Jones et al., 2006). It is in this region the deepest sub-aerial Depression (i.e. the Dallol Depression) on Earth exists (Miruts Hagos, 2010) where continental breakup is occurring above arguably the hottest mantle on Earth (Bastow et al., 2008).

The first systematic geological work in the Danakil Depression was started around late 1960´s (Barberi et al., 1973; Gibson & Tazieff, 1970). This was followed by detailed geological description of salt formation (Holwerda & Hutchinson, 1968; Hutchinson & Engles, 1970) attached to Dallol mine. According to Barberi et al. (1973) further prospecting for salt was carried out by a German team later in 1970 which produced geologic map by Bannert and others. In 1973 the Italian CNR (Consiglio Nazionale delle Ricerche) and the French CNRS (Centre National de la Recherche Scientifique), Afar Team collaboration produced geological map of the northern Afar at a scale of 1:500, 000 (see Appendix G). This collaboration resulted in publication of about 60 detailed and general papers during the period 1968-1973 by members of the expedition. These articles deal with various aspects including tectonics, petrology, volcanology, mineralogy, geochemistry of rocks, waters, sediments and fossils, isotopic geology and some geophysical aspects.

Since then many of the publications mainly focus on either the salt formation (e.g., Talbot, 2008) specifically or tectonics (e.g., Alebachew Beyene & Abdelsalam, 2005; Samson Tesfaye et al., 2003; Redfield et al., 2003), remote sensing (e.g., Hayward & Ebinger, 1996; Thurmond et al., 2006) and seismicity (Hofstetter & Beyth, 2003) of the whole Afar Depression at a regional scale or part of the present study area (Nobile et al., 2012) and the Danakil block (Collet et al., 2000; Eagles et al., 2002) with less extensive field investigation. Apart from these there were also geothermal investigations of the north sector of the depression (UNDP, 1973; Varet, 2010; Varet, 2012; Franzson et al., 2015) in recent times. Only recently has fieldwork been possible again, allowing researchers to conduct detailed investigations within the Afar Depression and understand its contribution to the volcano-tectonic history of the region as a whole (Atalay Ayele et al., 2009; Barisin et al., 2009; Manahloh Belachew et al., 2011; 2013; Ferguson et al., 2013; Wright et al., 2006, 2012; Darrah et al., 2013; Miruts Hagos, 2010) and most recently Balemwal Atnafu and others (2015) studied the intergrowth of coral and algae (coral reefs) of this region.

1.2 Problem Statement

Danakil Depression was once connected with the Red Sea evidenced by the presence of marine deposits within the Depression (Bonatti et al., 1971; Balemwal Atnafu et al., 2015). The depression was flooded at least two times by the Rea Sea during 80-130 ka (MIS 5; Marine Isotopic Stage 5) and 191-243 ka (MIS 7) (Foubert et al., 2015; Balemwal Atnafu

et al., 2015; Jaramillo-Vogel et al., 2015; Schaegis et al., 2016). According to two different studies the final separation of the Depression with the Red Sea took place 32ka (Bonatti et al., 1971) or 60 to 70ka (Barberi et al. 1973) ago. Some researchers (Bonatti et al., 1971; Barberi et al., 1973; Beyth (1994) (as cited in Duffield et al., 1997)) believe that Alid volcano in the north-western part of the Danakil Depression acted as dam that blocked the Red Sea from the Danakil Depression as in the case everywhere in Afar where young volcanic centres prevent marine waters from flooding the region (Corti et al., 2015).

However preliminary fieldwork has shown that the Danakil Depression could have been closed step-wise and that different pathways could be inferred for flooding (Foubert et al., 2015). Foubert et al. (2015) add to this argument the elevation variation of the synchronous marine units from -40 m to +170 m evidencing active differential subsidence. Sea level change in the Red Sea can also be put forward for the closure of the connection between the Danakil Depression and the Red Sea as in the alternate periods of flooding and evaporation in the Red Sea and the opening and closing of connections with the Mediterranean and Indian Ocean (Braithwaite, 1987 as cited in Klaus, 2015). Nevertheless, even though generally, over a few decades, sea levels change more rapidly than land levels the land movements are increasingly important and eventually dominant over centuries and millennia. Tectonic movements influence these land movements (Pugh & Abualnaja, 2015) specially in tectonically active areas like the Danakil Depression and the apparent sea-level record may not be free of tectonic complications.

It is known that the western margin of Danakil basin has been affected by repeated normal faulting (e.g., Holwerda & Hutchinson, 1968). Besides faulting along with plate stretching account for a higher proportion of lithospheric strain in the Danakil Depression (Keir et al., 2013). Hence the final closure of the Danakil Depression with the Red Sea and the pathways of the marine ingression might be determined by the syn-sedimentary tectonics. Accordingly, this research attempts to evaluate the structural control of the separation of the Depression with the Red Sea. To this end field work, remote sensing and seismic interpretation are employed.

1.3 Description of the Study Area

The study area is situated in north-eastern Ethiopia about 950 km away from the capital city Addis Ababa. It is found in the Afar National Regional State of Ethiopia bounded by 604000 m E to 642000 m E Easting and 1555000 m N to 1610000 m N Northing in WGS UTM zone 37N (see fig. 1.1 below). The Ethio-Eritrea Border bound it in the north direction. On the west side, it is separated from the NW Ethiopian Plateau by flat topography covered with alluvial sediments and a stream which runs N-S. Salt plain bound it on the east side (see fig. 1.3). The study area has an approximate total areal coverage of 1890 km^2 within partly the Dallol Woreda and partly the Berhale Woreda of the Afar National Regional State of Ethiopia (CSA, 2007).

The province can be accessed through a vehicle route from Addis Ababa-Mekele-Agula-Berhale-Musley-Badda. The way from Addis Ababa-Mekele-Agula is 799 km long asphalt road. From Agula town turn to the east and follow the newly constructed Agula-Berhale-Musley asphalt road which is 151 km long. Then after 37 km off-road from Musley town, Badda village, where the present study camp was situated at, can be reached.

According to Waltham (2005) 'hostile environment' is an expression tailor-made for the Afar Depression. Dallol currently holds the official record high average temperature for an inhabited location on Earth, where an average annual temperature of 35°C (96°F) was recorded between the years 1960 and 1966 (Pedgley, 1967; see table 1.1 below). The region is an awful, extremely hot and barren desert covered by fresh basaltic lavas and sediments.

In winter, daily temperatures are between 33 and 44°C; summer commonly reaches shade temperatures of >50°C in the northern part of the depression (Dallol Depression). Rainfall is very low in the depression itself where average circa 100 mm/year; 50 mm in Dallol (Varet et al., 2012; Allana Potash, 2012), which is even lower than the lowest value in Ethiopia (Elidar, 153 mm/year) which is measured by rain gauge located in the Afar Triangle at an elevation of 423 m (Fazzini et al., 2015). Relative humidity in the region ranges from 60 % to 90 % throughout the year (Circum, 2015). Cloudiness is another basic climatic parameter apart from rainfall and temperature. Ethiopia is the country with

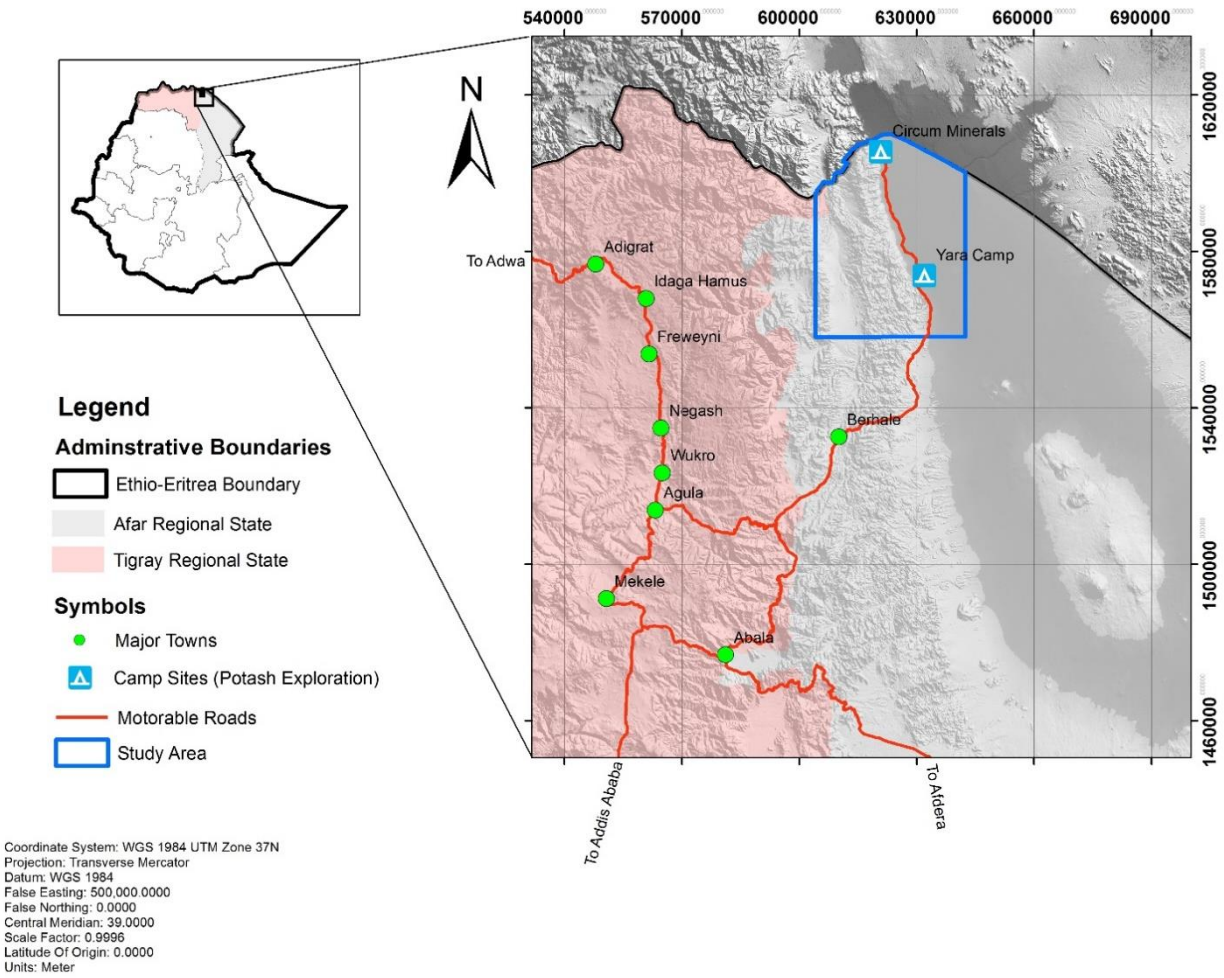

Fig. 1.1 location map draped on the DEM of the study area

the most extensive cloudiness in Africa and in Danakil Depression cloudiness is almost exceptional phenomenon. The Depression has Aridity index (A_i = p/PET, where p is annual precipitation and PET is potential evapotranspiration) less than 0.65 typical of dry lands. Hence the region is considered as desertification prone area (Fazzini et al., 2015 and references therein).

Table 1.1 historic temperature data for Dallol area (modified from Pedgley, 1967)

Month	Jan	Feb	Mar	Apr	May	Jun	Jul	Aug	Sep	Oct	Nov	Dec	Year
Record high (°C)	46	46	46	45	45	45	46	47	46	46	45	46	47
Average high (°C)	40.9	40.5	40.4	40.8	40.3	40.7	40.7	40.1	40.1	40.2	40.3	40.9	40.49
Daily mean (°C)	35.6	35.6	35.8	35.6	35	35.9	35.7	35.9	35.9	35.9	35.1	35	35.58
Average low (°C)	30.1	30.2	30.4	30.8	30.6	30.1	30.7	30.7	30.7	30.6	30.9	30.2	30.5
Record low (°C)	24	24	24	24	24	23	23	23	23	24	24	24	23
% humidity	88	89	90	85	85	80	80	80	81	83	82	85	84.6

Table 1.2 recent temperature data of Dallol area for the year 2015 and 2016 (http://accuweather.com/en/et/dalol/126842)

Months	Average Max. (°C)		Maximum (°C)		Average Min. (°C)		Minimum (°C)	
	2015	2016	2015	2016	2015	2016	2015	2016
Jan	28	28	28	28	21	21	21	21
Feb	28.43	28.45	29	29	20.53	20.55	20	20
Mar	30.13	30.13	31	31	22.29	22.29	21	21
Apr	32.4	32.4	34	34	24.03	24.03	23	23
May	34.52	34.52	35	35	25.61	25.61	25	25
Jun	35.2	35.16	36	36	27.4	27.4	27	27
Jul	36	36	36	36	28.29	28.29	28	28
Aug	35.9	35.63	36	36	28.26	28.25	28	28
Sep	34.93	34.07	35	35	27.27	26.73	26	26
Oct	33.19	33.22	34	34	25.45	25.48	24	24
Nov	30.53	30.53	32	32	23.3	23.3	22	22
Dec	28.61	29.77	29	33	21.71	22.22	21	19

The Danakil Depression, a ~200–220 km-long, relatively narrow (50–150 km-wide) basin (Corti et al., 2015), dominates the morphology of the northern Afar Depression. The morphology of the Depression is clearly controlled by active tectonics and young volcanism (Skovitina et al., 2012). Danakil Depression is physiographically very clearly defined, low lying, roughly triangular-shaped area situated within Ethiopia at the southern end of the Red Sea (Gibson & Tazieff, 1970). It is bounded on all its sides by upland topographic features (see

fig. 1.3): Ethiopian Plateau, Somali Plateau, and Danakil Alps. The N-S trending, 700-km long NW Ethiopian Plateau, the E-W trending 350-km long Somali Plateau and the NNW-SSE trending Danakil Alps bound the depression in the west, south and northeast respectively (Abbate et al., 2015; Barberi et al., 1973; Allana Potash, 2012; Corti et al., 2015). These uplands constitute the shoulder of the depression.

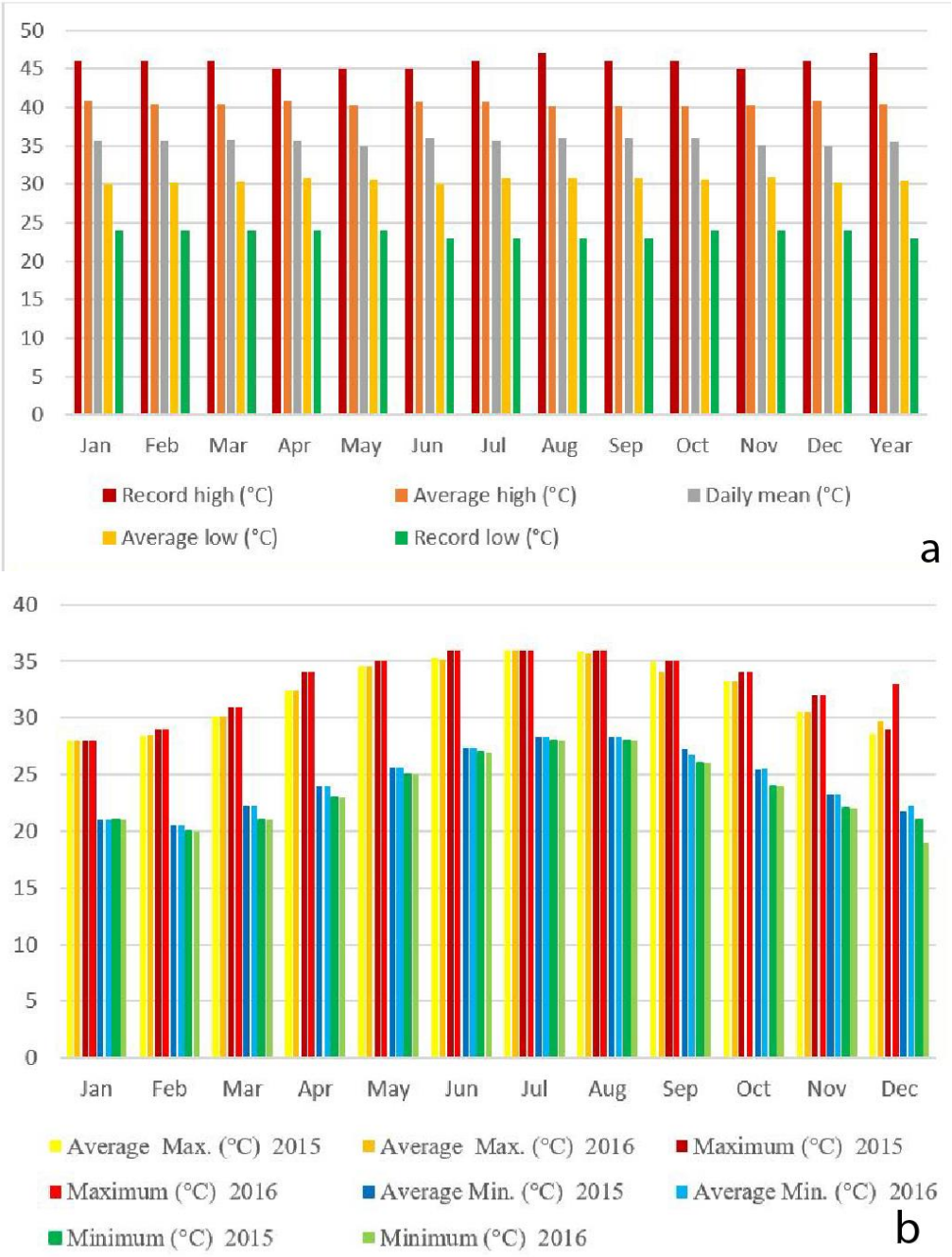

Fig.1.2 Temperature data for the Dallol area (a) historical (modified from Pedgley, 1967) and (b) Recent for the last two years: 2015 and 2016 (http://www.accuweather.com/en/et/dalol/126842)

The Ethiopian escarpment extends north into Eritrea and closes the Afar Depression against the Danakil Alps at the Gulf of Zula (Alebachew Beyene & Abdelsalam, 2005). Elevation in the Afar Depression vary from over 3000 m above sea level in the Ethiopian Plateau to 120 m below sea level in the Dallol area salt flats (Holwerda & Hutchinson, 1968; Franzson et al., 2015). The Danakil Alps reaches an elevation of 1,300 m in its northern portion and more than 2,000 m to the south (Abbate et al., 2015).

Geomorphic features characteristics of the study area and its surroundings are volcanoes, marginal basins, alluvial fans, ridges, salt plains and lake. Two volcanoes: Maraho volcano (see fig. 1.4a) and Dallol volcano are found within the study area. Dallol volcano is elliptical in shape and rises gently to 60 m from the salt plain (48 m b.s.l.) and has a longer diameter of 5km and a summit crater (ca. 100m diameter) (Tadiwos Chernet, 2012). The marginal basins are developed in the western margin of the study area adjacent to the Ethiopian plateau. The alluvial fans (see fig. 1.4b below), common geomorphic features in desert environment like the Afar Depression, are formed where the gradients of streams from the NW Ethiopian Plateau drops as it emerges onto the salt plain eastward depositing a large portion of its sediment load. Ridges in the study area (see fig. 1.4c below) rarely exceed 1000 m and are prevailing in the west side of the study area. More than one third of the vicinity is covered by salt plain (see fig. 1.4d & e). Lake Assale is found some 4 km on the SE direction of the study locale. The inflowing ground water from the highlands into the Depression through solution process within the evaporites resulted in the high salinity level of the lake. Hence Lake Assale (fig. 1.4j) is the saltiest lake in Northern Afar (Williams, 2016). Salt pillars (see fig. 1.4f below), hot acid pools (or lakes fig 1.4g), mud craters (see fig. 1.4h), and gypsum canyons (see fig. 1.4i) are other geomorphic features within the present study area. Close to Mount Dallol there are several hot springs with high salinity.

Danakil river basin has an area of 74,002 km^2, which covers Tigray, Amhara and Afar regional states. The basin has no major river draining out of it (Seleshi Bekele et al., 2007). The Danakil river systems are all ephemeral and drain endorheic basins. None of these rivers, in fact, has an outlet into either the Mediterranean Sea or the Indian Ocean unlike the other

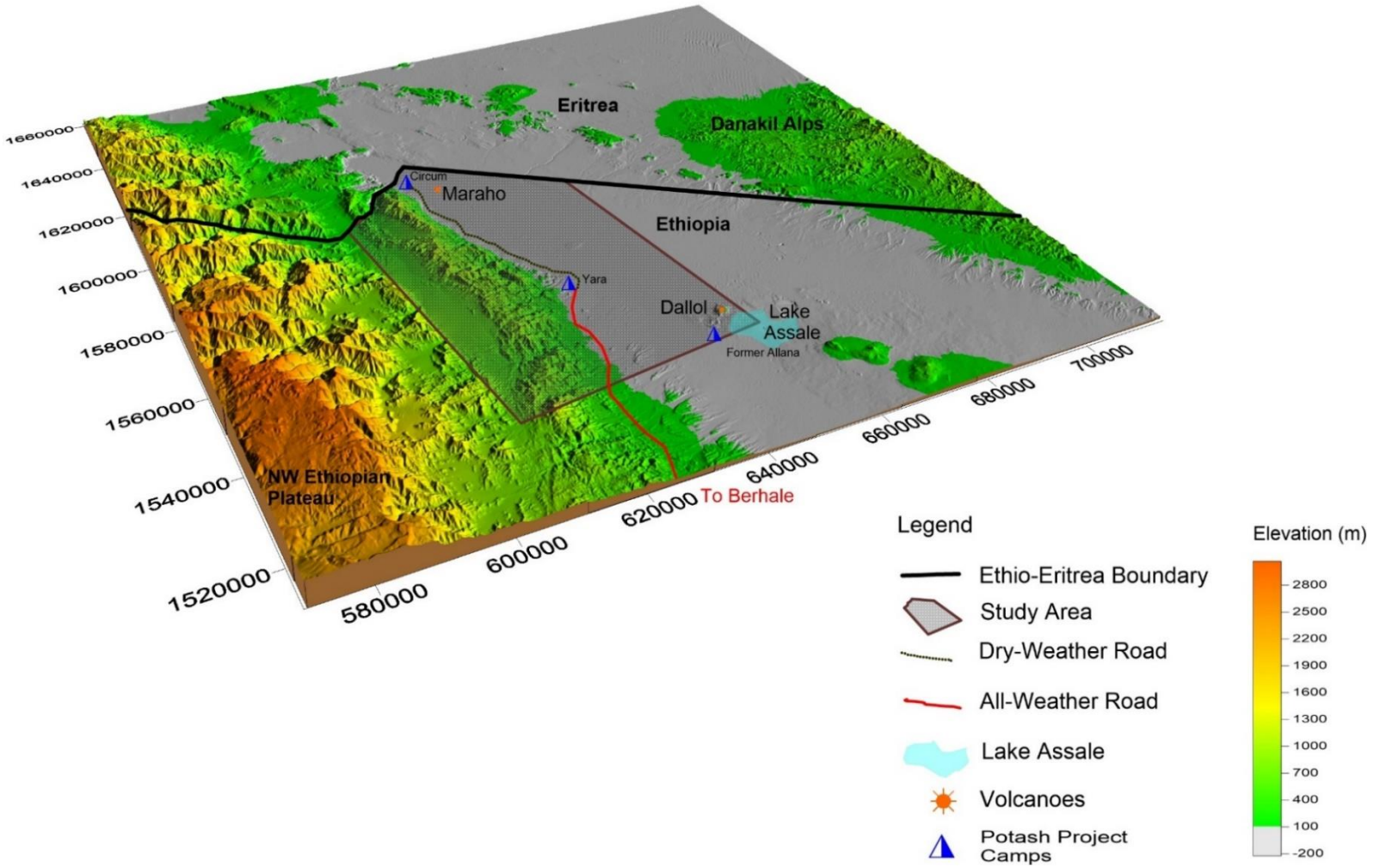

Fig. 1.3 physiographic map of the study area

larger rivers of Ethiopia. They outflow into the large lakes on the rift floor. The base level of a very few of them are small lakes such as Afdera and Assal, whereas many of Danakil rivers form terminal fans or distributary systems on the borders or on the floor of structural basins (Billi et al., 2015). The main water flow into the area is the Awash River (the second longest river of Ethiopia (Seleshi Bekele et al., 2007)), which flows north-eastward through southern Afar where it ends in a chain of interconnected lakes, the last of which is Lake Abhe (Corti et al., 2015; Billi et al., 2015). These saline lakes contain almost the only water in the region (Corti et al., 2015).

According to Central Statistical Agency (CSA) of Ethiopia as of July 1, 2015, the total population of the Afar National Regional State is 1,723,000 of which 97, 745 is in the Dallol Woreda to which the present study area belongs. From this 53,628 of them are males and 44,117 are females with 2291.18 km^2 area where the population density is 42.7. Majority (>96%) of the population in Dallol Woreda follow Islamic religion. Many of the people speak Afar language called Affarigna and belong to the Afar ethnic group. They live in conventional households mainly breeding cattle and leading nomadic way of life (CSA, 2007). Goats and camels are the main cattle breed in the region.

1.4 Objectives

1.4.1 General Objective

The present study generally aimed at determining the structural control on the marine incursion and flooding history of the Dallol Depression to fill the gap in the geologic history of the Danakil Depression.

1.4.2 Specific Objective

This work specifically aims at

- Producing geologic and structural map of the study site at a scale of 1:50,000;
- Understanding the structural evolution of the study locale;
- Determining the deformation rate within the study area.

1.5 Methodology

In this study, it was aimed to constrain the structural control on the Red Sea incursion of the Dallol Depression by integrating data obtained from three different sources: (1) field-based observation, verification and measurements (2) remote sensing-based analysis and (3) seismic data obtained from potash companies in the region. The overall methodology adopted for the present study is depicted in the form of flowchart (see fig. 1. 7 below).

1.5.1 Field Investigation

The field investigation was carried out systematically following predetermined traverse routes. The major objective was to look for faults. This was achieved by applying the hypothesis that topography is often a good guide where traverse follows mainly streams along which the presence of faults was highly suspected. Traverses also focused where gypsum and associated coral outcrops are based on spots taken from satellite images during the pre-field phase of this research activity. From previous field works 21 coral outcrop sites were identified and the present fieldwork focused on these already discovered coral outcrops and lead to the production of geological map of selected relevant outcrops at a scale of 1:10,000 and 1:25,000. Lithologies other than evaporite units, coral reefs and beach deposits were mapped as substrate: volcanics, sandstones and conglomerates.

Fieldwork was undertaken in the study area to observe conditions and characteristics of the ground surface. There were two approaches: reconnaissance (the entire study area) and detail (specific locations in selected areas). The reconnaissance allowed to produce geologic map of the entire study area along with remote sensing technique at a scale of 1:50,000. The field observations were used to identify and verify the features displayed on satellite imagery. Geologic reconnaissance of the entire study area was initially undertaken and then specific areas were selected where utility of the imagery could be best tested. Structural measurements from the field were analysed using the stereographic projection technique (Allmendinger, 2012). Fault-slip data were processed using the computer software Faultkin version 7.5 using the graphical kinematic method described by Marrett and Allmendinger (1990).

1.5.2 Remote Sensing

In the remote sensing-based analysis two types of satellite data were used: optical and elevation data. The optical and elevation data comprise Landsat image and Shuttle Radar Topography Mission (SRTM) Digital Elevation Model (DEM) respectively. Landsat 8 data LC81680502014290LGN00 was accessed from the image courtesy of the U. S. Geological Survey Earth Resources Observation and Science Centre (http://earthexplorer.usgs.gov) for path/row of 168/050 scene in which the study area falls, free of charge. The data was from date and year 17.10.2014. Landsat 8 has 11 spectral bands where bands from 1 to 9 have 30 m resolution except band 8 which has a resolution of 15 m. The other two bands (band 10 & 11) have a resolution of 100 m (http://landsat.usgs.gov/about_ldcm.php).

During the preprocessing, all images were geo-referenced into one projection system where they were projected to Universal Transverse Mercator (UTM) zone 37N projection using World Geodetic System WGS84 datum. Images were clipped within the boundary of the study area and further digitization was performed along the Ethio-Eritrea boundary (see fig. 1.5 below). The satellite images were then layer stacked. These layers-stacked images were processed and analyzed using the software packages ENvironment for Visualizing Images (ENVI) version 4.7 and the Environmental Systems Research Institute (ESRI) ArcGIS suite of geospatial processing program ArcMap version 10.5. The actual processing comprise band combination and band ratioing. These satellite image processing methods are widely used in lithological and structural mapping (e.g., Solomon and Ghebreab, 2006; Mwaniki et al., 2015; Ali and Pour, 2014; Raharimahefa and kusky, 2006; Chatterjee, 2003; Al-Shumaimri, 2012; Ali et al., 2012).

The cirrus band (Band 9) and Band 1 were excluded as they were mainly designed to support atmospheric correction and for studies of coastal water and aerosols respectively. The thermal (Band 10, 11) bands were also not used.

The elevation data used in this study were obtained from Shuttle Radar Topography Mission (SRTM) Digital Elevation Model (DEM). SRTM DEM was released in February 2000 by a joint international project between the United States National Geospatial-Intelligence Agency (NGA) and the National Aeronautics and Space Administration (NASA), and the German and

Italian Space Agencies (Gupta, 2003). Elevation data of 90m spatial resolution was obtained from NASA`s Jet Propulsion Lab (JPL) through USGS's Earth Explorer website (http://www.jpl.nasa.gov/srtm).

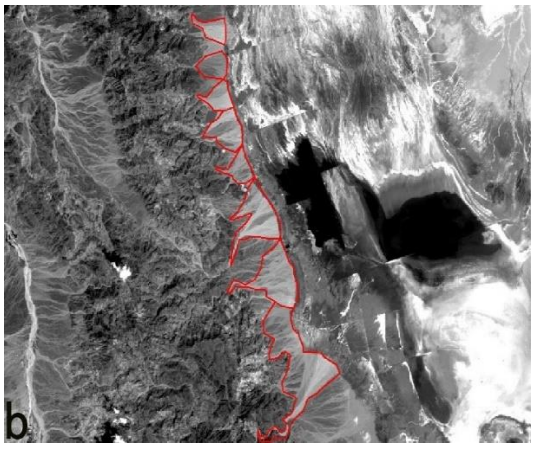

Fig 1.4 field photo of some of the geomorphic features of the study area (a) Maraho volcano (b) band 8 image of the alluvial fans indicated by red polygons (c) ridges (d) & (e) salt plain (f) salt pillar (g) hot acid pools (h) mud craters (i) gypsum canyon (j) Lake Assal

Fig. 1.4 (continued)

The individual SRTM-DEM tiles were mosaicked into one large image using ArcGIS 10.5. The mosaicked raster file was later resized to the exact coordinates of the study area (see fig. 1.6 below). The resulting DEM image provides the basis to create hill-shaded images, and to extract lineaments. The SRTM DEM data was processed using the Global Mapper software version 11.

1.5.3 Seismic Survey

In this study, secondary seismic data was also utilized. The seismic data were obtained from different potash companies in Dallol area, Ethiopia. Here the companies employed the two predominant techniques: the 2D and 3D seismic methods (BHP, 2012b; Allana, 2011; Circum, 2015) and processed and interpreted the acquired seismic data using various seismic interpretation software including IHS Kingdom, Landmark ProMAX V2003.19.1 processing

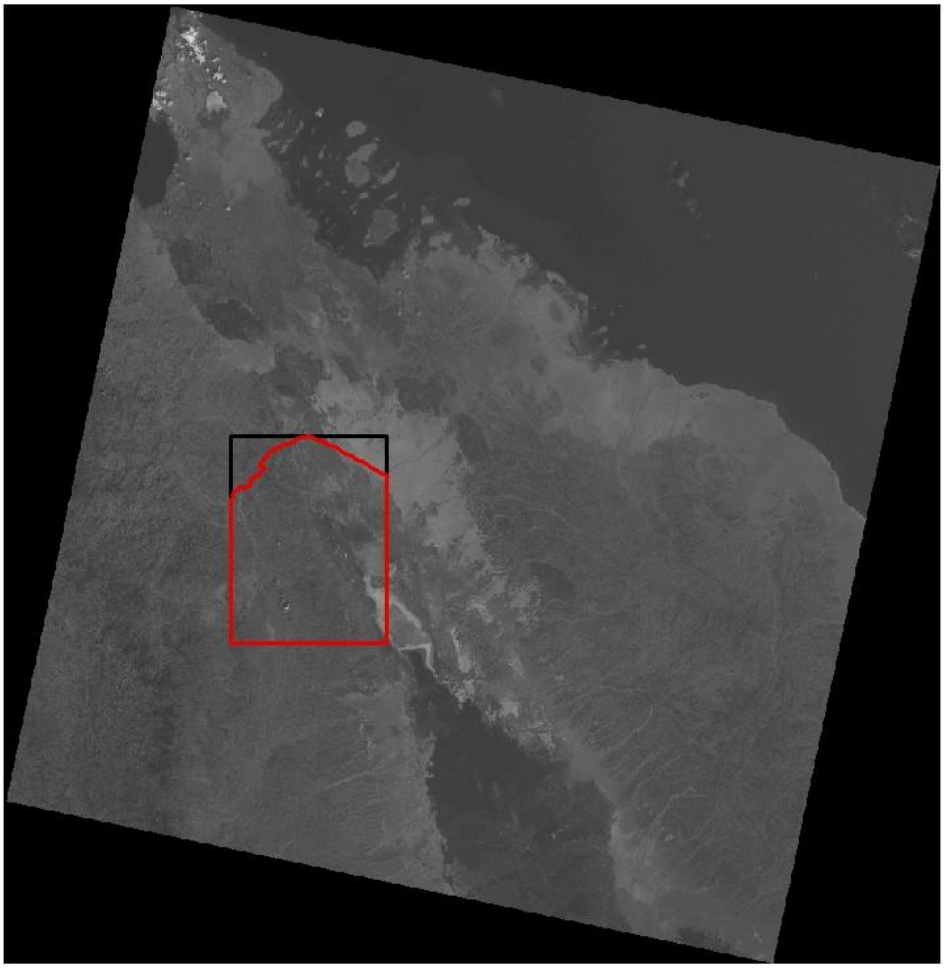

Fig 1. 5 Landsat 8 image of path/row 168/050: location of the study area is within the red box. The black rectangle was clipped from the image and then digitization performed along the Ethio-Eritrea border.

software and Green Mountain Geophysics (GMG) Millennium Suite refraction statics software.

1.5.4 Analog Geological Map

Analog geological map of the Northern Danakil Depression was published in 1973 by the French-Italian scientific cooperation (CNRS-CNR) at a scale of 1:500,000. This geologic map was scanned and georeferenced to UTM zone 37N projection using WGS84 datum and used as input to digitize regional lithologies and structures.

1.6 Limitations

Accessibility to the study area was limited mainly because it is found close to the Ethio-Eritrea border.

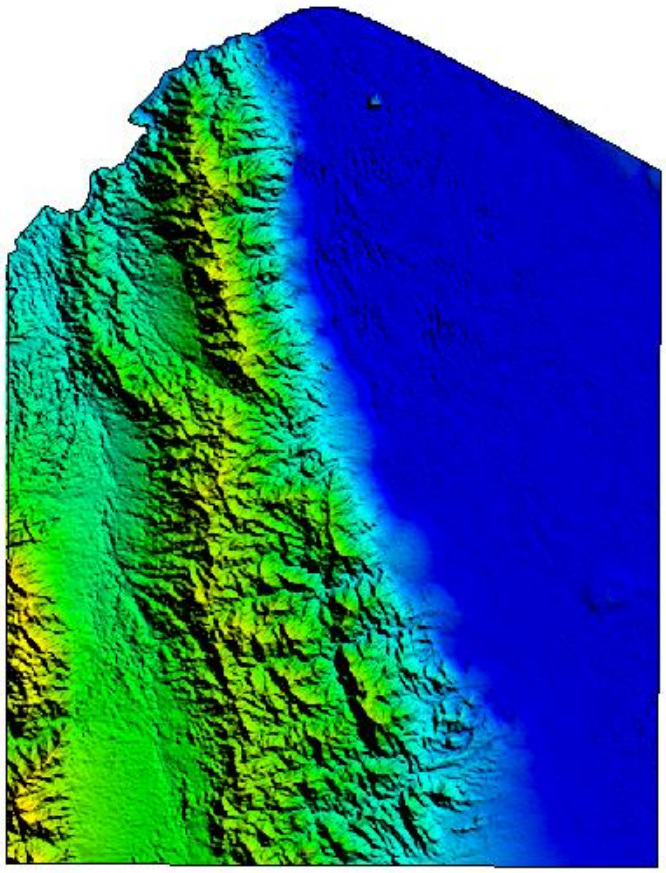

Fig 1.6 atlas shader of the study area

1.7 Future Studies

Detail study of available seismic data from different potash companies in the region can be used to model the basin architecture clearly aided by well bores to calibrate the seismic data.

1.8 Chapter Scheme

The thesis is structured into six chapters. The first chapter deals with the general introduction to the study area, problem statement, objectives and methodologies of the current study. This

is followed by chapter 2 which deals with the history of various geological studies in the Danakil Depression. Geology of the study area from regional perspective and from field investigation is presented in chapter 3. Chapter 4 is devoted for analysis of different data used in the current study. Results, interpretation and discussion of analysis of these data is presented in chapter 5. The thesis is concluded in chapter 6.

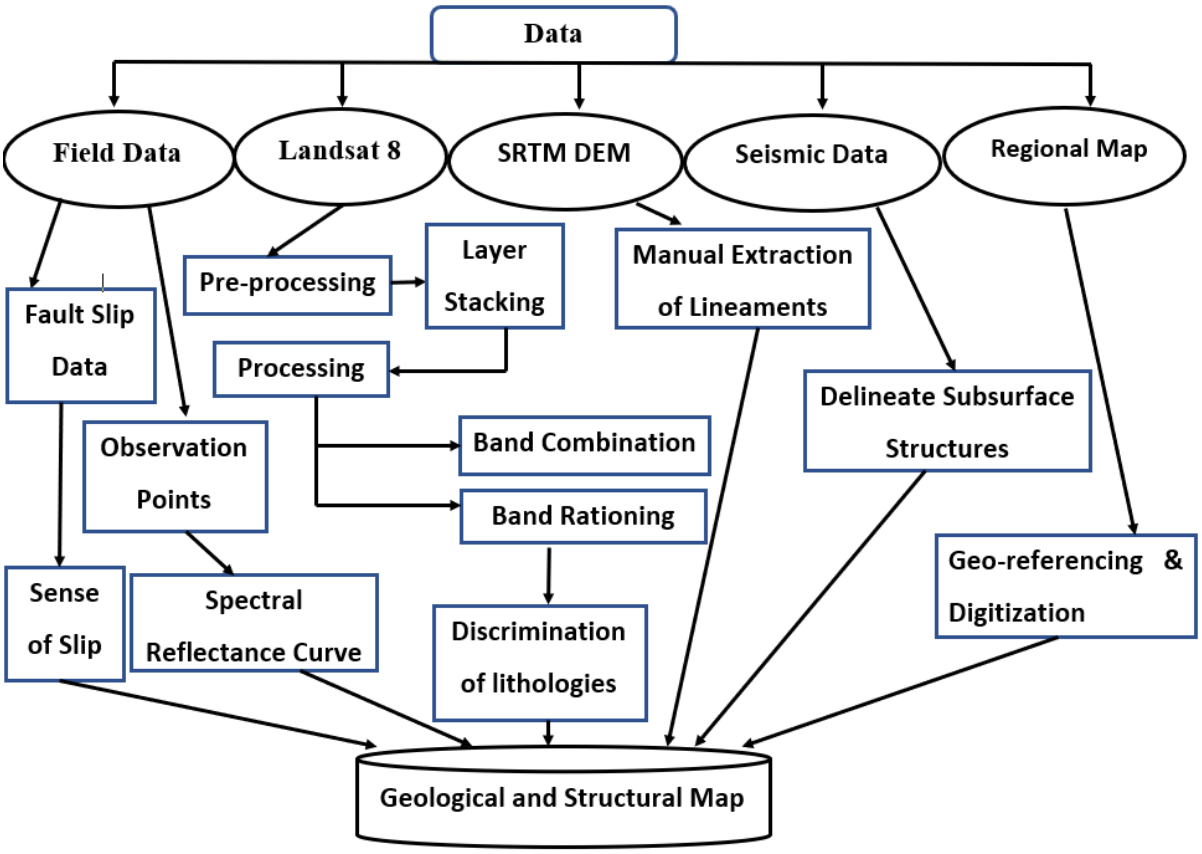

Fig. 1.7 flowchart of the data and methods used in the present study area

CHAPTER 2
RESEARCH HISTORY IN THE NORTHERN AFAR

In this section literature relating to the research history and research activities in the Danakil depression has been reviewed. The section discusses briefly the important results obtained from previous studies providing a conceptual framework for the better geological understanding of the northern Afar Depression. Literature related to the various methodologies used in this study and the general geological settings of the study area are discussed in resp. chapters 2 and 3.

2.1 Geological Mapping, Geochemical and Geochronological Studies

Regional geological mapping (Barberi et al., 1973) and radiometric (K-Ar) age determination (Barberi et al., 1972a) of volcanic rocks from the Danakil Depression enabled to distinguish three main volcanic units in the Afar: (1) volcanics of the axial zones, (2) volcanics along the margins of the depression, and (3) stratoid basalts. (Barberi et al., 1973; Varet & Gasse, 1978; Barberi et al., 1972b).

The axial volcanics are found flooring the Depression from the salt plain to Lake Afdera and are comprised of tholeiitic & alkali basalts to peralkaline rhyolites (Barberi et al., 1972b). Quite different volcanic units constitute marginal volcanics and are found along the margins of the Depression, in close connection with the pre-rift basement outcrops. Acidic lava, ignimbrite, pumice with minor basaltic lava characterize the marginal volcanics. Extensive and thick stratoid series cover the southern part of the Afar depression (Barberi et al., 1973; Varet & Gasse, 1973). According to Barberi et al. (1972a**)** the axial zone volcanics are probably of oceanic nature and consist mainly of transitional basalts with associated differentiates. This is the most recent volcanism of the depression (from 1 m. y. up to the present day) (Barberi et al., 1970). Volcanics along the margins of the depression mainly consists of silicic centres with minor basaltic lavas. This volcanism probably covers a wider time interval, and is still active (e.g., Dubbi Volcano). Stratoid volcanism produced a huge pile of flood basalts with intercalations mainly in the upper part of rhyolitic ignimbrites and flows. This volcanism covers a broad time interval probably from lower Miocene to recent Quaternary (23-0.37 m.

y.) and consists of transitional basalts and peralkaline silicic with scarce intermediate rock types (Barberi et al., 1972a).

The comparison of the compositional variations of major and trace elements in the axial range basalt with variations in the Mid-Oceanic Ridge Basalt (MORB) suggested an oceanic nature for large parts of the central Afar (Barberi & Varet, 1977). Particularly for the Erta Ale volcanic range the Strontium isotopic composition remains remarkably constant with low values ($^{87}Sr/^{86}Sr$= 0.702-0.704) implying a subcrustal origin for the Erta Ale Series, without distinctive contamination by crustal material enriched in radiogenic strontium (Barberi & Varet, 1970; Barberi et al., 1970). Another study by Miruts Hagos (2010), Miruts Hagos et al. (2016) and Barrat et al. (1998) confirm that the Danakil Depression is not composed of full-stage oceanic crust because the content of highly incompatible trace elements, REE, and their ratios are much higher than the content measured in the Red Sea and the Gulf of Aden basalts. The chemical differences between the basaltic rocks within the entire Afar Depression may result because of the variation in rifting stage, magmatic sources, and possibly the degree and depth of the melting. Miruts Hagos (2010), Miruts Hagos et al. (2016) suggested that the Danakil Depression basalts are derived from the plume-tail, the last phase of the Afar mantle plume, based on the abundance of highly compatible trace elements and Sr & Nd isotopic composition. Another geochemical study, which is the first noble gas or major gas observation for the Dallol active magmatic segment within the Red Sea arm of the Afar triple junction, hypothesizes that a combination of major and trace compositions may provide insights into the source and history of mantle fluids and their interaction with crustal waters and evaporites (Darrah et al., 2013). According to Darrah and others (2013) noble gas elemental and isotopic compositions analysis indicate that the Dallol gases display elevated helium isotopic ratios. Furthermore, Dallol fluids show significant mantle-derived contribution that are consistent with the Afar mantle plume (Darrah et al., 2013).

2.2 Stratigraphic Reconstruction

The spatial and temporal relation of quaternary syn-rift sediments in the Danakil Depression has never been studied in detail (Foubert et al., 2015). Very few studies focused on the sedimentary succession of the Afar Depression. Previous studies were linked to the late 60's and early 70's potash exploration. Holwerda & Hutchinson (1968) discussed the evaporite and

sylvite deposits and their unique geologic features and characteristics. This study established the first stratigraphy of the potash-rich intervals. Results indicate that that there is extensive evaporite accumulation due to periodic flooding by sea water and the prevailing hot, arid climatic conditions (Holwerda & Hutchinson, 1968). The established stratigraphy by Holwerda & Hutchinson (1968) places the sylvite unit between the upper halite and lower intermediate member (see fig. 2.1). The upper halite is overlaid by clastics. The intermediate member is overlying the kainite and lower halite respectively. In addition, the age of the salt is determined from the foraminifera within a thin bed of dark gray, silty marl intercalated with halite in one of the drilled core sections 58 m above the potash interval. It is found to be Middle to Late Quaternary age which makes it the youngest known major deposit of its kind (Holwerda & Hutchinson, 1968).

Holwerda & Hutchinson (1968) showed that the sylvite member of the Danakil succession does resemble the theoretical sequence on several counts. Firstly, it lies stratigraphically above the carnallite or intermediate member. Secondly, it is rich in sylvite, sufficiently so to reach its ore-grade in most places. Thirdly, equilibrium stability temperatures of several salts present in the lower members suggest temperatures of precipitation from about 25 to above 40^0C, and specifically the kainite member dictates temperatures in the range between 11^0 and 83^0C. These temperatures are virtually exclusive for the stability temperatures of sylvite deposition. Finally, the temperature range at which sylvite is unstable (11^0 to 72^0C) includes the temperatures expectable in a natural evaporation basin.

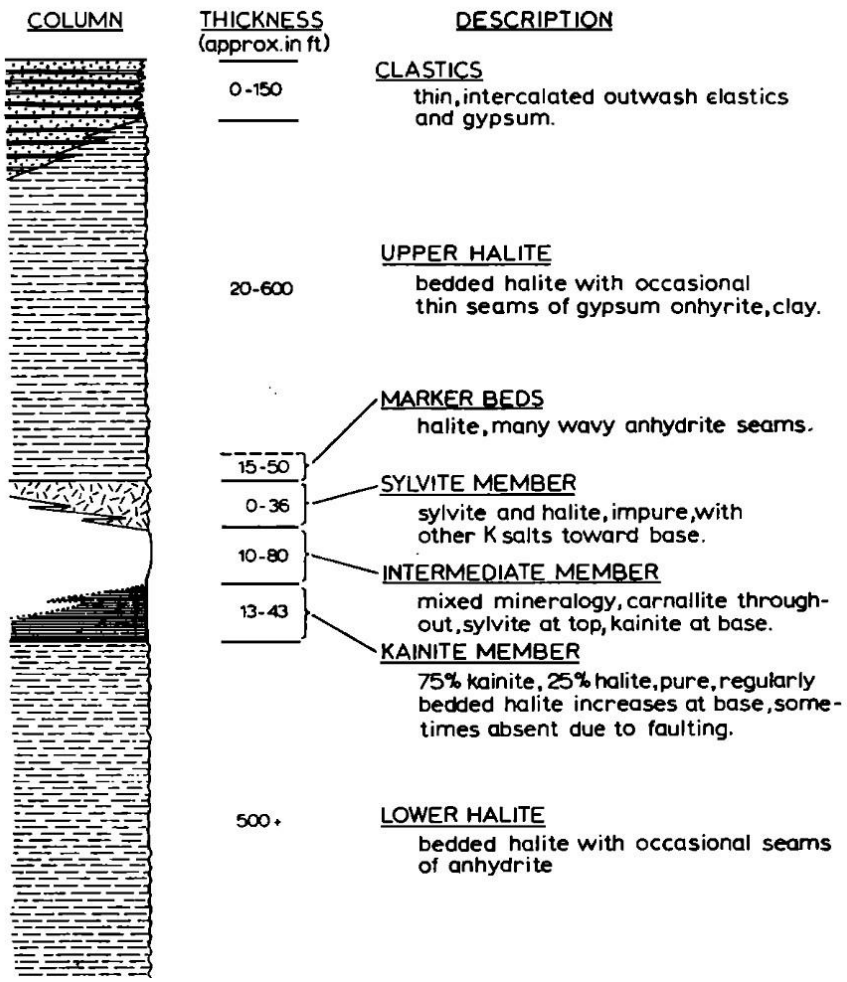

Fig. 2.1 diagrammatic stratigraphic column of potash interval, Musley area (Holwerda & Hutchinson, 1968)

These considerations dictate that the sylvite member is not primary, but has originated in another way. The stylolitic texture and slump structures of the sylvite member, its local inverse thickness relationships to the intermediate member, and the contrasts between these two and the kainite member all suggest that the sylvite member was formed from the intermediate member by secondary diagenetic process (Holwerda & Hutchinson, 1968).

A more regional stratigraphy of the Danakil Depression was established by Brickmann et al. (1970). After half a century, collaborative research teams from Switzerland (University of Fribourg) and Ethiopia (Addis Ababa University) are studying in detail the quaternary sediments of the Danakil Depression within the SNF (Swiss National Science Foundation) collaborative research project 'SERENA' (SEdimentary REcord of the Northern Afar). This collaborative study has the objective to unravel the spatial and temporal evolution of the

sedimentary facies in an active rift setting. So far, the research team has studied the growth and build-up of coral and algae called coralgal terraces and microbialites within the Danakil depression. Results indicate that the marine deposits consist of at least four superimposed coralgal units evidencing successive periods of fringing reef formation separated by erosional unconformities suggesting episodes of non-deposition and/or subaerial exposure (Foubert et al., 2015). Monospecific bivalve and gastropod shell accumulations between the coralgal units document alternating periods of restricted and open marine conditions (Balemwal Atnafu et al., 2015; Foubert et al., 2015; Jaramillo-Vogel et al., 2015). Jaramillo-Vogel et al. (2015) found the occurrence of two distinctive microbialites: one within the reef cavities and another on top of the reef units.

2.3 Tectonic Studies

Alebachew Beyene & Abdelsalam (2005) reviewed and synthesized the tectonics of the Afar Depression. This work summarized the physiography and geology of the Afar Depression; discussed the Nubian-Arabian–Somalian Plates separation and deformation of the Afar Depression; outlined different tectonic elements present in the Afar Depression; examined the nature of the Afar Lithosphere; outlined views on magmatic and tectonic processes in relation to the relative influence of far-field stress and upwelling mantle plume in the evolution of the Afar Depression; and synthesized these views in a comprehensive model for the Afar Depression. The review and the synthesis by Alebachew Beyene & Abdelsalam (2005) indicate that there are four major factors that influenced the evolution of the Afar Depression resp.: (1) The Rise of the Afar Dome; (2) Sequence of magmatism, uplift, rifting and lithospheric rupture; (3) the development of the Main Ethiopian Rift, the Red Sea and the Gulf of Aden Rift, and their interaction with other plate boundaries; and (4) the internal rearrangement of the individual tectonic elements of the Afar Depression.

Another study (Samson Tesfaye et al., 2003) documents the early continental breakup boundary of the Afar triple junction estimation that the Afar triple junction has migrated ~1.5° (~160 km) in N-NE direction with respect to the African (Nubian) plate in the past 25 m.y based on structural and geomorphological evidences. High-resolution digital terrain elevation data (DTED), coarse resolution global digital elevation model (GTDP030), Landsat Thematic Mapper (TM) images, stereo large formal camera (LFC) images, and existing geologic

information are used to document the observations of Samson Tesfaye et al. (2003). According to Samson Tesfaye et al. (2003) The estimated amount of migration of the Afar triple junction is less than the 200km migration expected from plate kinematic analysis (Samson Tesfaye et al., 2003). This discrepancy suggests either a slower rate of spreading than the current ~1.6 cm/yr rates (Africa-Arabia) during the early phase of rifting or a later early Miocene rather than Oligocene-Miocene age for the initiation of tectonic activity in the triple junction (Samson Tesfaye et al., 2003). High resolution (Landsat TM ~30 M resolution) satellite imagery calibrated by field studies and digital topography data was used to delineate faults and magmatic centers throughout the northern main Ethiopian rift (MER) and Afar (Hayward & Ebinger, 1996). According to Hayward & Ebinger (1996), there is a significant and systematic decrease in the length and width of Quaternary basins from south to north in the MER and Afar rift system. The Quaternary border faults decrease in length and scarp height from south to north as well. Larger volumes of quaternary basaltic magmatism in the northern Afar, without the development of rift valley/flank morphologies, lead to a magmatic rift segmentation (Hayward & Ebinger, 1996).

Different studies for different objectives (e.g. Barberi et al., 1973; Gibson and Tazieff, 1970; Hofstetter and Beyth, 2003; BHP Billiton, 2012a and Allana Potash, 2012) based on field investigations, Landsat image interpretation and seismic surveys revealed that all geologic features, including active fissure volcanism, normal faulting, open tensional faults, evidence generally NNW trends paralleling the major tectonic structures in the Red Sea. Furthermore, rose diagram plots of the faults dissecting the Depression indicate that there is a good concentration of strike frequencies around the value of $N20^0W$ in the northern apex which is assumed to be the most representative fault direction in the Danakil Depression (Barberi et al., 1973). Results from fault plane solutions for the Afar Depression indicates mainly strike slip and a normal sense of movement (Hofstetter and Beyth, 2003). These observations are consistent with the tectonic setting of the region and this shows that there is good agreement between the main tectonic features in the Afar Depression and the focal mechanisms of the observed events (Hofstetter & Beyth, 2003).

2.4 Geophysical and Remote Sensing Studies

There are only a few seismic and remote sensing investigations in the Danakil Depression (for e.g., Hofstetter and Beyth, 2003; Thurmond et al., 2006; Nobile et al., 2012; BHP Billiton, 2012b; Allana Potash, 2012). Thurmond and others (2006) proved that optical-radar-DEM data integration is an effective approach for geological mapping and structural analysis in arid regions such as the Afar Depression where there is lack of vegetation and soil cover and almost continuous exposures of bedrocks. InSAR and seismicity studies in Dallol area gave new insights on the interaction between diking and faulting in a region at the final stages of continental breakup (Nobile et al., 2012). This study showed a 2.4 km deep active magma reservoir beneath Dallol that likely fed a ~0.06 km^3 dike intrusion along the Dallol segment accompanied by a Mw 5.5 earthquake and associated fault slip along the western flank of the rift in 2004. Data from this study suggest that a shallow active magma chamber exist below Dallol which deflated in response to an along-rift dike intrusion. Nobile and others (2012) have also suggested that a seventh magmatic centre should be added apart from the other six active volcanoes spaced at 10 km intervals in NNW-SSE direction in the East African Rift (Barberi & Varet, 1970).

In the time from 2008 to 2012, BHP Billiton conducted prospecting and exploration work in the depression. The work involved Landsat image interpretation, geophysical data modelling and drilling. This exploration and prospecting work produced two 1:100,000 scaled and three 1: 250,000 scaled geological maps based on the interpretation of Landsat ETM+ data. The maps are similar to the 1:250,000 geological map published in 1970 by Brinckmann and others (BHP Billiton, 2012b). The Landsat image interpretation indicated that the Danakil Depression is dominated by NNW-NW trending faults that run parallel to the margin of the rift basin and a number of cross-cutting NNE-NE faults. Moreover, straight and curvilinear contacts between Landsat interpreted lithological units are consistent with buried faults. According to BHP Billiton (2012a) the 2D structural template portray a relatively simple, symmetrical rift in contrary to previous interpretations of the presence of a macroscale asymmetric half graben by Holwerda & Hutchinson (1968). The map patterns, including fault traces, facies types, stratigraphy, and modern drainage systems, are symmetrically disposed around an axial corridor. Based on structural geology observations as deduced from surface geologic relations,

geophysical data, and drill hole data the basin is interpreted as an asymmetric basin (Holwerda & Hutchinson, 1968). According to Hutchinson and Eagles (1970) there is no major west-dipping fault system or west-facing escarpment known, only east dipping rift fault system occur along the east facing escarpment that bound the Ethiopian Plateau and the Danakil Alps on the east. Holwerda & Hutchinson (1968) add the regional dips of strata and the lithofacies distribution as another evidence supporting the asymmetry of the basin. These authors substantiate their argument by several geologic features indicating that the Danakil Basin subsidence in the west with accompanying Danakil Alp uplift in the east, which cannot be a result of simple 'graben-horst' tectonics.

In addition, interpretations based on aeromagnetic and gravity data revealed that the Depression is a 3-4 km deep rift basin and its floor is characterized by grabens and horsts or rotated half grabens. Within this basin salt is not universally present and exposed shield volcanoes are of limited thickness (BHP Billiton, 2012b). According to BHP Billiton (2012b) the overall configuration of the basin is an essentially NNW to SSE trending trough approximately 10-15 km wide. The lithological succession in the basin, down to a depth of about 800 m, is predominantly halite with thin interbeds of other materials such as sylvinite, kainite and anhydrite. Maximum sedimentary thickness of the basin appears to occur immediately to the west of the so called Western Limb Main Growth (WLMG) (BHP Billiton, 2012b). The Western Limb Main Growth Fault (see fig. 2.2) structure is the eastern bounding fault of the basin (BHP Billiton, 2012b). Estimates of the basin's total sediment thickness made by BHP Billiton (2012b) ranged from 1720 m in the north to 3680 m in the south. There was rapid subsiding and 'pulling apart' of the basin due to the regional tectonics. The 2D seismic interpretation which revealed these results did not make it possible to make correlations of the seismic data with the geologic formations (BHP Billiton, 2012b). The correlation was not possible because there were no well logs available for this purpose.

Allana potash (2012) conducted seismic surveys to evaluate the continuity of the evaporite horizons and to delineate potential fault zones cutting the deposit horizons for exploration purpose. The data from the seismic survey confirm the overall graben structure with a shallow graben shoulder in the western parts and a deeper graben in the central part of the Depression within the license area of the potash corporation. The data also show undisturbed layering in

the evaporites, suggesting that no major faults with vertical throw are present at a high angle to the graben structure. However, there is an important fault zone that separates a relatively shallow potash interval of the graben shoulder from a deep potash interval in the graben center. This fault seems to dip relatively steeply towards the east. It is interpreted as a NW-SE striking normal fault zone with a down throw that might be in the range of 100 of meters. Localized smaller scale faults with minor offset seem to be present as well (Allana Potash, 2012).

2.5 Hydrogeological/Geothermal Investigations

Hydrogeological/geothermal investigations by Gonfiantini et al. (1973) and Franzson et al. (2015) determined the origin of the waters of the Dallol hot springs and cold and hot springs of Lake Afdera. Gonfiantini et al. (1973) investigated the origin of water in the Dallol hot springs and Lake Afdera cold and hot springs and the lake itself and the eventual modification of its original isotopic composition introduced by isotopic exchange processes and by evaporation. In this study, they have done water sampling making use of a syringe equipped with 50 cm of Teflon tube. Gonfiantini and others (1973) concluded that the origin of the waters of the Dallol hot springs and the cold and hot springs of Lake Afdera are of meteoric nature. The water in the Dallol hot spring are enriched in $\delta^{18}O$ by high temperature isotopic exchange with the carbonates and sulfates of the underlying evaporite sediments. According to Gonfiantini et al. (1973) small and distinct isotopic differences observed in the cold and hot springs of Lake Afdera are probably related to mixing of waters in different proportions having slightly different isotopic compositions and salt content. There is a non-uniform isotopic composition of the water of Lake Afdera in along specific depth profiles and this could be explained by the seasonal stratification of the water which had not yet completely disappeared (Gonfiantini et al., 1973). Isotope data from the geochemical studies conducted by Franzson et al. (2015) indicate that the surface water and fumarole steam in Dallol area have different origins, the former being meteoric whereas the latter stem from the underlying geothermal reservoir.

Few studies (UNDP, 1973; Varet, 2012, 2012; Franzson et al., 2015 and Carniel et al., 2010) investigated the geothermal potential of the Danakil Depression along with the Main Ethiopian Rift. Detailed descriptions of hydrothermal features in the Ethiopian rift on selected targets: (1) Tendaho Graben, (2) Danakil Depression and (3) Aluto Volcanic Center was conducted by

UNDP in 1973. This was accompanied by detailed mapping of the main hydrothermal areas employing photogeologic interpretations and field observations with a primary objective of identifying and evaluating local regions of anomalous heat flow (UNDP, 1973). Ground investigation and infrared photography within 150,000 km^2 of the rift of Ethiopia along with geologic, geochemical and hydrologic techniques were utilized. In addition, analysis of hot spring, surface and well waters and fumarole gas samples were employed. This work identified more than 500 hydrothermal features. Geological and geophysical evidences both strongly suggest that the heat source under Dallol is a shallow intrusion. High salinities and low pH may require special technology for the development of geothermal resources in this region. Geological evidences suggest that vast heat reserves underlie the Danakil Depression. The preferred and the most promising locality in the Depression is Dallol where there is evidence of important hydrothermal explosions within the historic past. This suggests the presence of high temperatures at depth. The geochemical evidence is inconclusive because of the overwhelming contribution of chemicals from the evaporites. All deep waters reaching the surface are so altered that the accepted geochemical indicators of subsurface conditions cannot be used with any degree of reliability. Based on the geochemical evidence only, Dallol cannot be recommended as a geothermal prospect. The near-surface evaporites completely obscure any indicators of conditions at depth (UNDP, 1973).

Varet (2010; 2012) took a new look at four potentially favourable geothermal sites, including Dallol, in the Afar region and proposed new approaches taking into consideration the hydrological basins feeding the potential sites. The geological simplified model for the Dallol geothermal systems has shown that underlying the salt plain and hypersaline geothermal

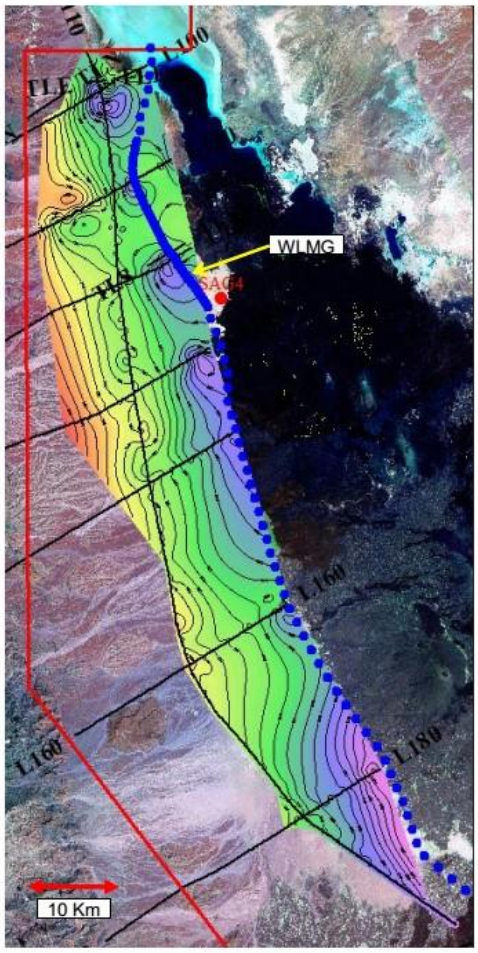

Fig 2.2 Satellite image indicating western limb main growth fault represented by blue line (BHP, 2012b)

system, there might be a deeper aquifer in the Jurassic limestone characterized by both low salinity and regular recharge by meteoric water descending from the NW Ethiopian Plateau (Varet, 2010, 2012). The presence of a high-pressure, high temperature reservoir is evidenced by the numerous past and present phreatic explosions, as well as by the steam vents aligned on NNW trending open fissures frequently opening through the salt cover. The presence of combination of high heat flow, a highly fractured area (the transverse faults in the vicinity) (Varet, 2010, 2012) or buried graben faults (Franzson et al., 2015) and the recharge of the reservoir by meteoric water from the plateau has shown that the Dallol area can act as a potential geothermal site (Gonfiantini et al., 1973; Varet, 2010, 2012; Franzson et al., 2015). According to Varet (2012) Dallol geothermal site would be worth analysing for prefeasibility and feasibility studies leading to industrial development reconsidering the conclusions drawn from previous studies (UNDP, 1973) based on the geochemical content of the hot springs in the area suggesting that the Dallol area is unsuitable for geothermal development.

Evaluation of the geothermal potential of the Dallol geothermal system in association with future potash mining activities in the area was directed to establish the presence of a high temperature reservoir in the area and to produce a conceptual model of the geothermal system based on the data acquired. Geological and geochemical field studies along with XRD analysis of rock samples from the various salt structures and isotope analysis of surface waters were carried out. This investigation resulted the first conceptual model of the Dallol geothermal system. Results from geological investigation has shown that all geothermal features are superimposed on salt flow and black salt extrusion confirming a younger age (Franzson et al., 2015). The geothermal features are manifested in the form of salt pillars, circles, and acid lakes. According to Franzson and others (2015) 70 rock samples from a total of 80 showed halite is the dominant mineral. Anhydrite was the most common subsidiary mineral and other minerals mostly showed up as traces including gypsum, carnallite, jarosite, bischofite, sylvite and thenardite. The iron oxides, which dominantly were found in the salt and dome flows were mainly hematite and some magnetite. Sulphur was commonly found in the geothermal activity areas (Franzson et al., 2015). Results from fluid chemistry indicate that the surface waters at Dallol and surroundings have very high salinity and pH ranging from moderately acidic to extremely acidic liquid.

The first integrated multi-parametric geophysical data set close to the superficial hornitos of Dallol was collected in 2003 (Carniel at al., 2010). This work discussed the use of this data set for understanding the underlying hydrothermal system. Based on thermal, seismic and acoustic measurements, Carniel et al. (2010) identified the presence of the alternation of low and high activity regimes, which are determined by shallow processes and are therefore mostly independent for each other and of the superficial structure within the hydrothermal system.

2.6 Coral Reef Studies

The Danakil Depression was once connected with the Red Sea evidenced by the presence of marine deposits within the Depression (Bonatti et al., 1971; Balemwal Atnafu et al., 2015). The Depression was flooded at least two times by the Rea Sea during 80-130 ka (MIS 5) and 191-243 ka (MIS 7) (Foubert et al., 2015; Balemwal Anafu et al., 2015; Jaramillo-Vogel et al.,

2016; Jean-Charles et al., 2016). Bonatti et al. (1971) studied the final desiccation of the Depression employing C^{14} and Th^{230}/U^{234} dating methods and stable O^{18}/O^{16} and C^{13}/C^{12} isotopes analyses on three fossil samples (2 mollusk specimen and 1 coral specimen). According to this study the O and C isotope analyses indicate deposition of skeletal material under normal marine conditions, followed by recrystallization during evaporation and increased salinity. C^{14} analysis dates the formation of the unrecrystallized portion of the mollusk specimen at 31,600 years ago, and recrystallization as having occurred most probably within about 2000 years. The U/Th age of the unrecrystallized mollusk sample is 54,000 years, which is considerably greater than the corresponding C^{14} age. This is expected because mollusks show often open system behaviours with respect to U migration. The age obtained for the coral sample is 37,800 years, or about 6,000 years greater than the C^{14} age obtained for the unrecrystallized mollusk sample. Because of the large net evaporation rate of the Afar region, growth of marine invertebrates could not have occurred much after the final separation of the region from the Red Sea. Thus, volcanic events responsible for this separation are dated at not earlier than about 32,000 years ago. Within 2000 years, desiccation had proceeded to the point where a substantial portion of the original seawater had evaporated as indicated by the oxygen isotopic value given by the recrystallized mollusc sample. Total desiccation might have taken another 2000 years. In any case, final separation of the Danakil Depression from the Red Sea appears to have occurred not earlier than 32,000 years ago, and desiccation to have occurred largely or entirely within a few thousand years (Bonatti et al., 1971).

CHAPTER 3

GEOLOGY

3.1 Regional Geologic Setting

3.1.1 Tectonovolcanic setting of the Afar Depression

The East African Rift System (EARS) is characterized by a N-S oriented stretch zone over 6000 km long running from the Afar to the Davie ridge. It comprises three branches: the eastern, the western and the south-eastern branches (Chorowicz, 2005; fig 3.1). The eastern branch of the EARS is an ~2000-km-long (Hayward & Ebinger, 1996; Chorowicz, 2005) intracontinental extensional system composed of several interacting rift segments, from Mozambique to Afar (Bekele Abebe et al., 2007; Chorowicz, 2005 and references therein). Its northernmost part comprises the Ethiopian Rift System (Bekele Abebe et al., 2007). The Ethiopian Rift System, which extends about 1000 km in a NE-SW to N-S direction from Afar southwards to the Turkana Depression, constitutes the Main Ethiopian Rift (MER) and the Afar Depression (Corti, 2009; Pürschel et al., 2013; Samson Tesfaye et al., 2003).

The Afar Depression (AD), north-eastern branch of the Ethiopian Rift (Billi, 2015), is a spectacular region that encompasses parts of Ethiopia, Eritrea, and Djibouti (Hammond et al., 2011; Varet et al., 2012). It forms a unique outdoor laboratory exposed on land to study the transition mechanisms from continental rifting to seafloor spreading centres (Atalay Ayele et al., 2007; Bastow et al., 2005; 2008; Bridge et al., 2012; Doubre et al., 2007; Atalay Ayele et al., 2009; Miruts Hagos et al., 2016; Mock et al., 1999; Ameha Atnafu et al., 2013; Varet & Gasse, 1978; Hayward & Ebinger et al, 1996; Bonatti et al., 1971). The Depression is the result of the fragmentation of a once stable continental lithosphere that underlies most of the Neoproterozoic Arabian–Nubian Shield and the Mozambique Belt within the East African Orogen (Stern, 1994). It is produced by rifting between the African, Arabian & Somalian plates (see fig 3.2) during the past ~30 Myr (predominantly the last 10 Myr) within the Paleogene flood basalt province believed to have originated from the Afar mantle plume (Hofmann et al., 1997; Atalay Ayele et al., 2007b; Hayward & Ebinger, 1996; McKenzie et al., 1970; Bastow et al., 2008; Wolfenden et al., 2005; Ebinger et al., 2008; Gezahegn Yirgu et al., 2006). This coincides roughly with the onset of rifting in the Red Sea and Gulf of Aden (Wolfenden et al., 2004; 2005; Bosworth et al., 2012). The crustal nature of the Afar is controversial (Tilahun

Mammo, 2004; Barrat et al., 1998; Chorowicz, 2005; Gupta & Scholz, 2000; Abbate, 1995; Stab et al., 2015). Some argue the nature of the Afar crust is oceanic (Barberi & Varet, 1977; Barrat et al., 1998), others argue that it is transitional from continental to oceanic crust (Tilahun Mammo, 2004; Makris & Ginzburg, 1987; Atalay Ayele et al., 2009) and still others believe it is new igneous crust (Mohr, 1989). It is not yet clearly established which parts of the Afar

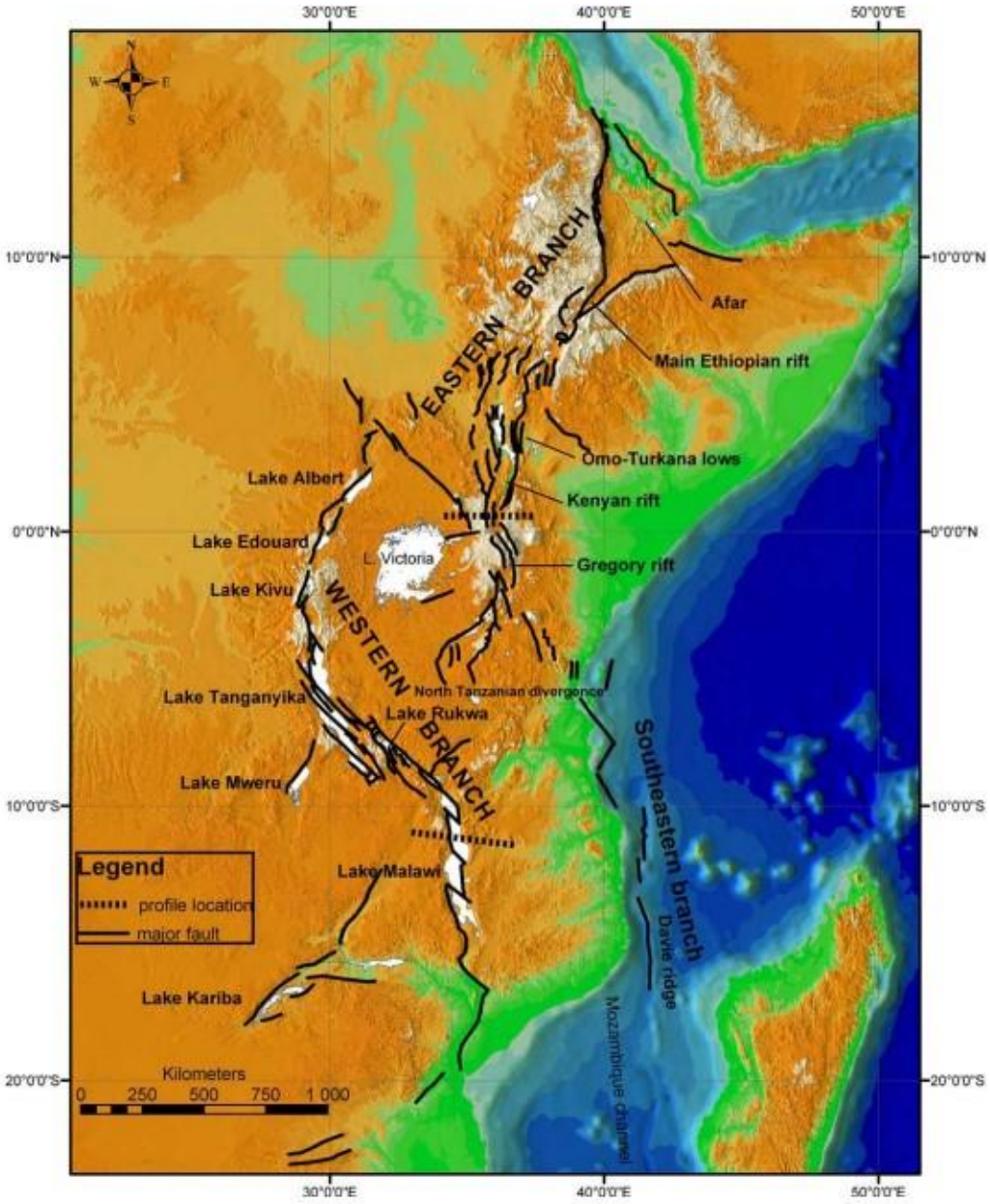

Fig. 3.1 Hypsographic DEM of the East African rift system. Black lines: main faults; white surfaces: lakes; grey levels from dark (low elevations) to light (high elevations). The East African rift system is a series of several thousand kilometres long aligned successions of adjacent individual tectonic basins (rift valleys), separated from each other by relative shoals and generally bordered by uplifted shoulders. It can be regarded as an intra-continental ridge system comprising an axial rift (from Chorowicz, 2005).

Depression is characterized by oceanic crust and which parts are thinned continental lithosphere (e.g., Makris and Ginzburg, 1987; Souriot and Brun, 1992; Ebinger and Hayward, 1996; Hayward and Ebinger, 1996). The Afar Depression covers an area of ~200,000 km^2 and is ~300 km wide and ~ 600 km long (Alebachew Beyene & Abdelsalam, 2005; Manahloh Belachew et al., 2011; Bosworth et al., 2005; Chorowicz, 2005).

The AD comprises the subaerial Late Oligocene - Early Miocene archetypal rift-rift-rift Afar triple junction (see fig. 3.2) where two seafloor spreading centres - the southern Red Sea (Arabia-Africa) and the western Gulf of Aden (Arabia-Somalia) meet with the northern Main Ethiopian Rift (Somalia-Africa) (Barberi & Varet, 1970; McKenzie et al., 1970; Abbate et al., 1995; Alebachew Beyene & Abdelsalam, 2005; Atalay Ayele et al., 2007b; Barisini et al., 2009; Bastow et al., 2005; 2008; Black et al., 1972; Bosworth et al., 2005; Doubre et al., 2007; Eagles et al., 2002; Wolfenden et al., 2005; Field et al., 2013; Hébert et al., 2001; Barberi & Varet, 1977; Bonatti et al., 2015; Gonfiantini et al., 1973; Abbate et al., 2004; Abbate et al., 2015). The Afar triple junction was first established when the NNW-SSE directed extension propagated northwards along the MER reaching the southern Afar ca. 11 Ma ago (Wolfenden et al., 2004). Since then, the triple junction has continued propagating NE, overprinting older structures, towards its current position near Lake Abhe (Samson Tesfaye et al., 2003). The Red Sea rift has split the Nubian and Arabian shields; the Gulf of Aden separates the Arabian and Somalian plates; and the northern MER is starting to separate the Somalian plate from the rest of Africa (Pasyanos & Nyblade, 2007; Alebachew Beyene & Abdelsalam, 2005).

This junction is not a classical triple junction. It is rather a diffuse quasi-triangularly shaped triple junction (Dauteuil et al., 2001; Abbate et al., 2015) where only two out of its three rift systems (Red Sea and MER) meet, whereas the third (Gulf of Aden rift) has no clear connection with them. The Gulf of Aden does not directly join the other two rift systems. It penetrates landward with the rifts of Asal, Inakir and Manda which roughly parallel the Red Sea system for one hundred of kilometre, and then branch out as a NW-trending horsetail merging into the complex extensional structure of the northern part of the Afar Triangle (Abbate et al., 1995; Hébert et al., 2001), i.e., there is no oceanic spreading between Red Sea and Gulf of Aden yet (Courtillot et al., 1980; Courtillot, 1982; Courtillot et al., 1984; Courtillot et al., 1987). However, the fact that there is no oceanic spreading between the Red Sea and the Gulf of Aden

doesn´t mean that is there is no structural connection. The Red Sea by passes Afar, east of the Danakil Block, reaching into the Gulf of Aden through the Strait of Bab El Mandeb. Its subaerial continuation is a narrow, NW trending belt of active normal faulting, dense fissuring, and volcanism that follows the SW edge of the Afar Depression, to Lake Abhe. The Gulf of Aden ridge also bypasses Bab E1 Mandeb to penetrate directly into Afar, through the Gulf of Tadjoura and the Ghoubbet strait. It then veers into another narrow, NW trending belt of active volcanism and faulting that hugs the west side of the Danakil block, to the Manda Inakir rift (Tapponnier et al., 1990).

The Red Sea is linking to the Afar Depression through the Gulf of Zula and similarly to the Gulf of Aden through the Gulf of Tadjoura (Bosworth, 2015). The two oceanic spreading ridges join the NMER in the Afar Depression (e.g., Hébert et al., 2001) and they appear to propagate still at present time through a series of disconnected parallel embryonic spreading centers (Manighetti et al., 1997; 1998). According to propagation model by Manighetti et al. (1997) the two plate boundaries cannot meet. Their opposite sense of propagation towards the north and south makes them jump constantly away from each other, toward the NE and SW since the southward propagation of the Red Sea spreading axis is stopped by the ancient major E-W structure causing a jump into the Danakil Depression. The westward propagation of the Gulf of Aden is stopped by Marda Fault Zone (which is parallel to the NW Red Sea trend) as soon as it crosses the Danakil-Aisha Blocks west of Djibouti (Beyth, 1991). They miss one another without achieving connection (Manighetti et al., 1998). The NMER is propagating northward into the southern Afar Depression (Wolfenden et al., 2004).

The three extensional major plate boundaries are in different stages of evolution (Gupta & Scholz, 2000). They are different in age (Barberi et al., 1972b; Wolfenden et al., 2004) and have different divergence rates (Chu & Gordon, 1998). Continental separation has occurred in the Red Sea and Gulf of Aden while seafloor spreading has yet to begin in the MER. NE-directed seafloor spreading in the Gulf of Aden has propagated a distance of over 1500km in constant westward direction (oblique to the Arabian-Somalian motion vector) (Manighetti et al., 1997) into the Afar Depression since the last 16 Ma (d'Acremont et al., 2005) or 25 Ma (Manighetti et al., 1998) and NE-directed seafloor spreading started around 4 Ma ago in the Red Sea (Cochran & Martinez, 1988; Bonatti et al., 2015). The third arm of the triple junction,

i.e. the northern MER, is much younger and started to propagate northwards into the Afar Depression 11 Ma ago (Bastow et al., 2005, 2008; Wolfenden et al., 2004; Keir et al., 2015).

The last 3 Ma, faulting and volcanism within the Afar Depression resulted in 60-km long and 10-km wide zones of aligned chains of fissural flows, basaltic cones, stratovolcanoes, shallow seismicity and positive gravity anomalies (Barberi & Varet 1977; Hayward & Ebinger 1996; Manighetti et al., 1998). These Quaternary-Recent magmatic segments (refer to figure 3.3) are similar in size, morphology, structure and spacing as the second order (~50 km-long) non-transform segments of a slow-spreading mid-ocean ridge (Hayward & Ebinger 1996; Manighetti et al., 1998). These magmatic segments are formed by the injection of dikes into the upper crust from underlying magma chambers (Ebinger et al., 2008).

A large rifting event in one of these rift segments, the Dabbahu-Manda Harraro magmatic rift segment (see fig. 3.3) in the northern Afar, occurred in September 2005 during which 165 earthquakes were recorded, of which 15 were greater than M5, as well as a large vent opening associated with a small eruption (Wright et al., 2006; Rowland et al., 2007). The Dabbahu-Manda Harraro rift segment, which is the largest dike opening event ever measured using satellite geodetic methods, showed that up to 8 m of opening occurred on the a ~60 km long, ~10 km deep dike (Wright et al., 2006; Atalay Ayele et al., 2007). This volcano-seismic event was further punctuated with 14 large volume dikes between 2005 and 2010 (Ebinger et al., 2010; Hamling et al., 2009). According to Ebinger et al. (2010) observations from this rift segment reveal the interplay between faulting and magmatism in space and time during one intense rifting episode as well as its relation to the time-averaged rift morphology. The combined data sets and the exposed rock record require the interplay between multiple active magma reservoirs Studies from the Dabbahu rifting event (Keir et al., 2009; Ebinger et al., 2010) reveal that the primary extension mechanism in the Afar Rift is episodic and rapid opening of discrete rift segments such as the Dabbahu magmatic segment itself.

3.1.2 Stratigraphy and Lithostratigraphic Units

The geological formations of the Afar Depression and its marginal areas and surrounding plateaus can be divided into four major units going from pre-rift to syn-rift complexes (fig. 3.4): (1) Pre-rift complexes (Neoproterozoic basement, Mesozoic sedimentary rocks, and

Eocene–Miocene basalts); (2) Syn-rift igneous rocks (Miocene igneous rocks); (3) Pliocene–Pleistocene volcanic rocks; and (4) Quaternary volcanic and sedimentary rocks (Alebachew Beyene & Abdelsalam, 2005; Bosworth et al., 2005).

3.1.2.1 Pre-rift complexes (Neoproterozoic basement, Mesozoic sedimentary rocks, and Eocene–Miocene basalts)

The Neoproterozoic basement, which represent part of the Arabian-Nubian Shield (ANS), is prevalent on the periphery of the Afar Depression (see fig. 3.4). The ANS covers vast terrain to the N & NW of the AD in eastern Eritrea and Northern Ethiopia, respectively (Stern, 1994; Abbate, 1995). The Neoproterozoic rocks of the ANS also occupy parts of the Danakil and Ali-Sabieh Blocks (Alebachew Beyene & Abdelsalam, 2005; Bonatti et al., 2015; Barberi et al., 1973). The basement rocks were assembled and metamorphosed between 800 and 650 Ma ago during closure of the Mozambique Ocean, suturing the components of East and West Gondwana along the East African Orogen (Stern, 1994).

Stratigraphically the basement rocks are overlain by Mesozoic sedimentary rocks (see fig. 3.5) that get progressively younger towards the south on the Ethiopian Plateau. On the Ethiopian Plateau, the Mesozoic sedimentary rocks comprise Early Jurassic Adigrat Sandstone, Middle Jurassic Abay Limestone, Late Jurassic Antalo Limestone and Cretaceous Debre Libanos Sandstone (Holwerda & Hutchinson, 1968; Alebachew Beyene & Abdelsalam, 2005 & references therein). According to Holwerda & Hutchinson (1968) the Mesozoic formation

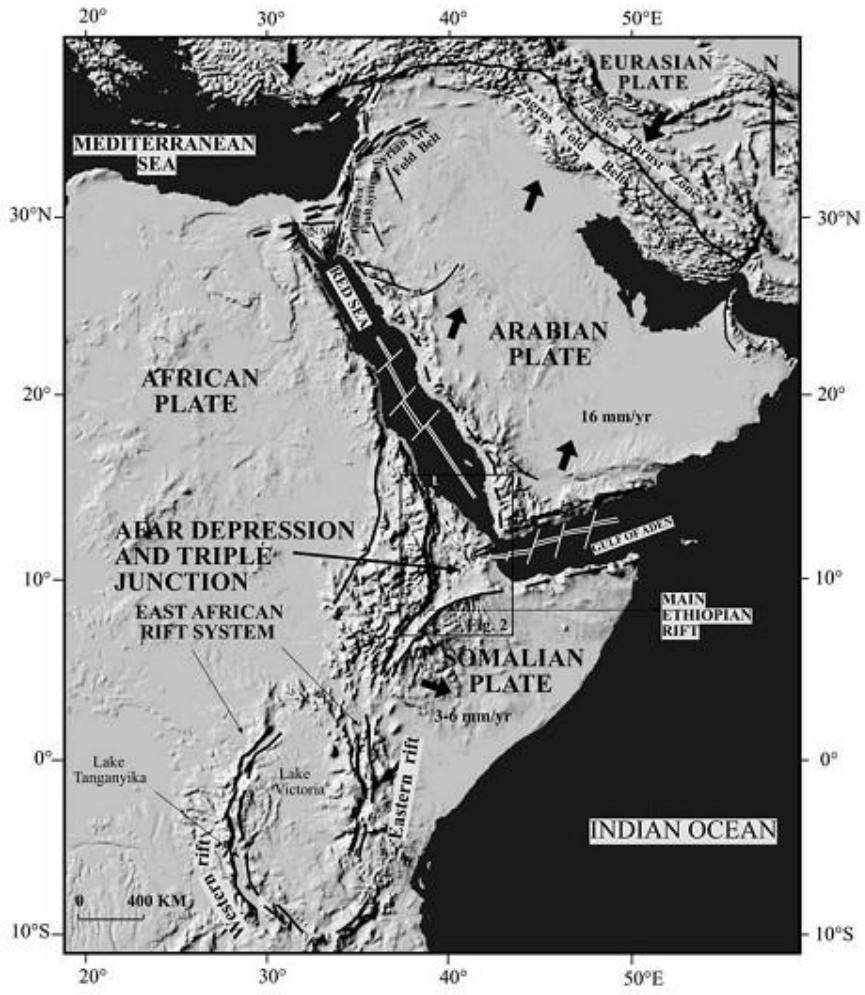

Figure 3.2 Digital elevation model of eastern Africa and Arabia showing the location of the Main Ethiopian Rift, Red Sea Rift, Afar Rift, and the Gulf of Aden Rift (from Samson Tesfaye et al., 2003).

together with the Neoproterozoic basement crop out extensively in the north-eastern part of the Danakil Alps. The top of the Mesozoic pre-rift stratigraphy is marked by a major unconformity, over which Ethiopian flood basalts or ‘‘trap series’’ have been extruded. This sequence reaches a preserved thickness of ~2 km and presently covers an area of ~0.6 million km^2 (Bosworth et al., 2005 & references therein). The trap series basalts erupted over a short period at ~30 Ma (Hofmann et al., 1997).

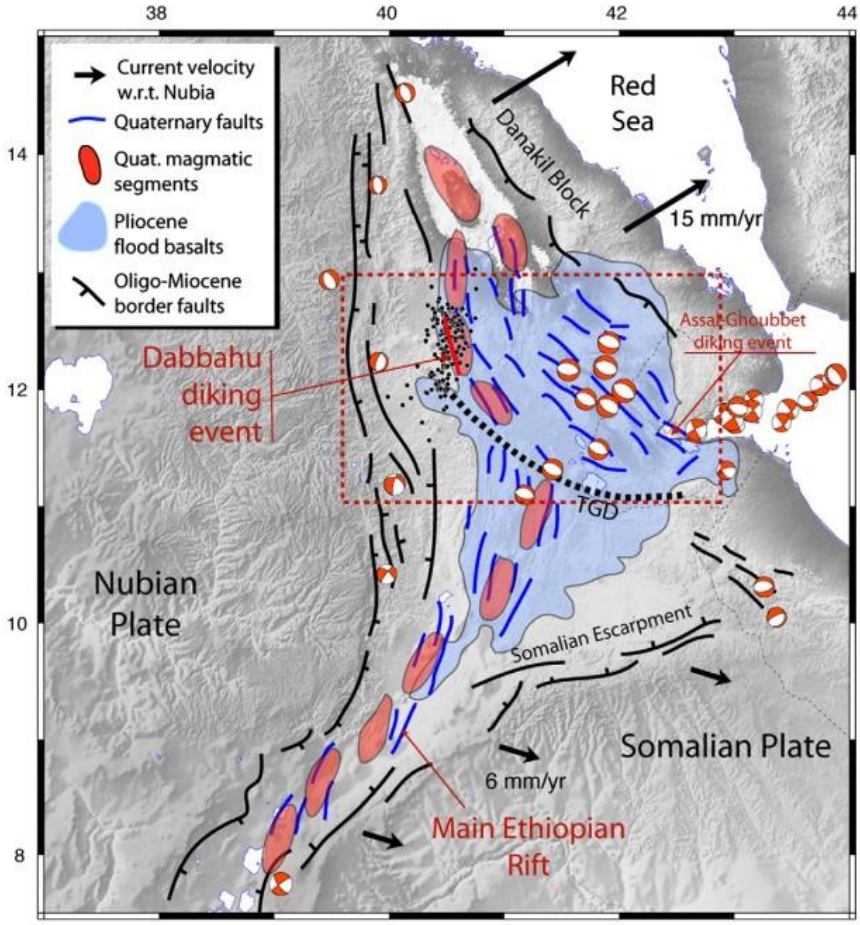

Fig. 3.3 Magmatic segments of the southern Red Sea, Main Ethiopian Rift, and westernmost Gulf of Aden Rift systems (Hayward and Ebinger, 1996). The Dabbahu magmatic segment entered a rifting phase in September 2005 (e.g., Wright et al., 2006).

3.1.2.2 Miocene (Syn-rift) Igneous Rocks

Younger Miocene igneous rocks within the Afar Depression include the Adolei, Mabla and Dalha Series. The Adolei basalts are found in a strongly tectonized area north of the Gulf of Tadjoura. The flows are highly altered turning dating difficult (Bosworth et al., 2005). The Mabla Series, which are found overlying the Adolei Series, consists of rhyolites and ignimbrites with minor intercalation of basalts. These were erupted along N–S trending vents. The top of the rhyolite sequence was significantly eroded prior to extrusion of the Dalha series, which also marked a return to basaltic volcanism (Bosworth et al., 2005). The Dalha Series is a basaltic sequence of up to 800 m thick interbedded with rare detrital sedimentary rocks and

ignimbrites (Alebachew Beyene & Abdelsalam, 2005; Bosworth et al., 2005 & references therein).

3.1.2.3 Pliocene–Pleistocene Volcanic Rocks

Pliocene to Pleistocene volcanic rocks cover most of the Afar Depression (see fig. 3.4). They are by far the most important geological units in terms of coverage and preservation of igneous features and tectonic activities. The most significant series of these is the Afar Stratoid Series which is separated from the Dalha Series by a nonconformity suggesting a prolonged erosion period characterized by reduced magmatic activity (Alebachew Beyene & Abdelsalam, 2005 and reference therein).

The Stratoid Series along with associated rhyolites of Plio-Pleistocene age covers more than 2/3 of the Afar Depression (Varet & Gasse, 1978; Alebachew Beyene & Abdelsalam, 2005; Barberi & Varet, 1977; Barberi et al., 1972b). About 2/5 of these volcanic rocks are basalts frequently found to be porphyritic, vesicular, and tholeiitic in their geochemical nature (Barberi & Varet, 1977). The thickness of the Stratoid Series reaches up to 1500 m with individual flows varying from 1 to 6 m (Varet & Gasse, 1978). The stratoid formation was built during Plio-Quaternary times, as all determinations fall in the range between 4.4 and 0.4 Myr (Varet & Gasse, 1978).

3.1.2.4 Quaternary Volcanic Rocks

Quaternary volcanic rocks in the Afar Depression are composed of basaltic flows, scoria cones, and silicic rocks. In most places, basaltic fissure eruptions were followed by central eruptions that produced differentiates of basalt comprising alkaline and per-alkaline silicic rocks. However, the rift-parallel axial ranges (within the SE-propagating Manda Hararo–Gobaad and the NW-propagating Asal–Manda Inakir rifts) in the northern and east-central Afar are dominated by basalts which are 1 Ma old. The Quaternary volcanic rocks, especially in the northern Afar are characterized by shield volcanoes. The axial ranges are forced along fissures showing symmetric magnetic anomalies that are underlain by thin oceanic-type crust, and get progressively younger from the marginal zones towards the axial zones (Barberi and Varet, 1977).

Because the axial ranges show characteristics similar to mid-oceanic ridges, Barberi and Varet (1977) considered those to be equivalents of oceanic spreading centres. E–NE trending volcanic centres transverse the NW– SE rifts found along the eastern and western Afar margins. These transverse volcanic centres are associated with fracture zones equivalent to oceanic fractures and composed of alkali basalts with inclusions of peridotite nodules indicating deeper mantle sources (Barberi and Varet, 1977). Central volcanoes called marginal centres are also found along the Afar margins. These are characterized by the occurrence of summit calderas and are mainly composed of trachytic and rhyolitic rocks.

3.1.2.5 Quaternary Sedimentary Units

Quaternary sedimentary rocks in the Afar Depression are dominated by lacustrine deposits. There are also conglomerate, marine limestone & corals, salt and gypsum formations. Lacustrine deposits are found mainly around Lake Afdera, and along the lower Awash basin, for example north of Mille (Barberi et al., 1973).

Danakil Formation

Danakil formation comprises marine sediments in the lower part and lacustrine sediments, in the upper part. This formation crops out only on the margins of the depression. The lower part of this formation is Early Miocene in age suggesting that the initial phase of the graben formation occurred at that time (Brinckmann and Kürsten, 1972).

Zariga Formation

The Depression has been flooded by sea water coming from the Red Sea at least twice during the Middle and Late Pleistocene (Foubert et al., 2015; Balemwal Atnafu et al., 2015). This led to the deposition of carbonate units surrounding the margins of the Danakil Depression. These carbonates constitute Zariga formation (see fig. 3.5) and at most places they directly overly the

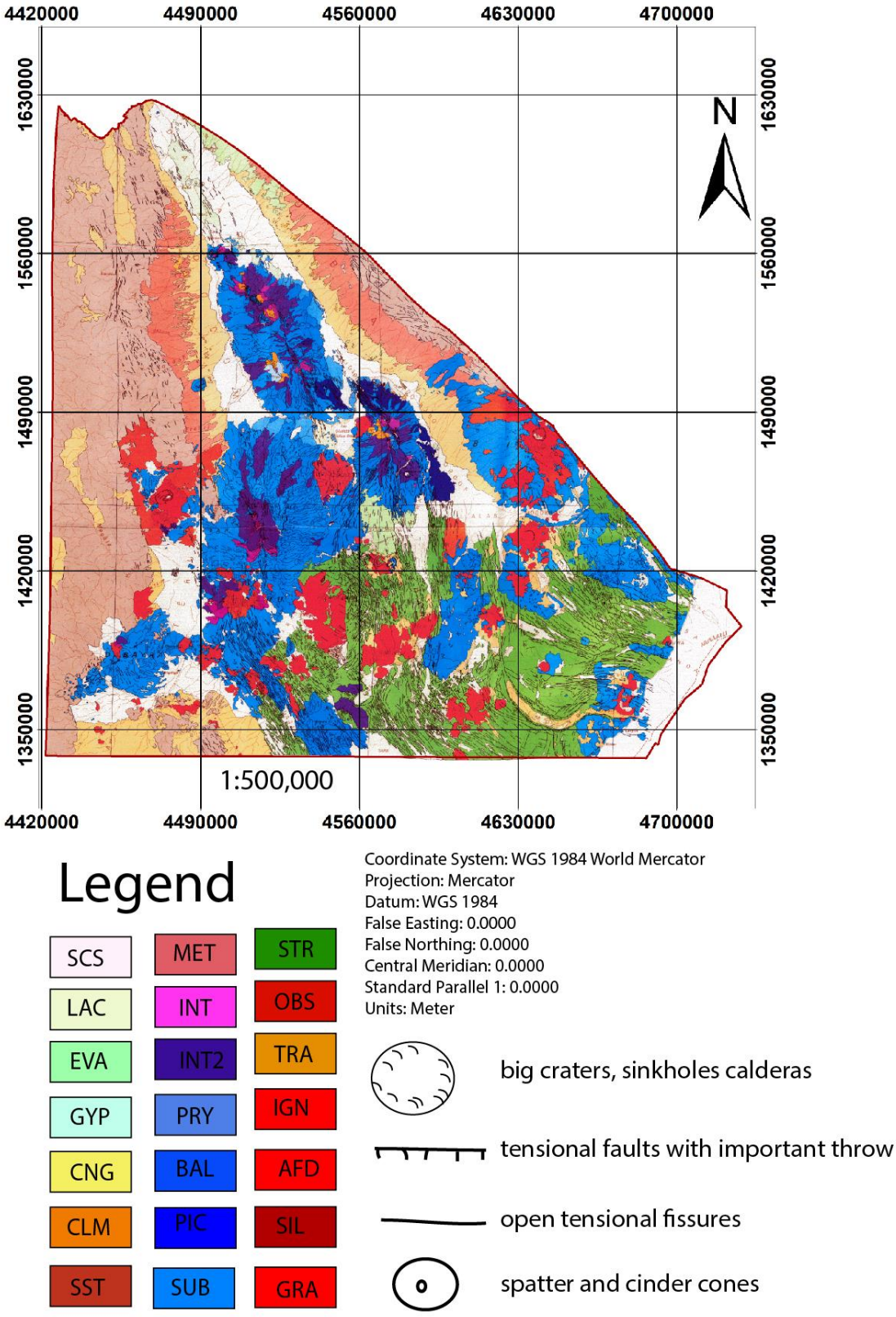

Fig. 3.4 Geological map of Danakil Depression, Northern Afar, Ethiopia (Barberi et al., 1973). Note the division of the Afar Depression into Northern, East Central, Southwestern, and South-eastern regions. Note SCS: silts, clays and sands (mud flats); LAC: lacustrine limestone and diatomite; EVA: evaporites (mainly

halite, potassic salts and salt domes); GYP: gypsum deposits bordering the Depression CNG: continental conglomerate; CLM: coral limestone locally gypsum; SST: sandstones, sands, red or polychromatic shales and associated volcanites; MET: epimetamorphic basement, granites, basic intrusions, Mesozoic cover (limestone and sandstone) and tertiary plateau traps; INT: lavas of intermediate composition (trachyte); INT2: lavas of intermediate composition (hawaiites, andesine basalts, ferrobasalts) ; PYR: basic pyroclasts of subaerial origin; BAL: basic lava flows, lava fields and related spatter cones, mainly basaltic composition; PIC: picritic basaltic flows and related spatter cones; SUB: basic subaqueous (submarine and sublacustrrine) lava flows, hyaloclastitic ash rings and layers locally covered by marine deposits (coral limestone); STR: recent traps of the Depression (stratoic basaltic lavas and ignimbritic sheets, locally covering rhyolitic massifs): submarine flows with pillow-lavas (MARSA FATMA); OBS: peralkaline rhyolitic obsidians (flows and domes); TRA: alkaline oversaturated trachytes, alkaline and peralkaline rhyolites, mainly in glassy flows and domes (Erta Ale Range); IGN: ignimbrites, pumice flows and pumice layers mostly of rhyolitic composition; AFD: intermediate and silicic lavas of Afdera volcano; SIL: silicic massifs, mostly of rhyolitic composition (lava flows and domes); GRA: alkaline and peralkaline granites and associated aplites and pegmatites intruded into the old tertiary traps of the Depression (Affara Dara massif).

volcanic substrates. The deposits range from open marine coralgal reefs, coastal oolithes to hypersaline microbial reefs deposited in lacustrine environments. Field investigation revealed four coralgal reef units separated by erosional surfaces within the oldest coral reefs (MIS7) evidencing the complexity of the system (Foubert et al., 2015;
Balemwal Atnafu et al., 2015). According to Jaramillo-Vogel et al. (2015) and Foubert et al. (2015) those units can be followed laterally for several kilometres (fringing coral reefs) and show distinctive biotitic composition. Deposits of MIS 5e are represented by scattered coral colonies or small patch reefs interfingered with ooid grainstones and covered by evaporitic deposits. The marine to hypersaline units are intercalated with volcanoclastic layers and are overlain by gypsum. Based on four K/Ar age determinations on sylvite at 73 and 210m depth into drill holes taken within the frame work of the early potash exploration (i.e., between 76 and 88 ka) (Hutchinson and Engles, 1970) the evaporites are believed to correspond at least partly to the Zariga Formation (Foubert et al., 2015; Jaramillo-Vogel et al., 2015; Balemwal Atnafu et al., 2015).

Afrera Formation

This formation is separated from the Zariga Formation by Late Pleistocene to Holocene fluvial sands and gravel on top of the gypsum deposit (see fig. 3.5). Afrera Formation is characterized

by lacustrine marls, carbonate, diatomites and evaporitic deposits locally interbedded with hot-spring build-ups representing respectively seasonal terminal saline lakes and geothermal pools (Foubert et al., 2015). According to Foubert et al. (2015) Holocene brackish and hypersaline lacustrine deposits belonging to the Afrera Formation are present in the central and southern part of the Danakil Depression at elevations ranging between -120 and -70m.

Older Terraces, Younger Terraces and Fluviatile Gravels

Conglomerates cover the base of the escarpment and the tertiary formation which flanks it. These form large alluvial fans encasing each other. Salt (halite) forms the floor of the Danakil Depression in the Dallol-Assale region, and beneath part of the Erta Ale range (Barberi et al., 1973). Gravel terraces of detrital and fluvial origin are intercalated in between the Danakil, Zariga and Afrera Formations (see fig. 3.5). River sands constitute the recent deposits in the graben area.

3.1.3 Regional Structures

According to Hayward and Ebinger (1996) the overall structural trend of the Afar Depression shows a temporal variation in fault length within each Afar rift sector. The older, longest border fault segments and highest fault escarps are preserved at the plateau whereas the younger, shortest border fault segments and lowest escarps flank the Quaternary rift basins where the crust is the thinnest indicating the active faulting concentration along narrow zones within the centre of wider rift systems. This is due to the decrease in the strength of the lithosphere with increasing strain rates and magmatism (Hayward & Ebinger, 1996).

The Afar Depression is dominated by three structural trends (Barberi et al., 1972b): (1) a NNW trend that parallels the Red Sea along which the axial basaltic ranges of northern Afar are oriented; (2) an E-W trend that runs through the Gulf of Aden and continues onto land at the Gulf of Tadjura in Djibouti; and (3) A NNE trend of the northern Main Ethiopian Rift (see fig. 3.6 below). The dominant structural elements of the Danakil Depression belong to the NNW Red Sea system (Beyth, 1991 and references therein).

Statistical treatment of faults mapped in the northern Afar Depression indicate N20^{0}W is the most representative of the strike of the faults in the northern Afar Depression (Barberi et al., 1973). According to Barberi et al. (1973) SE & NE of the Afdera volcano NE trending sets of faults are present. These faults represent transverse structures interpreted as a pre-rift line of weakness, reactivated several times during the main tensional events which produced the depression. The NE trending faults cannot be interpreted as transform faults since this alignment is volcanically active and that transform faults are not the loci of volcanic activity (Barberi et al., 1973). The NNW tectonic trend is prevalent in the northern and central Afar Depression (Hayward & Ebinger, 1996). Samson Tesfaye et al. (2003) noted that the central and southern Afar are dominated by horst and graben structures. Accordingly, the grabens in the central Afar strike NW whereas those of the Southern Afar strike N-NE.

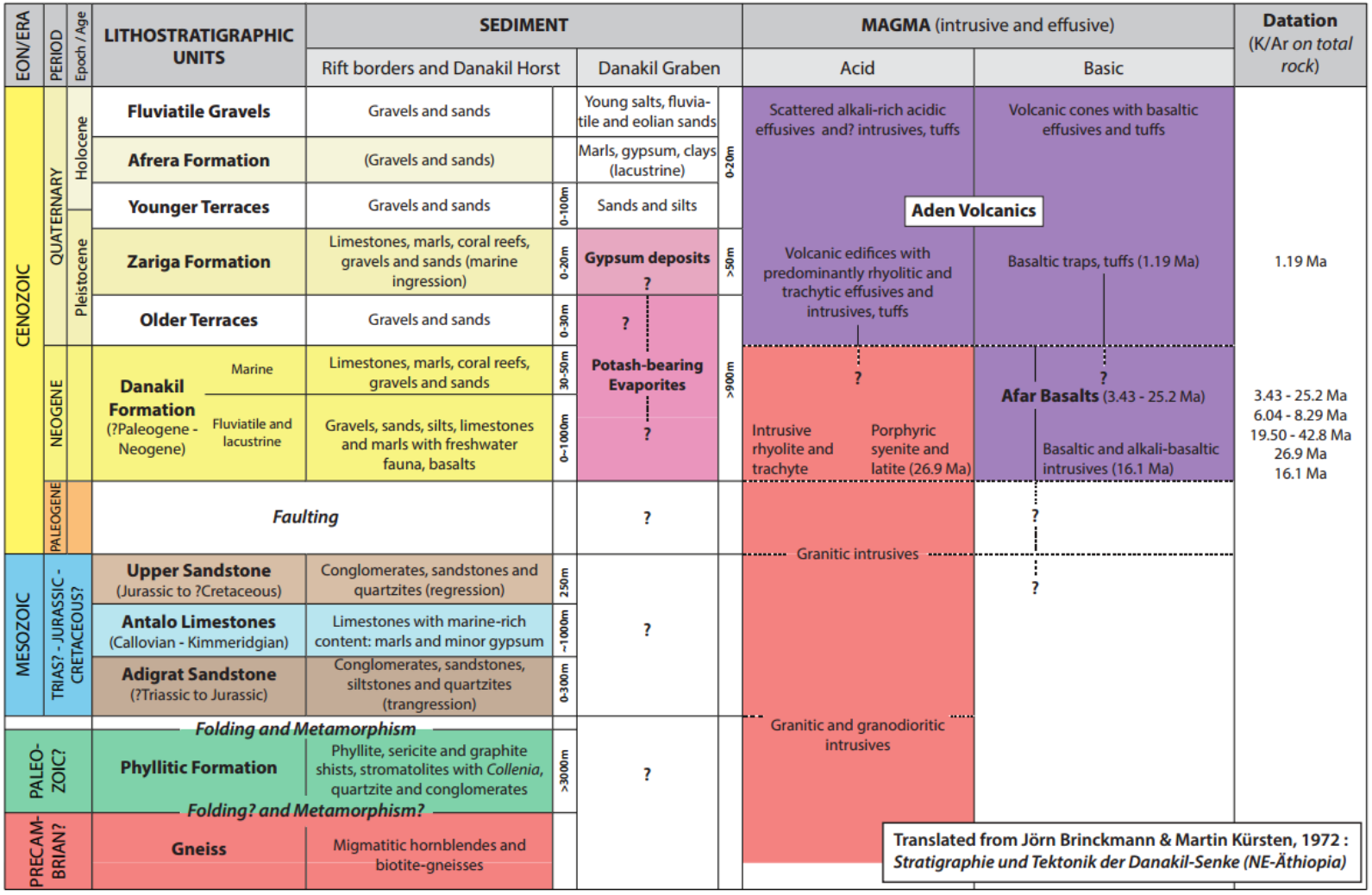

Fig. 3.5 Stratigraphic column of the Danakil Depression (after Brinckmann & Kürsten, 1972)

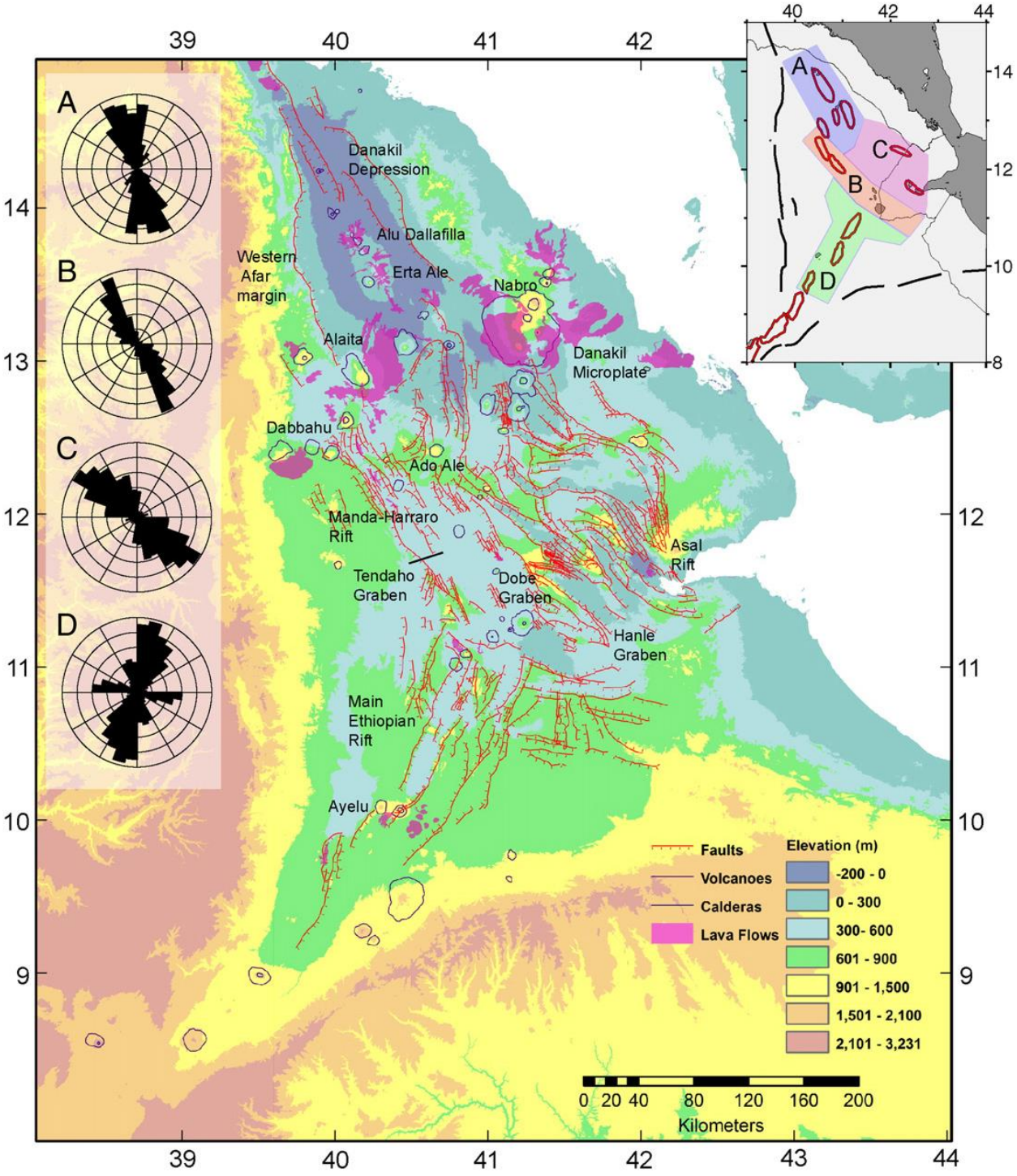

Fig. 3.6 Topographic and structural map of the Afar Depression. Major Pliocene–Recent faults are marked red. Recent basaltic lava flows are shaded light purple. The inset delineates the major rift system forming the Afar triple junction. The subaerial Red Sea rift is included in areas A (Danakil depression) and B (Manda– Harraro rift and Tendaha graben). The subaerial Aden rift is included in region C, and the northern Main Ethiopian rift is area D (from Keir et al., 2013).

3.2 Geology of the Study Area

Landsat 8 image of the study area was used as a base map to perform geological and structural mapping. Field observation enabled to construct spectral reflectance curve (see fig. 4.18) for each lithologic unit mapped. This reflectance curve allowed to distinguish different lithologic units where access was not possible.

3.2.1 Lithologic Units

3.2.1.1 Precambrian Basement Rocks

This lithologic unit is found exposed along the western edge of the study area. It covers an area of 486 km^2 within the study area. It is found exposed forming extensive ridge topography from north to south. Common crystalline basement rocks within the study area are phyllite and slate. These basement rocks exhibit prominent foliations which are trending either in the NE or NNW direction. For instance, where slate is found exposed forming small ridge, (see fig. 3.8) it has general attitude of $170^0/80^0$SW. The common lustrous sheen foliation surfaces of phyllite are not clearly seen, at some localities, due to intense alluvial mass movement from the plateau through these surfaces resulting in dull appearance. The freshly broken surface of the phyllite rock exhibit silky sheen appearance and has light green colour and its weathered face is light greyish and brown. The observed slate has dull appearance on its freshly broken surface.

3.2.1.2 Sedimentary Rocks

Sedimentary rocks within the study area comprise limestone, sandstone, gypsum and associated coral reefs, beach deposits, lacustrine and alluvial sediments and conglomerate as well as salt formation; and are exposed along the peripheries and plateaus and covering the flat area as well. These units cover a total area of 1400 km^2 within the study area.

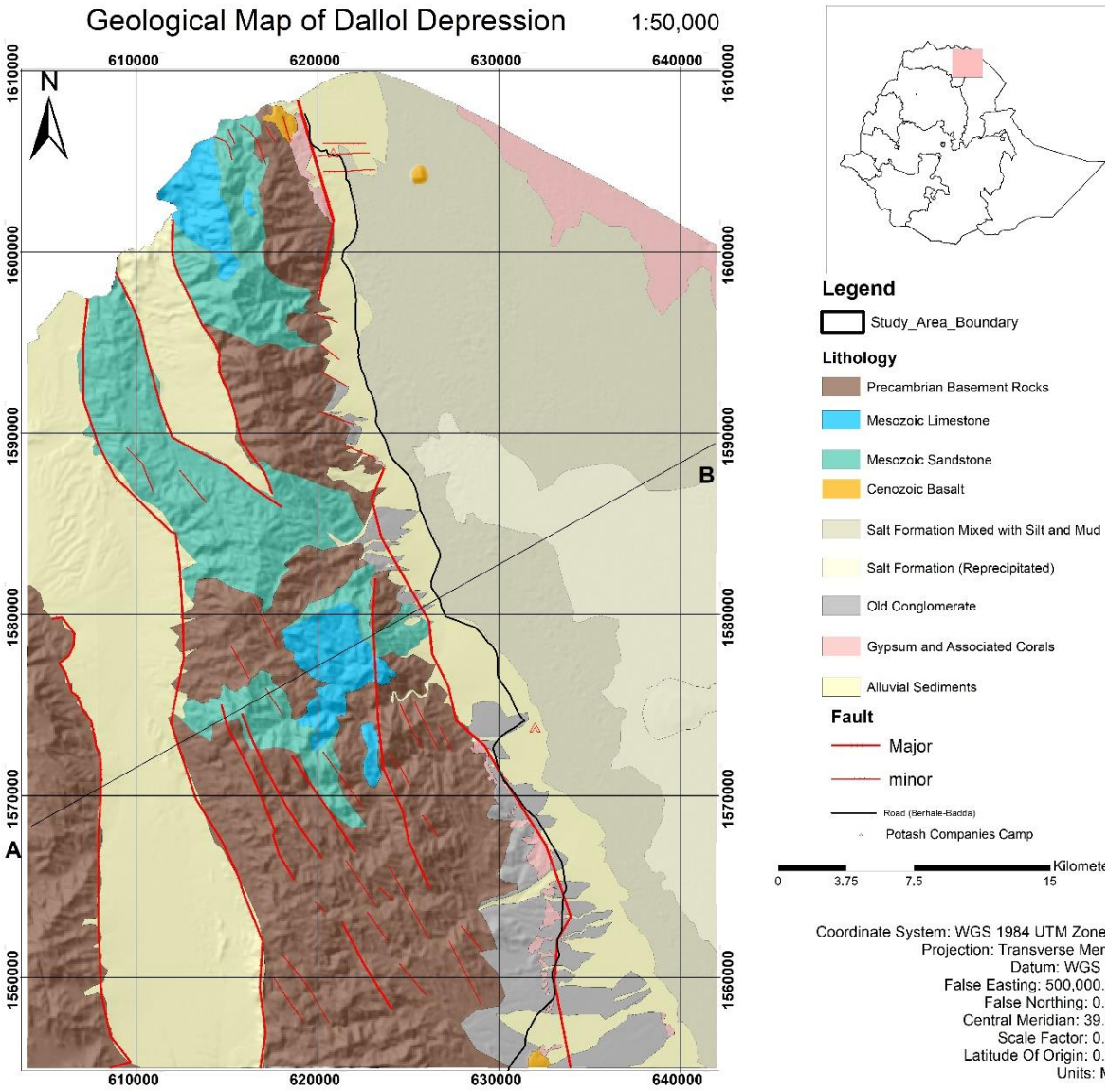

Fig. 3.7 Geological map of the study area

Gypsum and its associated corals covers about 48 km^2 of the study locale and it is distributed on the eastern edge of the ridges west of the alluvial fans. It is usually found as patches aligned in NNW direction here and there along those edges. This rock unit is found exposed forming canyon on the north edge of the mapped area (see fig. 3.9 a below). As can be noted in fig. 3.9 b generally NNW trending cracks characterize this lithology. It is characterized by white appearance, soft hardness, and horizontal to sub-horizontal layering and where it is exposure forming a canyon it shows laminations (see fig. 3.9 a). Gypsum is usually found overlying coral reef outcrops. Coral reef facies comprise, tropical coralgal species, echinoids, numerous gastropods and bivalves, including tridacna.

Lacustrine sediments varying from 1 to 5m in thickness appear bedded and show bioturbation. Field observation revealed that these sediments generally occur below marine sediments and contain lacustrine gastropods (see fig 3.10 below).

Beach deposits within the study area are found exposed in flat topography (see fig. 3.9e). These deposits contain cemented lithoclasts, bioclasts, ooids and oncoids and large aligned pores visible with the naked eye.

The alluvium covers central part of the study area. These sediments also cover the floor of the marginal graben (see fig. 3.7). Quite large area about 460 km^2 is covered by the alluvium. It is found forming alluvial fans. The alluvium contains all range of rock fragments from the boulder size to the silt and clay size where the larger fragments are found close to the ridges from where they are coming. Close to the salt plain silt and clay size alluvium dominates over the larger grains. The alluvial fan sediments are found deposited in the border region between the Ethiopian highlands and the Depression. They are deposited from ephemeral water flow from the NW Ethiopian highland during extreme rain storms. These sediments dip to the centre of the depression. The alluvial sediments cut through the old conglomerate and they are aligned NNW. Older conglomerate deposits which appear darker in the natural Landsat 8 (4-3-2) dissect the gypsum and coral reef and they are in turn cut by the recent alluvial sediments (see fig. 3.9f). These conglomerate deposits contain different rock fragments (clasts) mainly of the basement rocks and are clast-supported. Thus, these polymictic conglomerate deposits are epiclastic according to the genetic classification of conglomerates (Boggs, 2006).

Fig. 3.8 Slate exposure exhibiting prominent foliation

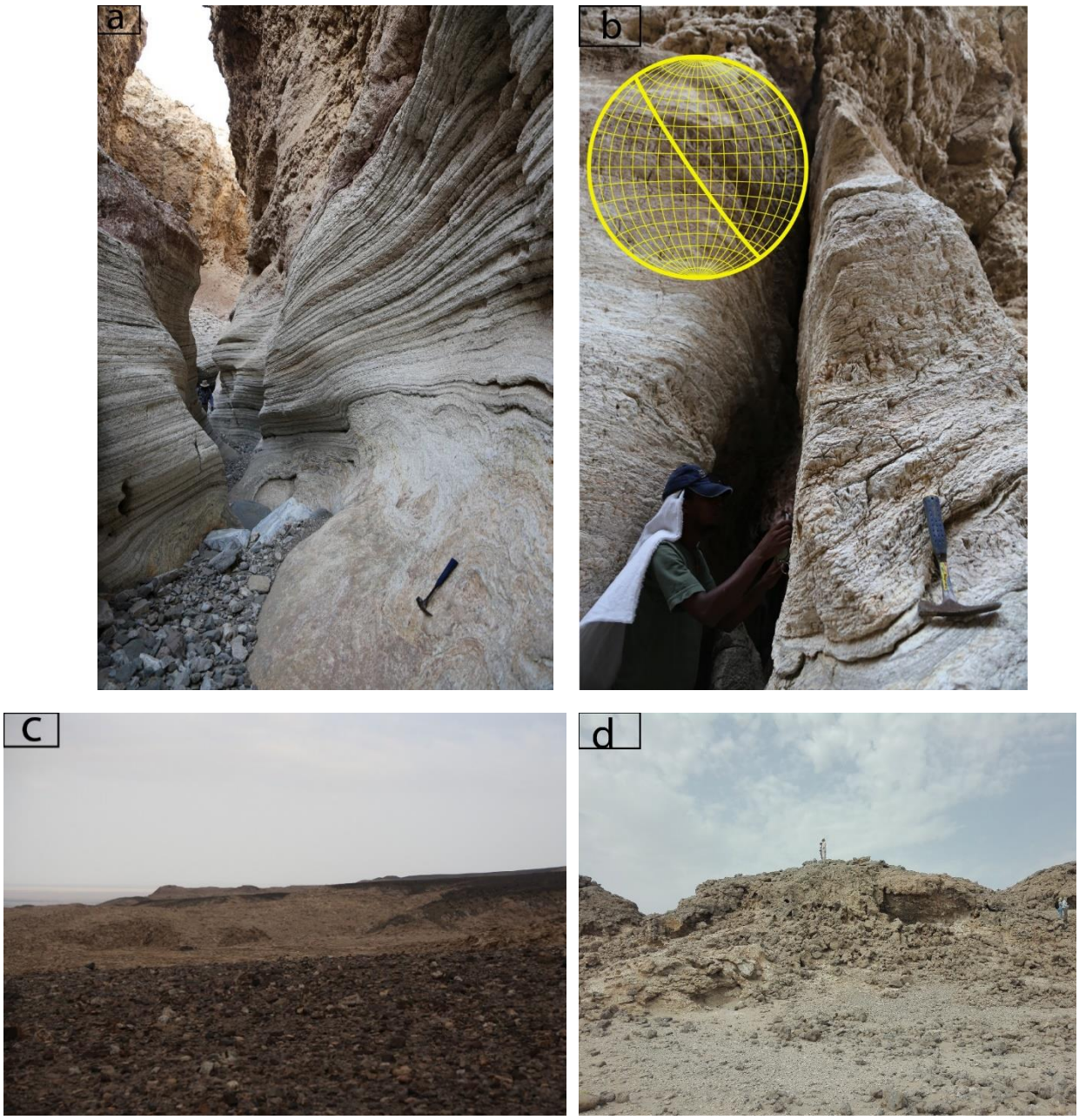

Fig 3.9 sedimentary rocks in the study area (a) gypsum forming canyon (b) gypsum with NNW trending cracks (c) gypsum horizontal to sub-horizontal layering near Badda Village (d) coral reef outcrop in the southern part of the study area (e) beach deposits (f) recent alluvial sediments which cut through the old conglomerate (g) salt cover surrounding Dallol area

Fig 3.9 (continued)

The salt formation sequence covers the flat topography and has an areal extent of >600km^2. It is comprised of halite particularly in the Dallol mound. Adjacent to the alluvial fan deposits it is mixed with mud and silt materials which are left by the transportation of mass of sediments from the Ethiopian Plateau. Surrounding of the Dallol mound manifest the occurrence of sulphur/sulphide giving the province a rotten-egg smell.

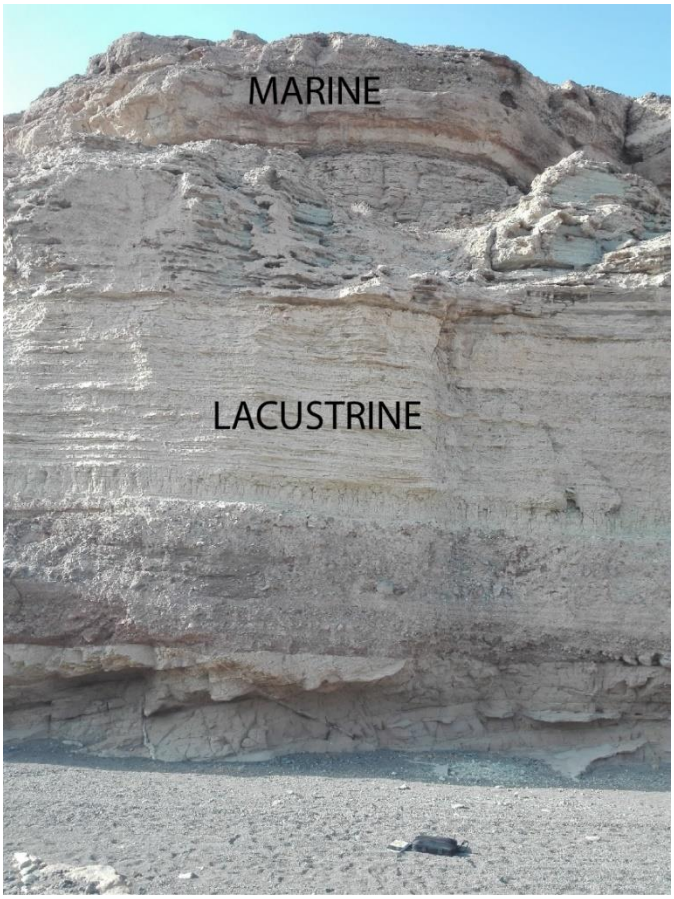

Fig. 3.10 Bedded lacustrine sediment below marine sediment

Coral Reefs

Coral reefs are geographically distributed along the slope of the western margin of the Danakil Depression in the north and south. In the north Coral Outcrop (CO) 6, CO16-19 constitute site A, B and C and CO 1-4, C07, CO11-12 and CO14 constitute site D and E in the south (see fig. 3.11a). The elevation measurement from dGPS and DEM indicate that altitudes for a given sequence vary greatly from the south to the north where it tends to increase towards the north. Lower altitudes were observed in outcrops CO18 (see fig. 3.11d), CO19 (see fig. 3.11c) and CO17 (see fig. 3.11b) than the general trend would suggest (see table 4.2). Many of the coral outcrops show good preservation particularly in CO07 (see fig. 3.11g) and CO14 (see fig. 3.11f) even though some outcrops show bad preservation, for instance CO16 (see fig. 3.11c) and C017 (see fig. 3.11b). At some places, for instance in CO19, alternation between marine and lacustrine units is observed. In many places outcrops are incised by several river channels. Lateral variation of carbonate facies was seen in outcrops, for example in CO04. Along CO1, CO12 and CO7 two generations of corals can be observed separated by an erosional surface in

CO1 and CO12. Corals of younger generation in the northern part are frequently covered by gypsum. Field observation revealed that the older coral generation is general located stratigraphically above the younger corals.

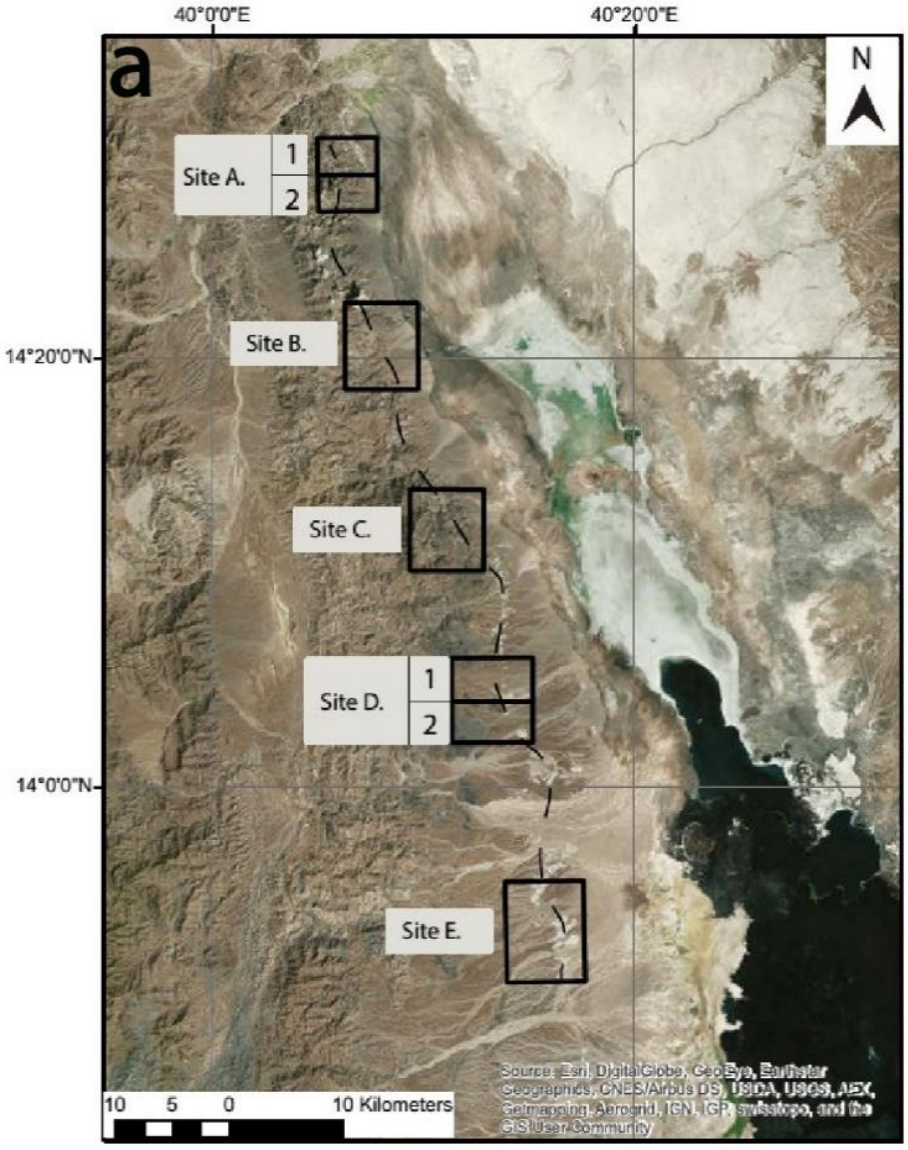

Fig. 3.11 Distribution of Coral Reefs and surrounding units (a) map showing the detailed map sites and each outcrop (b)CO17 (c) CO19 & 16(d) CO18 (e) CO06 (f) CO4 & 14 (g) CO1, 2, 12 & 17 (h) CO3 & 11

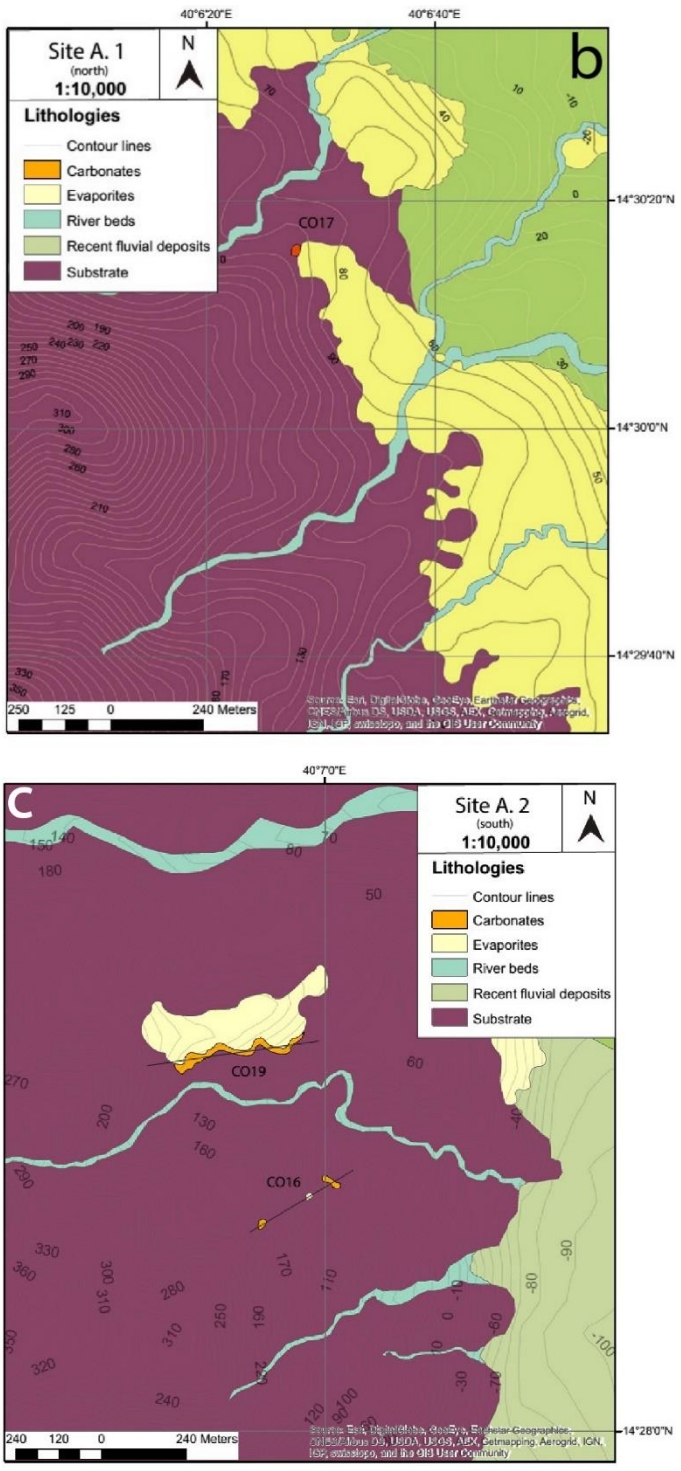

Fig. 3.11 (Continued)

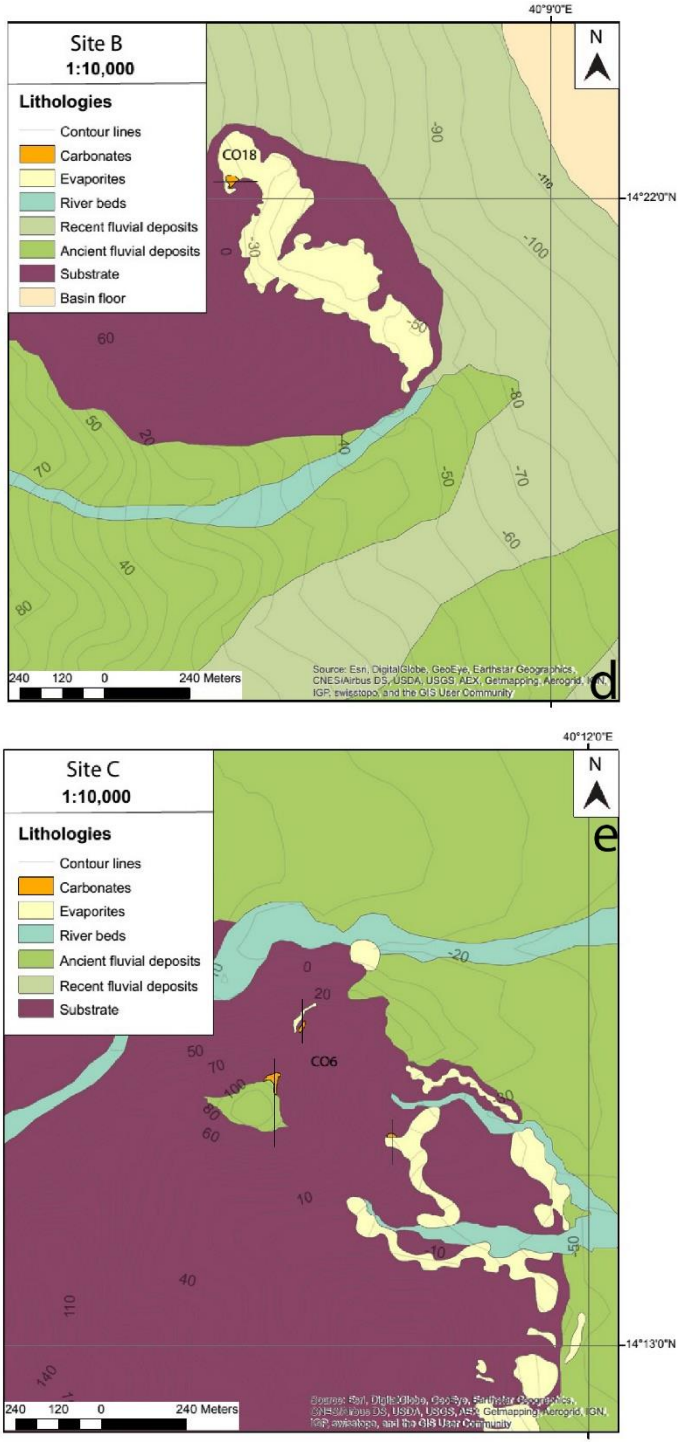

Fig. 3.11 (Continued)

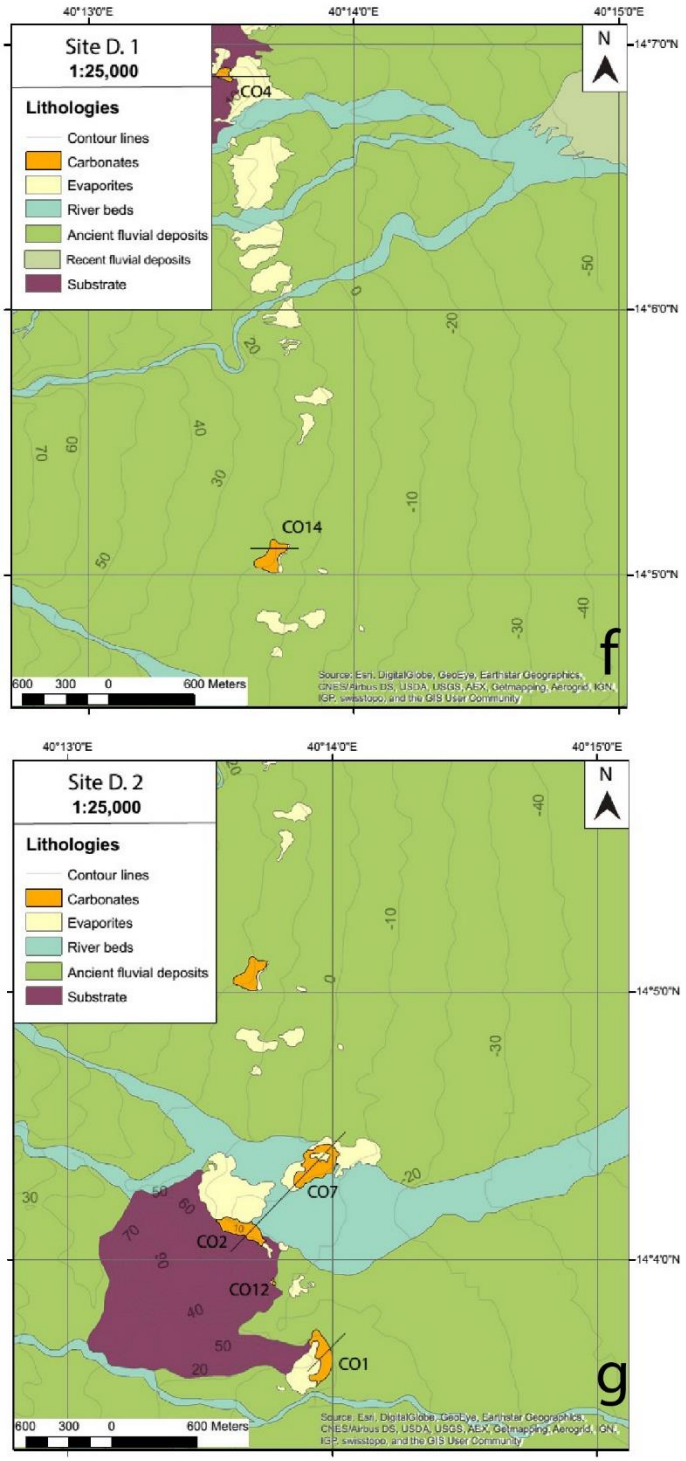

Fig. 3.11 (Continued)

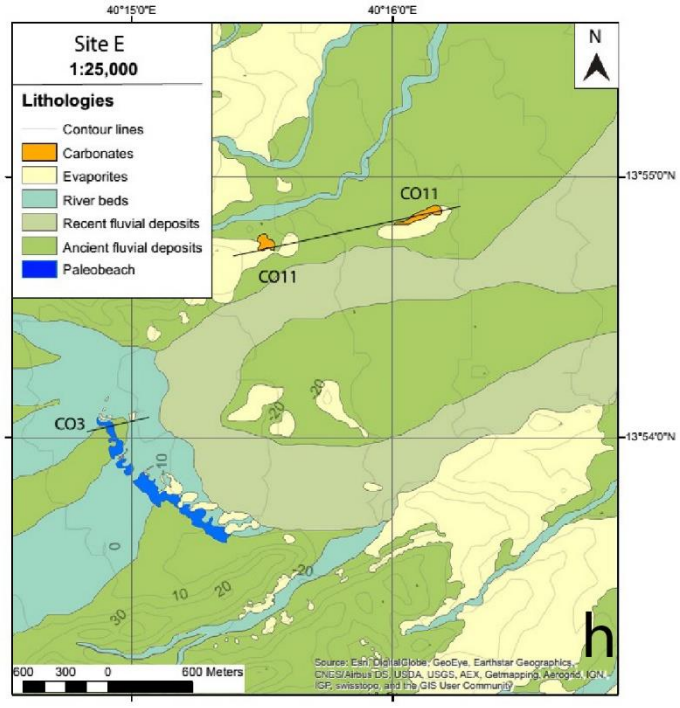

Fig. 3.11 (Continued)

3.2.1.3 Volcanic Rocks

The volcanic rocks mainly comprise basalt which is exposed on the northern tip and farther south of the study area covering an area of about 3.5 km^2. In these places, it is found overlaid by coral reefs surrounding it. This unit is vertically jointed (see fig. 3.12b) where the joints are trending generally NNW with some deviation of this trend to the N-S and NE (also see table 3.1). Hence, basalt forms cliff topography with its columnar jointing. Texturally the mapped basalt is aphanitic to vesicular. Pyroclastic fall deposits are also observed in the northern part of the study area. These fallout from a vertical eruption may have accompanied the small basaltic eruptions which produced Maraho scoria cones (Winter, 2001 page 56). The fall deposits are typically well sorted and display plane parallel beds. Volcanic bombs were also noticed (see fig. 3.12c & d).

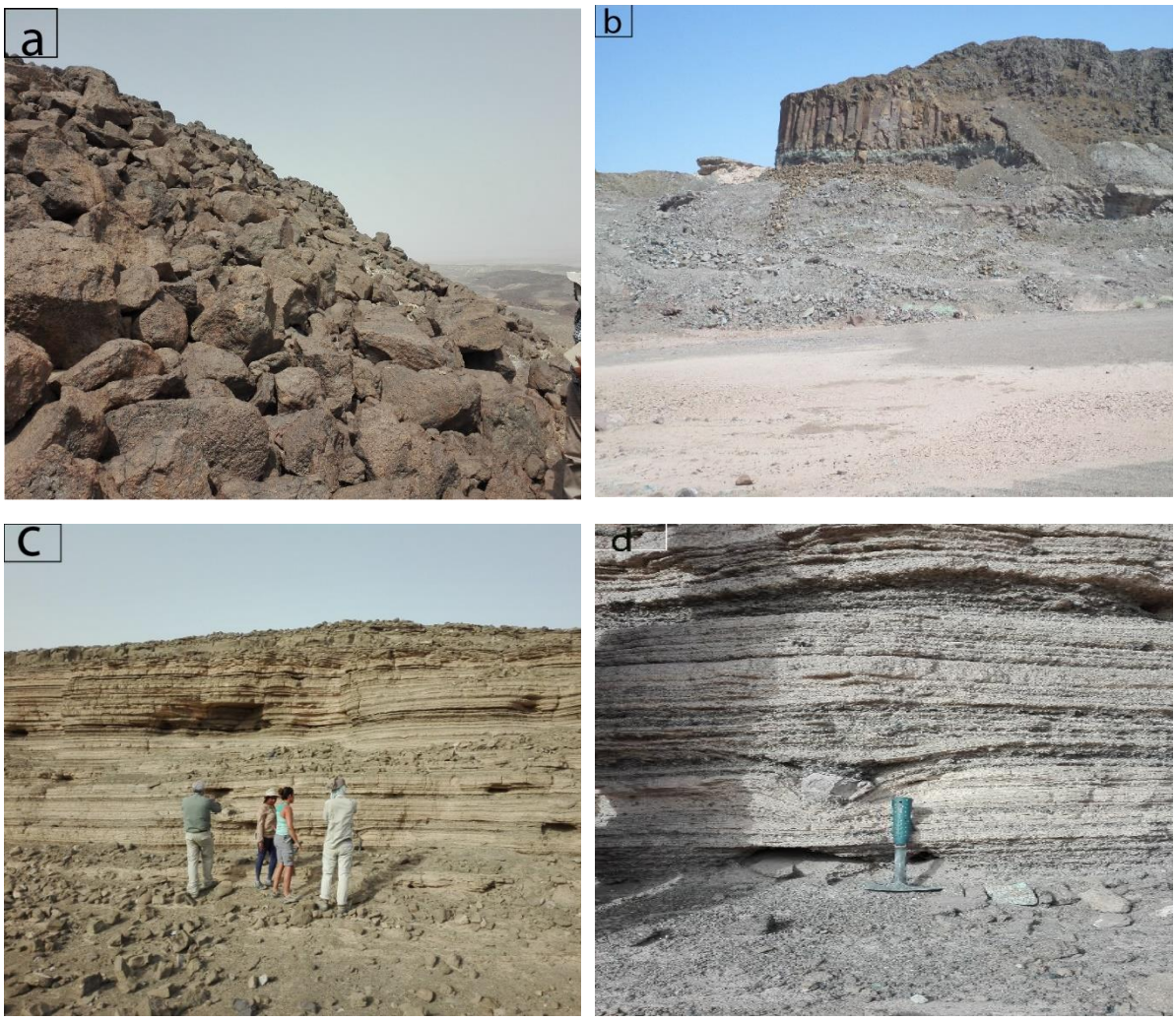

Fig. 3.12 Basalt and pyroclastic fall outcrops in the northern part of the study area (a) basalt with few coral reefs (b) basalt with columnar jointing (c) stratification in pyroclastic fall deposit (d) bomb in a pyroclastic fall deposit

3.2.2 Geological Structures

3.2.2.1 Faults

The fault structures in the study area are difficult to map; one because the area is covered by recent alluvial sediments and the other is that the province is found close to the Ethio-Eritrea Border due to which there is no access. Hence there were only few structural measurements taken from the field. The observed faults have no perfect planar surfaces that several strike and dip measurements are taken to describe the attitude of the faults. It is noted that the faults change attitude both along strike and up and down dip. As most normal faults the faults observed are high angle faults where their dips range from 65^0 to 85^0. Many of the faults in the

study area are recognized by the presence of stratigraphic discontinuity where juxtaposition of rocks that do not belong together in an undisturbed geologic sequence are observed. Most of the measured faults are localized in the northern part of the study area along the ridge topography dissected by the modern streams.

One is that which juxtaposes phyllite rock with conglomerate unit. It is a normal fault where the hanging wall constitute the conglomerate unit whereas the footwall comprises the phyllite unit. This fault is steeply dipping fault with 70^0 dip amount and it trends generally NNW paralleling the southern Red Sea trend. The measured distance between the fault planes (see fig. 3.13 below), width of the fault, is 11m. The lithologic units above and below the fault plane are dipping to the SW general direction and trending NE. This fault is directly observable in excellent natural stream cut exposure and recognized in the field by stratigraphic lateral discontinuity of conglomerate rock unit.

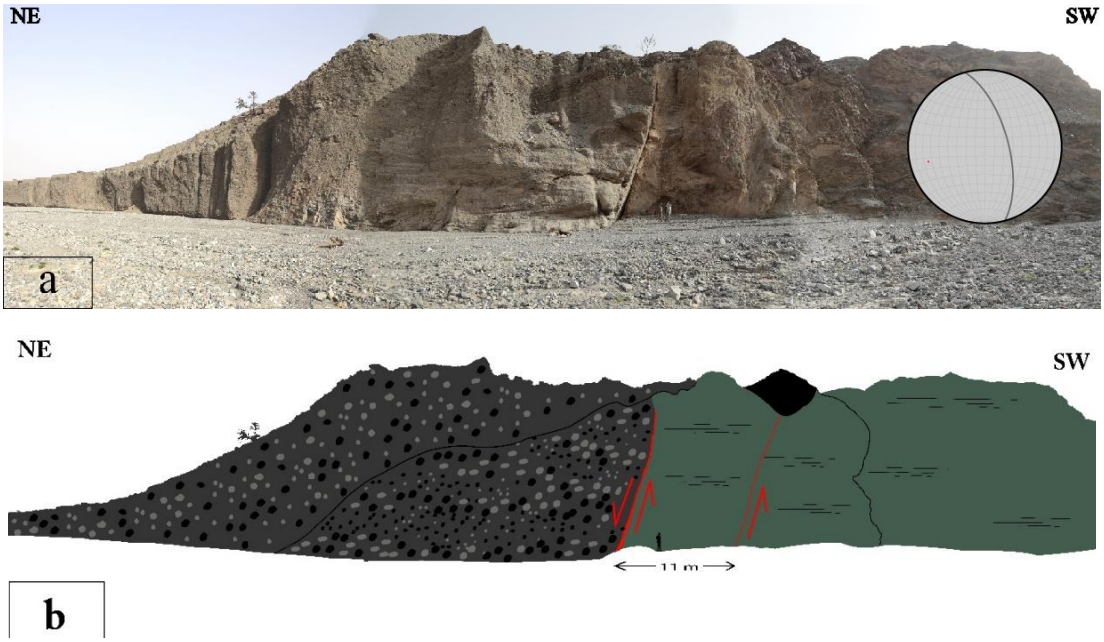

Fig. 3.13 normal fault juxtaposing phyllite and conglomerate (a) panoramic view (b) interpretive sketch

Abrasion by the wall rock and the fault-zone fragments produced grooves (fig. 3.14a below). These grooves have rake of 40^0 which is measured from the 307-strike direction of the plane with an attitude of 307/65NE. This fault also exhibits a series of subordinate faults close to each other which are arranged variably defining a zone (see fig 3.14 b). This fault zone has a width of 11 m.

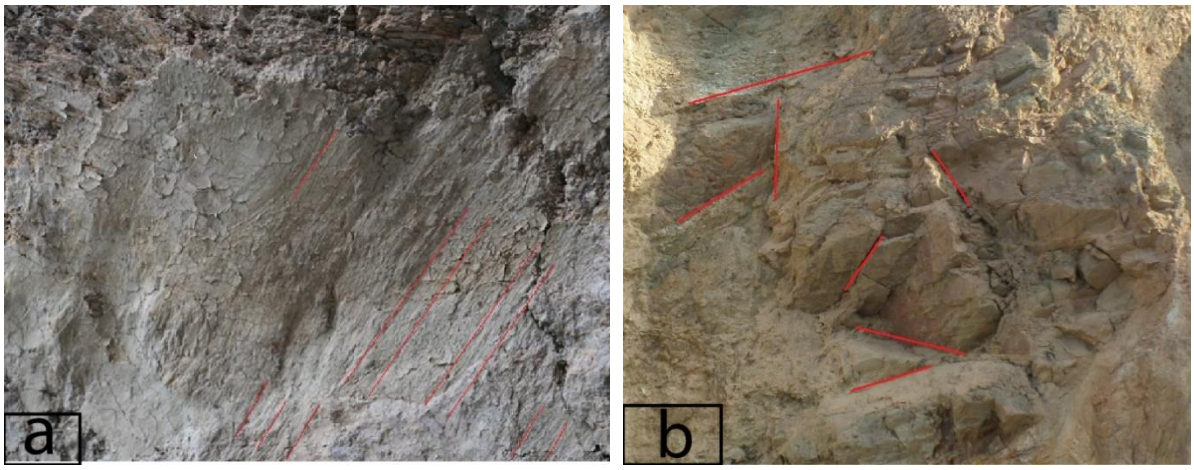

Fig. 3.14 Grooves on a fault plane (a) and (b) fault zone with faults having different orientation indicated by thin red lines

Another fault measured in the field is found close to the Ethio-Eritrean Border. It is a high angle normal fault with an attitude of 190/70E. It is well exposed by stream which runs from the plateau to the depression. The fault is revealed by the discontinuity of the lacustrine sediments in the stratigraphic sequence. At the base of the hanging wall there is a few-meters-wide drag zone which displays change in the orientation of the lacustrine sediments (see fig 3.15). Striation measured on the slickenside of this fault (see fig. 3.16) has a rake of 70^0 from the SW end of the strike of this fault plane.

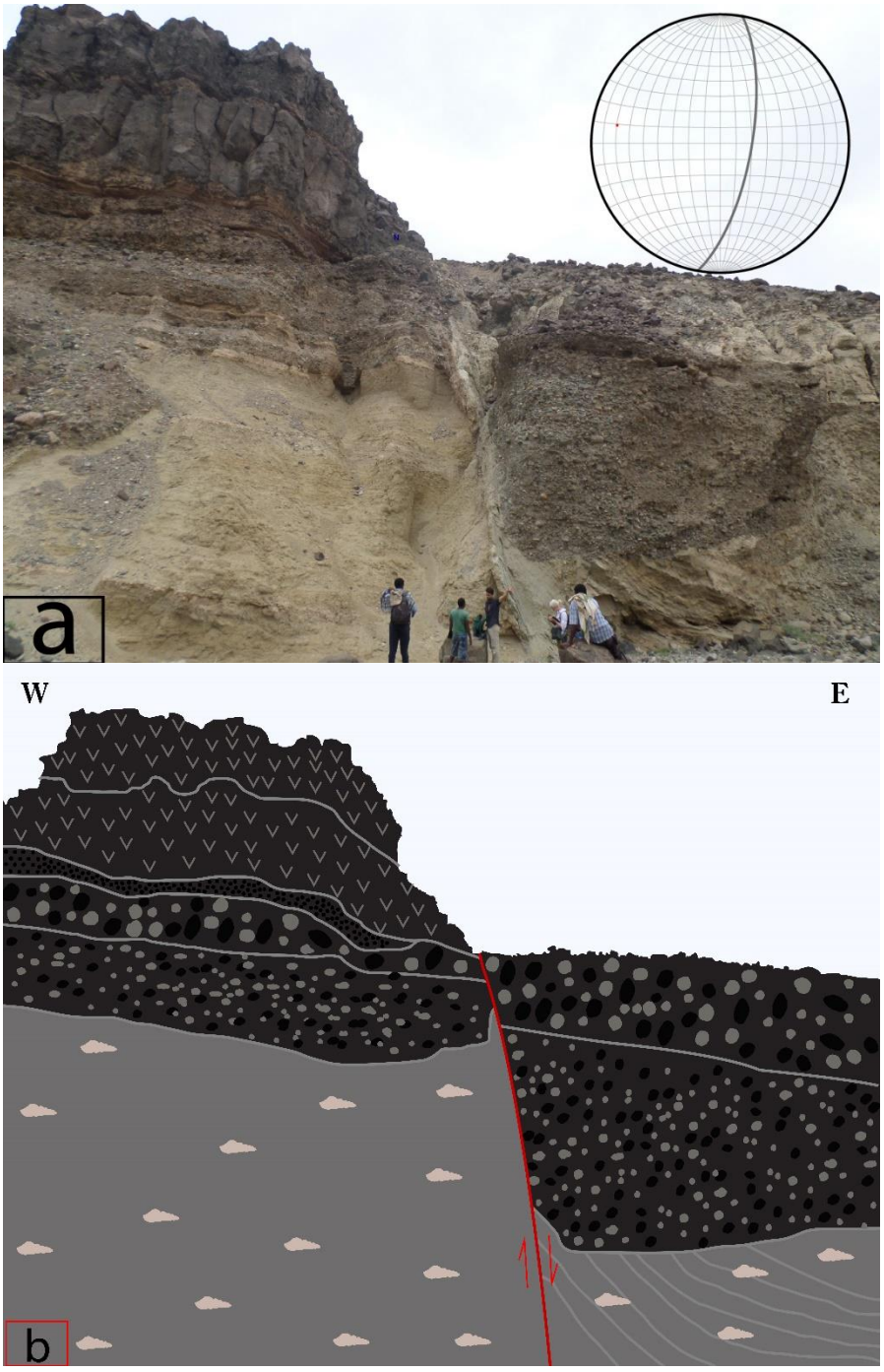

Fig. 3.15 normal fault affecting basalt, conglomerate and lacustrine deposit (a) field photo with stereoplot. (b) Interpretive sketch. Note also the drag zone at its base on the hanging wall.

Along ephemeral stream channel in the northern part of the study area a fault put lacustrine sediment and conglomerate rocks together (see fig. 3.17). This fault has a general attitude of $353^0/73^0$E. Apparent displacement of 25 m was estimated by measuring elevation of lacustrine sediment on the hanging wall and footwall side of the fault plane with ordinary GPS. The fault plane shows white coloured hardened surface along which fluid has moved. Vertical fault

which displaced basaltic lava with an attitude of 320^0 (see fig. 3.18) is also observed in the field. The basaltic lava flow sits on top of lacustrine sediment. The basaltic lava that comprise

Fig. 3.16 striation on fault plane

Fig. 3.17 normal fault putting together conglomerate and lacustrine sediment (a) field photo (b) interpretive sketch

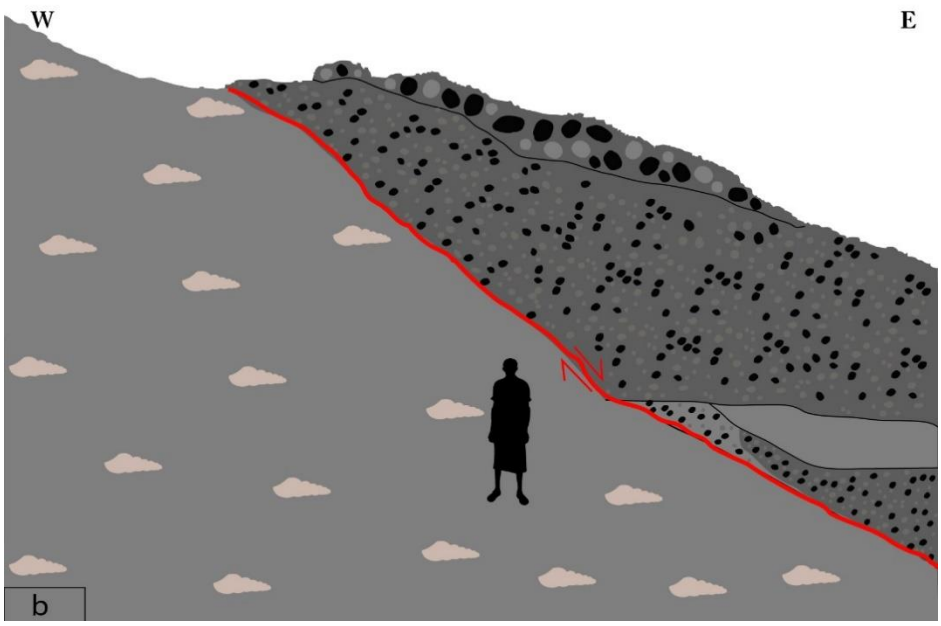

Fig 3.17 (continued)

the eastern block seem rotated counter clockwise but this cannot be confirmed from far distance in a situation where there is no closer access to the fault. Conjugate set of normal faults (see fig. 3.19) measured in the field affect intensively weathered lithology beneath basaltic lava close by Hamadela village. The road which run from Hamadela to Dallol expose these set of oppositely dipping normal faults.

Fig. 3.18 fault displaced basaltic lava (a) field photo (b) interpretive sketch

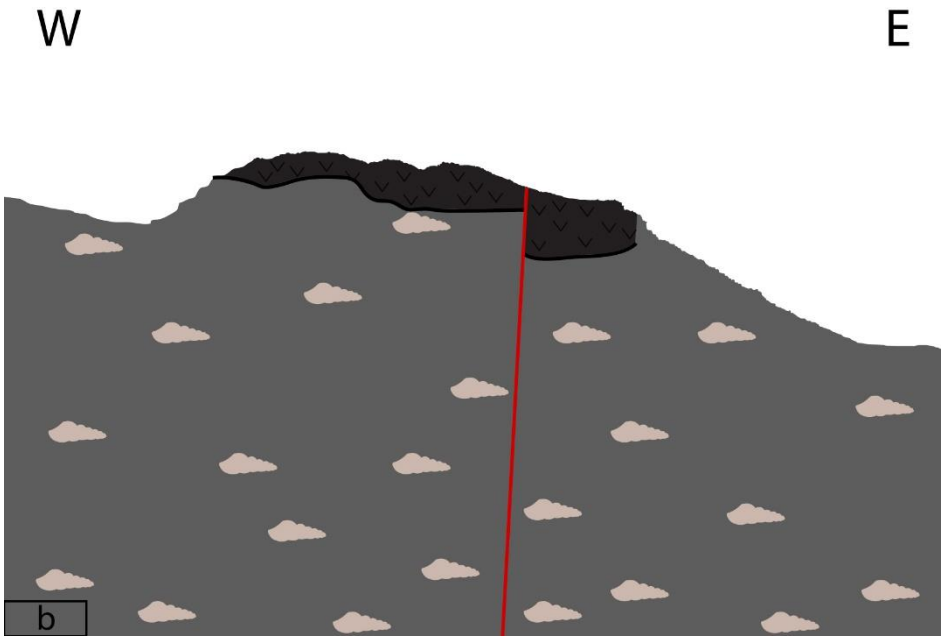

Fig. 3.18 (continued)

The measured orientation of these faults is N10^{0}E, 75^{0}E and S20^{0}E, 75^{0}W. In the central part of the study area along one of the ephemeral streams a fault with an attitude of 335^0/55^0 SW displaced 20 cm thick lacustrine sediment (see fig. 3.20). The lacustrine sediment is found as a lens within inclined conglomerate unit below an angular unconformity between horizontal conglomerate and tilted conglomerate.

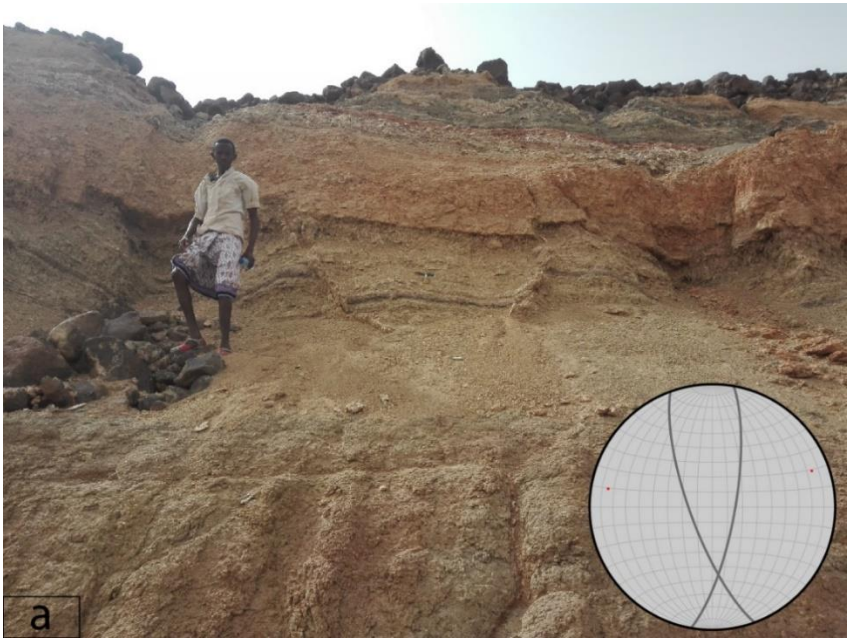

Fig. 3.19 Conjugate set of faults around Hamadela village (a) field photo (b) interpretive sketch

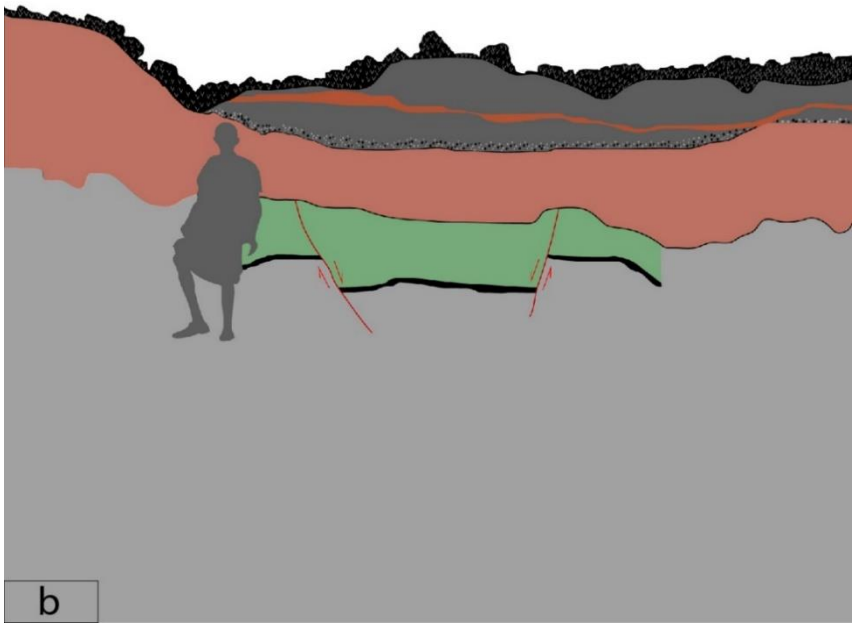

Fig. 3.19 (continued)

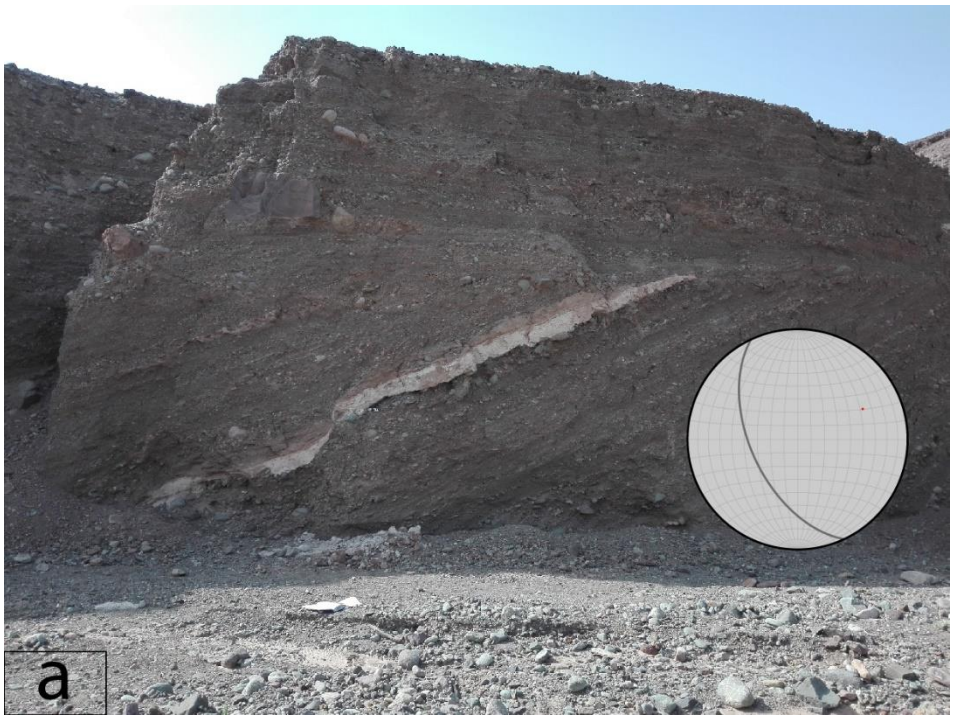

Fig. 3.20 fault displacing lacustrine sediment (a) field photo (b) interpretive sketch

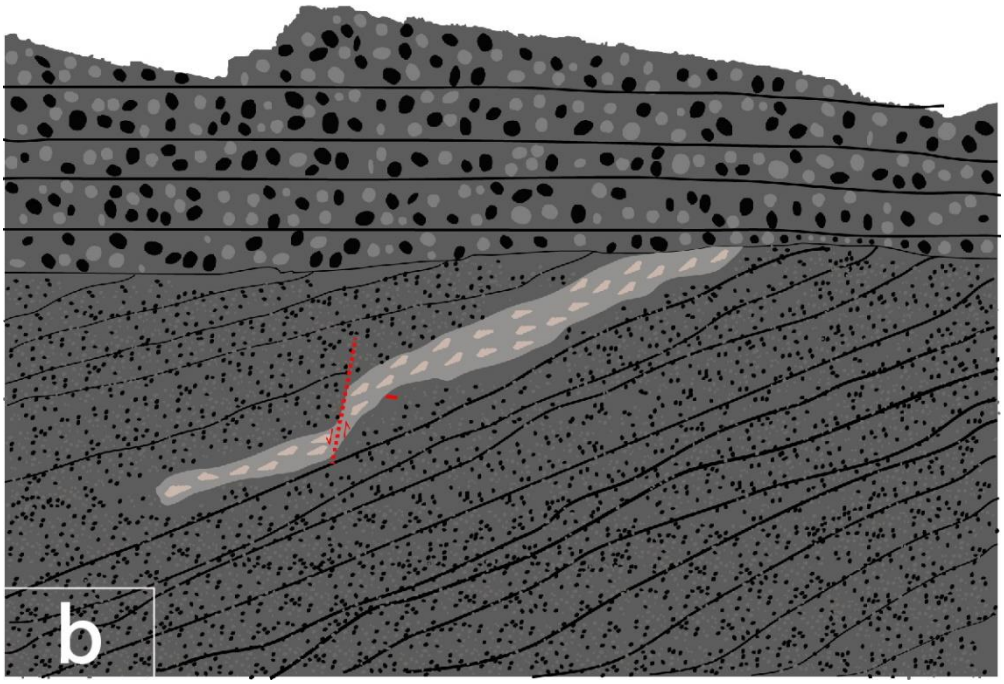

Fig. 3.20 (continued)

Standing on the western ridges within the study area steps of four old conglomerate terrace (see fig. 3.21) is clearly seen from the top. These steps represent faults which run generally E-W and along this, modern recent ephemeral streams flow through. Field observation revealed that there is a cliff-forming gypsum exposure adjacent to the alluvial sediments. The exposure extends 6km from the north to the south. This is interpreted to be fault and it is also easily spotted in the satellite image. These three sets of faults were recognized by their pronounced effect on the topography. Here sharp decrease in the slope from the gypsum and associated sandstone scarp to the recent alluvial from West to East is observed from the DEM as well.

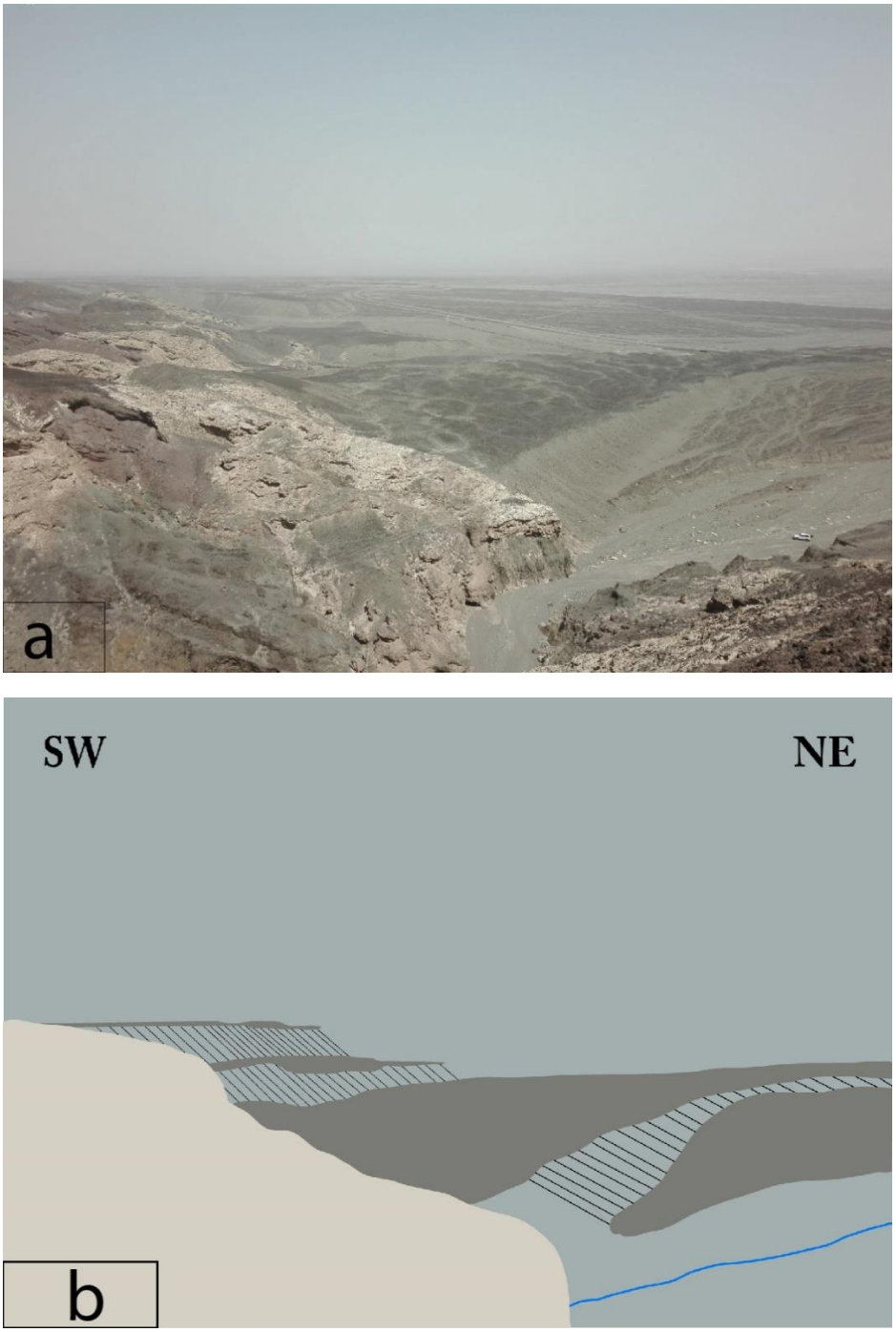

Fig. 3.21 Fault steps by old conglomerates terraces at different elevation. Note the blue line represent modern stream

Table 3.1 field measurements of fault attitude

No.	Strike	Dip	Rake (if any)	Remark
1	347	67NE	--	tilted bed of lithified conglomerate 30/25SE; phyllitic foliation 30/15SE; 273/35SW; juxtapose conglomerate and phyllite; small fault difficult to characterize and to follow above the surface
	345	70NE	--	
	344	70NE	--	
	70	72NNW	70 SW	
	307	65NE	40 NW	
2	190	70E	--	fault with drag zone
	185	75E	70 SSW	
	200	75SE	--	
3	354	73E	--	juxtapose conglomerate and lacustrine sediment; with hardened surface along which fluid moved
	5	70E	--	
	165	60NE	--	
	N-S	70E	--	
	170	70NE	--	
	350	75NE	--	
	340	85NE	--	
	330	75NE	--	
4	30	75SE	--	small fault within lacustrine sediment
5	N-S	85W	--	conjugate fault set
	N-S	90E	--	
	N-S	85E	--	
	N10E	75E	--	
	155	65E	--	
	150	70SW	--	
	160	75SW	--	
	145	87SW	--	
	N35E	65E	--	
	N15E	65E	--	
6	335	55SW	--	fault within inclined conglomerate unit above an angular unconformity
7	N-S	80E	--	

	15	100	--	affecting lacustrine sediment of thickness 20 cm
	015	80E	--	
8	325	20NE	--	affecting lacustrine sediment
9	320	90	--	Displace basalt lava

3.2.2.2 Other structures

The other structures observed and measured in the field include joints & cracks, unconformity, and foliations. The joint and crack are mainly seen on the basaltic lava and the gypsum unit: the joints on the basalt unit (see fig. 3. 22a) and the cracks on the gypsum unit (see fig. 3.22b & c). The joints and the cracks have a general trend of NNW (see table 3.2) where some of them deviate to the N-S. As can be observed in fig. 3.22a the joints are parallel to sub-parallel to one another maintaining roughly the same average spacing that these are systematic joints. This basaltic lava flow has been broken into joint-bound columns. The trace lengths of joints are measured in (tens) of meters. These, roughly, regularly spaced joints have an average distance of 30-50 cm between each other. The Gypsum cracks usually are 30-40 cm wide on average. Some of these cracks are filled with unsorted, angular, mud supported grains or blocks (see fig. 3.22 c).

Fig. 3.22 Joints and cracks (a) columnar joint in basalt lava (b) nearly vertical gypsum crack (c) gypsum crack filled with unsorted, angular, mud supported grains or blocks

Fig. 3.22 (continued)

Table 3.2 field measurements of joints affecting basaltic lava and gypsum cracks

No	**1**	**2**	**3**	**4**	**5**	**6**
Joints affecting basaltic lava						
Strike	N-S	150	325	125	350	10
Dip	85E	85NE	80SW	90SW	85NE	85NE
Gypsum Cracks						
No.	**1**	**2**	**3**	**4**	**5**	**6**
Strike	140	140	90	110	305	325
Dip	65 SW	65 SW	60 SE	47 SW	67 SW	80 SW
No.	**7**	**8**	**9**	**10**	**11**	**12**
Strike	310	305	315	350	160	330
Dip	85 SW	80 SW	87 SW	80 SW	70 SW	85 SW
No.	**13**	**14**	**15**	**16**	**17**	**18**
Strike	185	155	165	340	178	340
Dip	79 SW	90 SW	90 SW	85 SW	85 SW	85 SW
No.	**19**	**20**	**21**	**22**	**23**	**24**
Strike	160	318	300	130	160	330
Dip	87 SW	80 SW	84 SW	75 SW	85 SW	85 SW
No.	**25**	**26**	**27**	**28**	**29**	**30**
Strike	135	300	140	315	145	325
Dip	72 SW	80 SW	90 SW	85 SW	85 SW	80 SW
No.	**31**	**32**	**33**	**34**	**35**	**36**
Strike	335	330	350	170	340	325
Dip	80 SW	90 SW	90 SW	80 SW	75 SW	85 SW
No.	**37**	**38**	**39**	**40**	**41**	------
Strike	145	180	320	320	155	------
Dip	75 SW	75 SW	78 SW	80 SW	90 SW	------

Angular unconformity between an overlying horizontally stratified conglomerate and inclined conglomerate (see fig. 3.22) below indicate that tilting during the time of non-deposition gave rise to the inclination of the conglomerate unit below the surface of unconformity relative to the conglomerate above. The sloping conglomerate below has a dip of 30^0 to the NE. The unconformity is confined to only this outcrop. In the field, tectonic (or secondary) foliations

were also measured. The measured foliations are slatey cleavages (see fig. 3.8) and have a general NNW trend (see table 3.3 below).

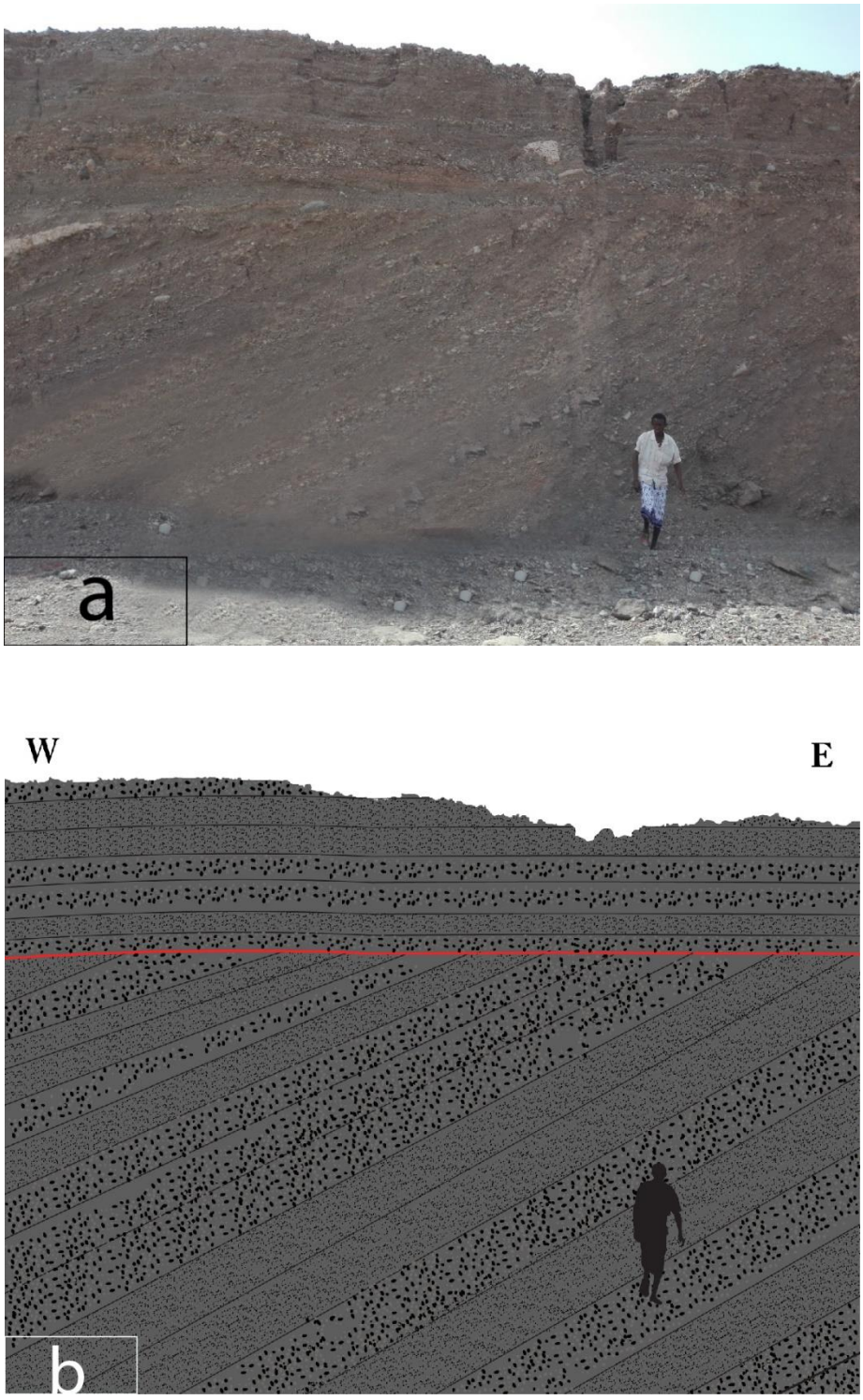

Fig. 3.22 angular unconformity (a) field photo (b) interpretive sketch

Table 3.3 orientation data of measured slatey cleavages

No	**1**	**2**	**3**	**4**	**5**	**6**	**7**	**8**	**9**	**10**
Strike	30	120	110	115	140	135	155	155	150	110
dip	15SE	70SW	90SW	75SW	85SW	85SW	65SW	70SW	70SW	80SW
No.	**11**	**12**	**13**	**14**	**15**	**16**	**17**	**18**	**19**	**20**
Strike	140	110	135	120	150	105	130	135	120	150
Dip	90SW	80SW	85SW	85SW	80SW	80SW	85SW	80SW	55SW	85SW

CHAPTER 4

STRUCTURAL, REMOTE SENSING AND SEISMIC DATA ANALYSIS

4.1 Structural Analysis

All structural orientation data collected from the field and extracted from DEM was analysed using the stereographic projection technique. StereWin software package Version 8 (Allemendiger, 2012) allowed to analyse the trend of the structures. Here the strike of faults, joints and cracks and foliation is analysed (see fig.4.1).

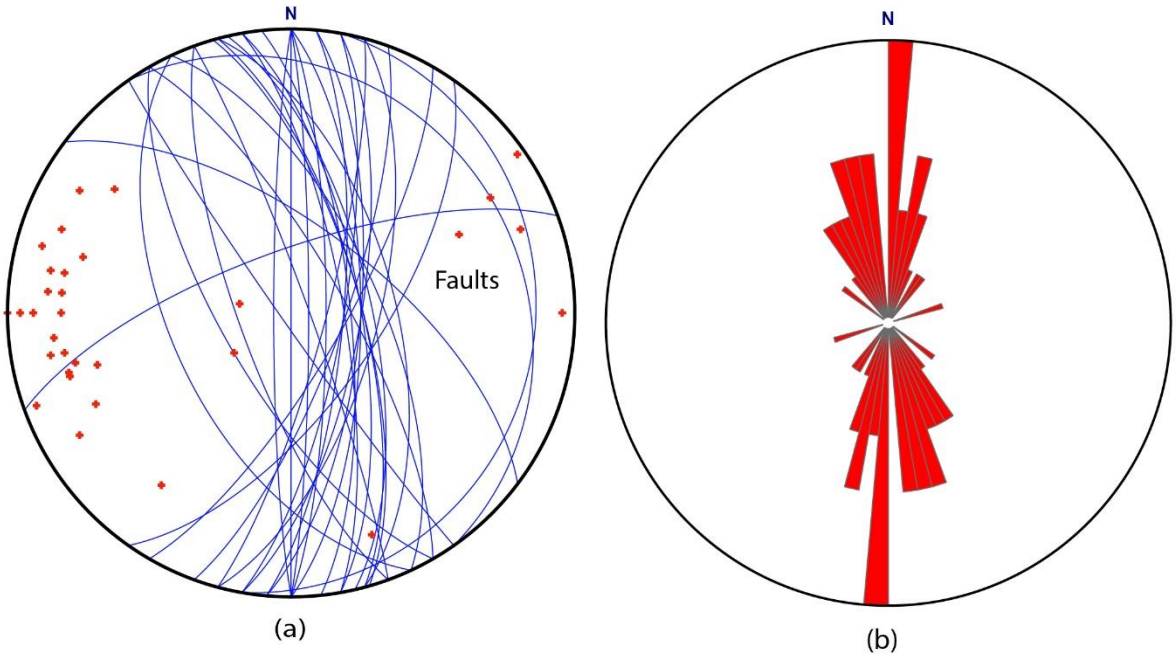

Fig. 4.1 Schmidt net lower hemisphere plot of structures measured in the field (a) stereoplot of faults (b) (b) rose diagram of faults (c) stereoplot of joints and cracks (d) rose diagram of joints and cracks (e) stereoplot of foliations (f) rose diagram of foliations (g) rose diagram of structures extracted from DEM

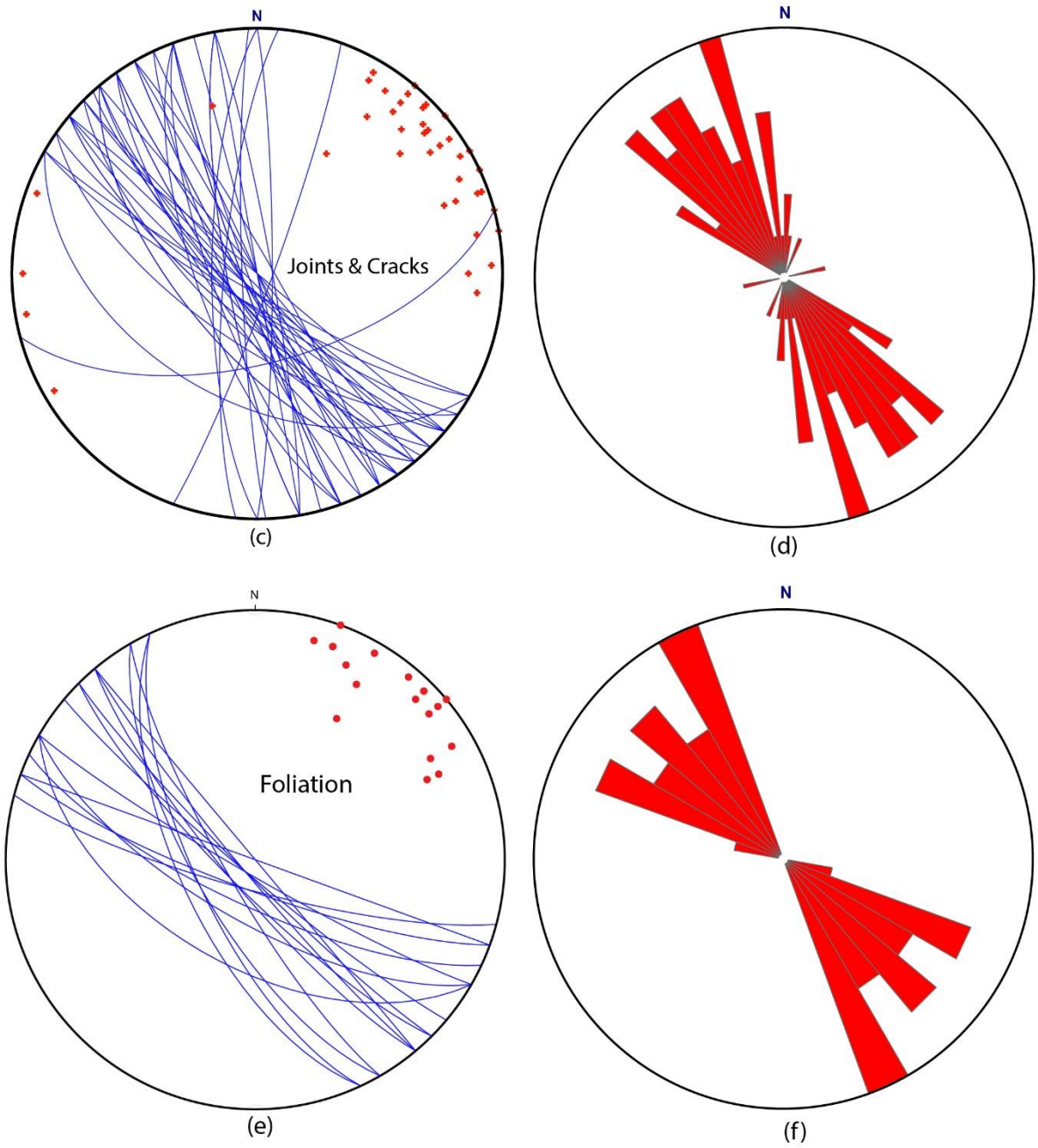

Fig. 4.1 (continued)

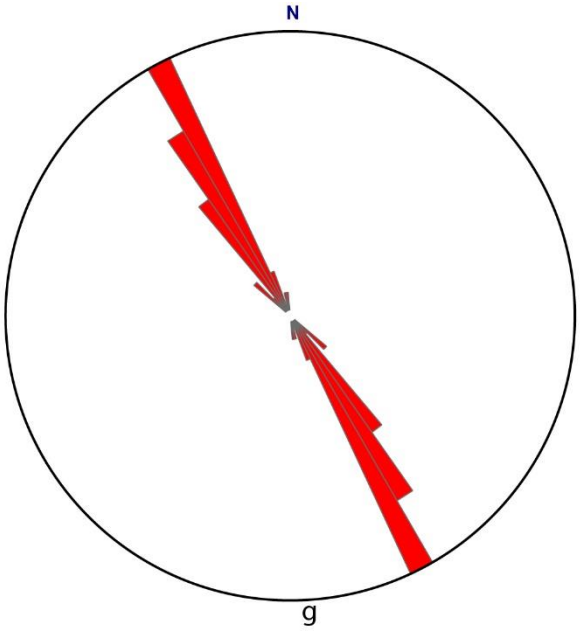

Fig. 4.1 (continued)

4.1.1 Kinematic Analysis

Fault-slip data provide direct information on kinematics since slickenlines are direct indicators of displacement directions on fault planes. Thus fault-slip data collected from the field was used to analyse kinematics in the study area using the FaultKin program (Allmendinger et al., 2001). The principal kinematic indicator here is fault striation (see fig. 4.3 below) on slickensides. Many of the faults have been observed without development of striae. This may have to do something with the lithology or the effect of weathering and erosion. That is, may be the host rock was not able to take a polish or the original polished surface was destroyed by weathering and erosion since many of the faults affect either conglomerate or lacustrine sediments.

The measured strike and dip of fault planes and rake of the striations were plotted on the Schmidt net stereonet (see fig. 4.4 below) for the analysis. Fault-slip data from two fault sets (see Table 4.1) allowed to quantitatively characterize the overall local deformation or movement pattern resulting from cumulative fault motions in a region and to determine the direction of bulk shortening or extension (i.e., strain see fig 4.2 below) using the methods of Marriet & Allemendiger et al. (1990).

The anisotropy on the fault slickensides left the surface to feel smoother as you slide your hand in the shear direction as opposed to sliding your hand in the direction opposed to the shear direction especially on the first two fault planes.

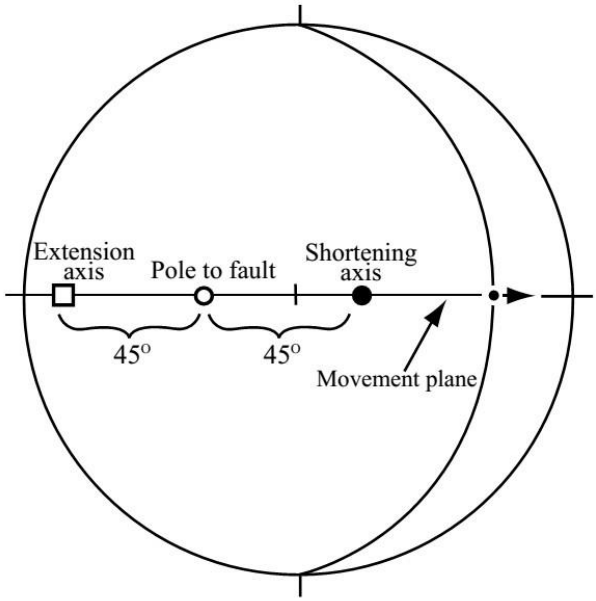

Fig. 4.2. Geometry of fault-slip kinematics in lower-hemisphere, equal-area stereographic projection. The kinematic axes, slip direction and pole to fault lie in a common plane called movement plane, with each of the kinematic axes forming angles of 45^0 with both the slip direction and the pole to fault (Marriet & Allemendiger et al., 1990)

Table 4.1 Fault-slip data

Fault Plane	Strike	Dip	Rake
1	307^0	65^0NE	40^0NW
2	185^0	75^0E	70^0SE

Fig. 4.3 Striations on slickenside of faults observed in the field

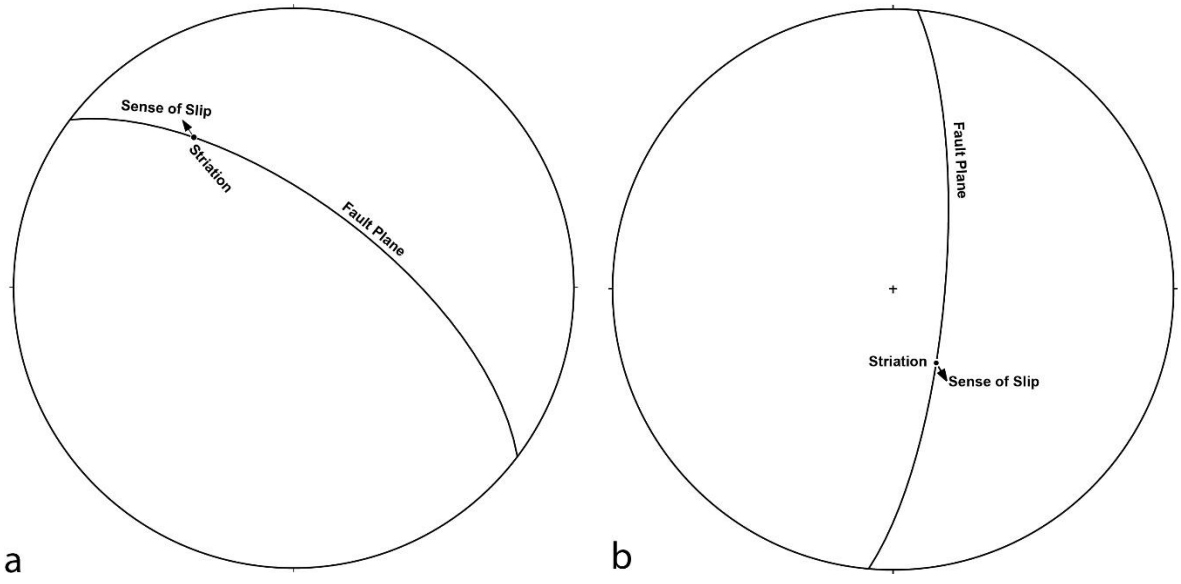

Fig 4.4 fault-slip data lower hemisphere Schmidt net plot

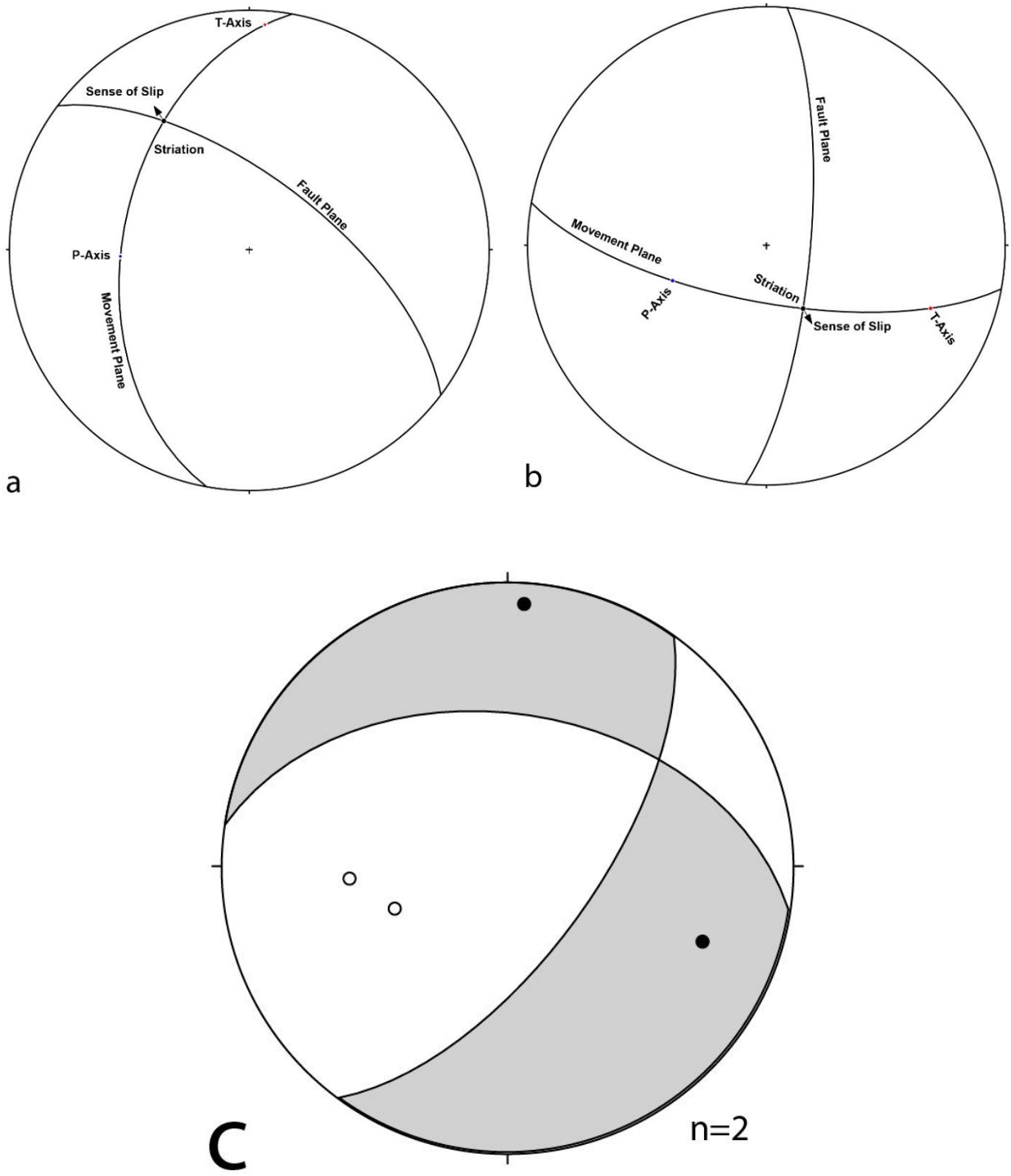

Fig. 4.5 Kinematic analysis of fault-slip data (a) fault 1 (b) fault 2 (c) The results of kinematic analysis fault-slip data (n=total data) applying the method of Marrett and Allmendinger (1990). Note the filled dots represent the extension axes and the hollow dots represent the shortening axes.

4.1.2 Dynamic Analysis

In this sub section, structural data collected from conjugate normal fault set is analysed seeking to reconstruct orientation of local stress field (σ_1, σ_2, σ_3) that produced these oppositely dipping normal faults. As demonstrated by Anderson (1951) the relationship between the three fundamental stress regimes at the earth's surface and their associated faults define the basic categories of normal, reverse and strike-slip faulting. For each stress regime, there are two possible fault plane orientations, forming a conjugate pair whose acute bisector gives the direction of maximum compressive stress and whose obtuse bisector gives the direction of minimum compressive stress (Anderson, 1951; see fig. 4.6 below).

Orientation data for set of conjugate faults measured in the field was plotted where for corresponding attitude data presented on the table below (see table 4.2 below).

Table 4.2 Structural data for conjugate fault set

Fault plane	Strike	Dip
1	010	75E
2	160	75W

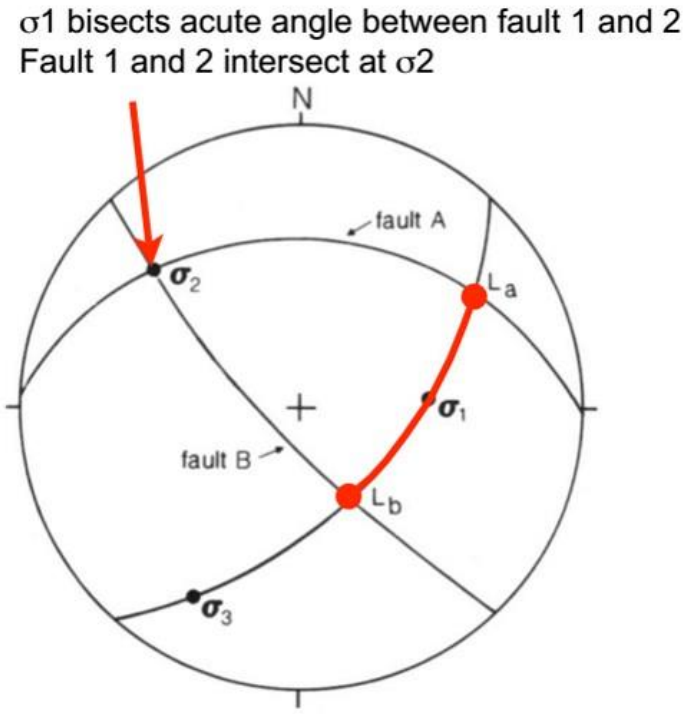

Fig. 4.6 Determining the orientation of the principal stress axes σ_1, σ_2 and σ_3 from a conjugate fault pair (Anderson, 1951)

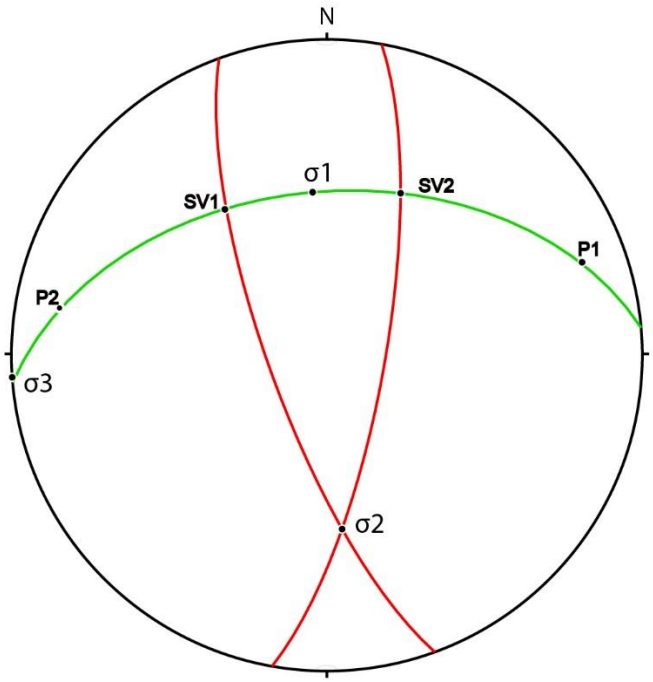

Fig. 4.7 Dynamic analysis of conjugate fault to determine the orientation of principal stresses. The red great circles represent the fault planes and the green great circle shows the movement plane

4.1.3 Rate of Deformation

Rate of deformation was calculated from coral reef elevation measurements and age determination to quantify vertical movement in the western margin of the Danakil Depression. The elevation measurement was taken using differential GPS (dGPS) during the fieldwork in 2016. The age determination employed U-Th dating method. The elevation measurements of two marine sequence which were differentiated in previous studies (Foubert et al., 2015; Jaramillo-Vogel et al., 2015) were taken on various outcrops using dGPS as can be seen in table 4.3 and fig. 4.8. The relative sea level curve of Rohling et al. (2009) was used where the sea level for each MIS (Marine Isotopic Age) have been set at -10 m for MIS 7 and +5 m for MIS 5e. General uplift and subsidence rate has been calculated for the period between the first coral generation and today (200 – 0 ky). Elevation measurements of CO1, CO3/11, CO4, CO6, CO7, CO12, CO14, CO16, CO18 and CO19 (see table 5.1) were used in the subsidence/uplift rate calculation using the equation R= (D/200 ky) *100; where R is rate, D is total displacement of coral reef sequence and 200ky is the age of the oldest sequence. In this vertical movement

quantification, the sea level was set at -10m for MIS7 coral reef sequence according to Rohling et al. (2009)

Table. 4. 3 Average elevation for each visited outcrop. For CO14 and CO19 the altitudes are extracted from DEM.

Outcrops	Relative distance S-N (km)	Altitude of MIS7 (m)	Altitude of MIS5(m)
3	0	-8.8	-
11	0	-	-32
11	18	8.3	6.7
12	18.5	8.6	8.2
2	18.7	-	10.9
7	19	9.8	10.1
14	20	18	20
4	23.8	20.5	38.8
6	36.5	46.8	103.2
18	53	-32.8	-
16	65	64.3	170.1
19	66.5	130	110
17	68.5	-	93.7

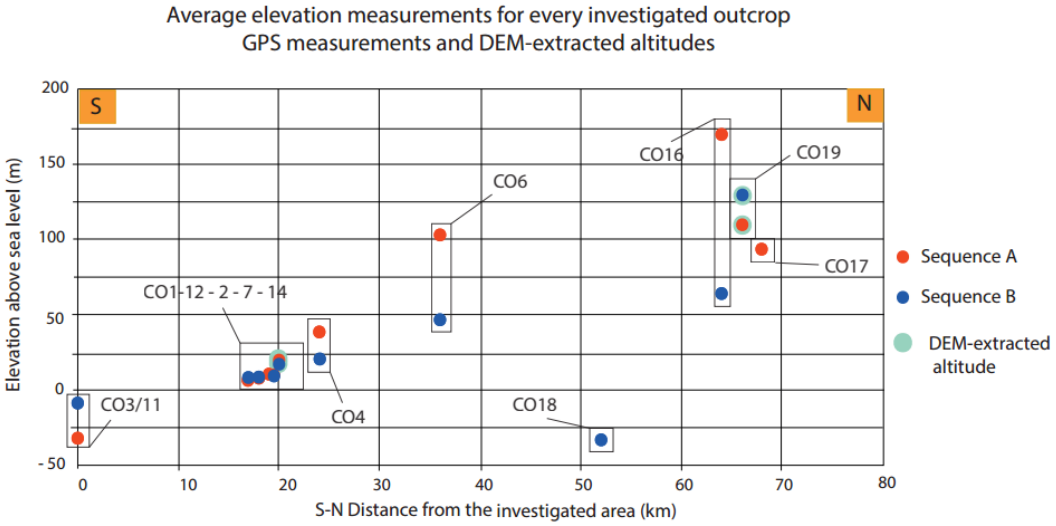

Figure 4.8 Graph illustrating the average measured altitudes along the north-western margin of the Danakil depression. From the southern part (km 0) to the northernmost visited area (km 68.5)

4.2 Remote Sensing Data Analysis

Landsat images of the study area, along with available regional map and field observation, were analysed by digital image processing techniques to delineate various geological and structural features of the area. Two major techniques in digital image processing, according to Ali et al. (2012), were employed. They are pre-processing and enhancement. ENVI 4.7 and ERDAS IMAGINE 2014 software packages were used in digital image processing to enhance the quality of the satellite raw digital data and produce image suitable for visual geological interpretation.

4.2.1 Pre-processing

Remote sensing data employed in this research are Landsat 8 and SRTM DEM. These data were processed and analysed using the software packages Environment for Visualizing Images (ENVI) version 4.7, and global mapper software version 11.These remote sensing data were pre-processed where layer stacking was performed before proceeding to the main processing techniques: band combination and band ratioing. The pre-processing makes satellite image interpretable for a specific use.

Landsat 8 image has 11 bands which are of 30 m resolution except band 8, which is of 15 m resolution. Here bands 1-7 were stacked since single bands are hardly of any use for remote sensing and GIS work (see fig. 4.9 below for comparison). Only bands 1 to 7 were stacked (see fig. 4.9 below) because the other bands are not useful for distinguishing lithologies and delineating structures.

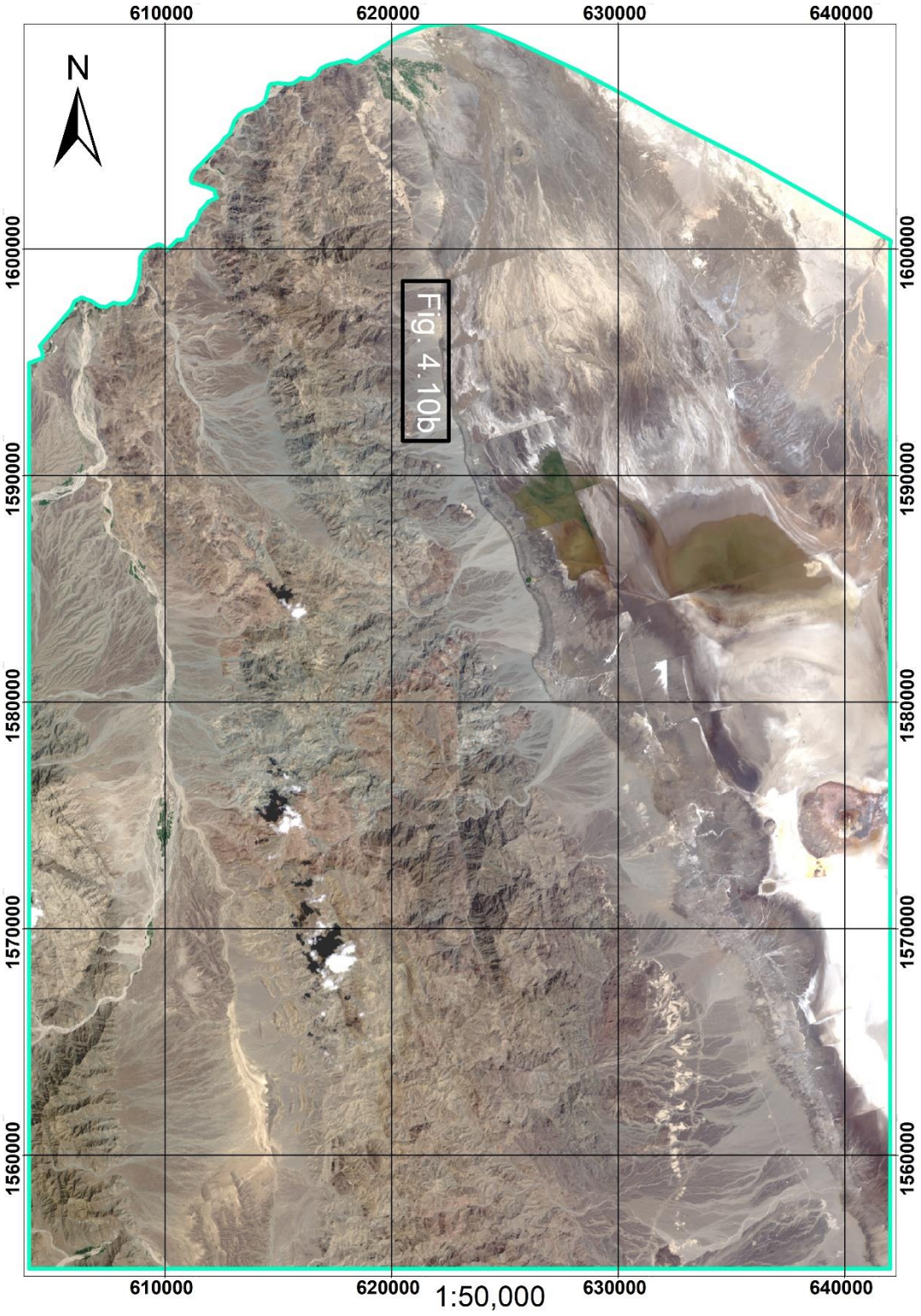

Fig. 4.9 Natural colour (4-3-2) Landsat 8 image of study area. Note here bands 1-7 are stacked (b) Landsat 8 single band image which has low lithologic discrimination capability as compared to the layer stacked image

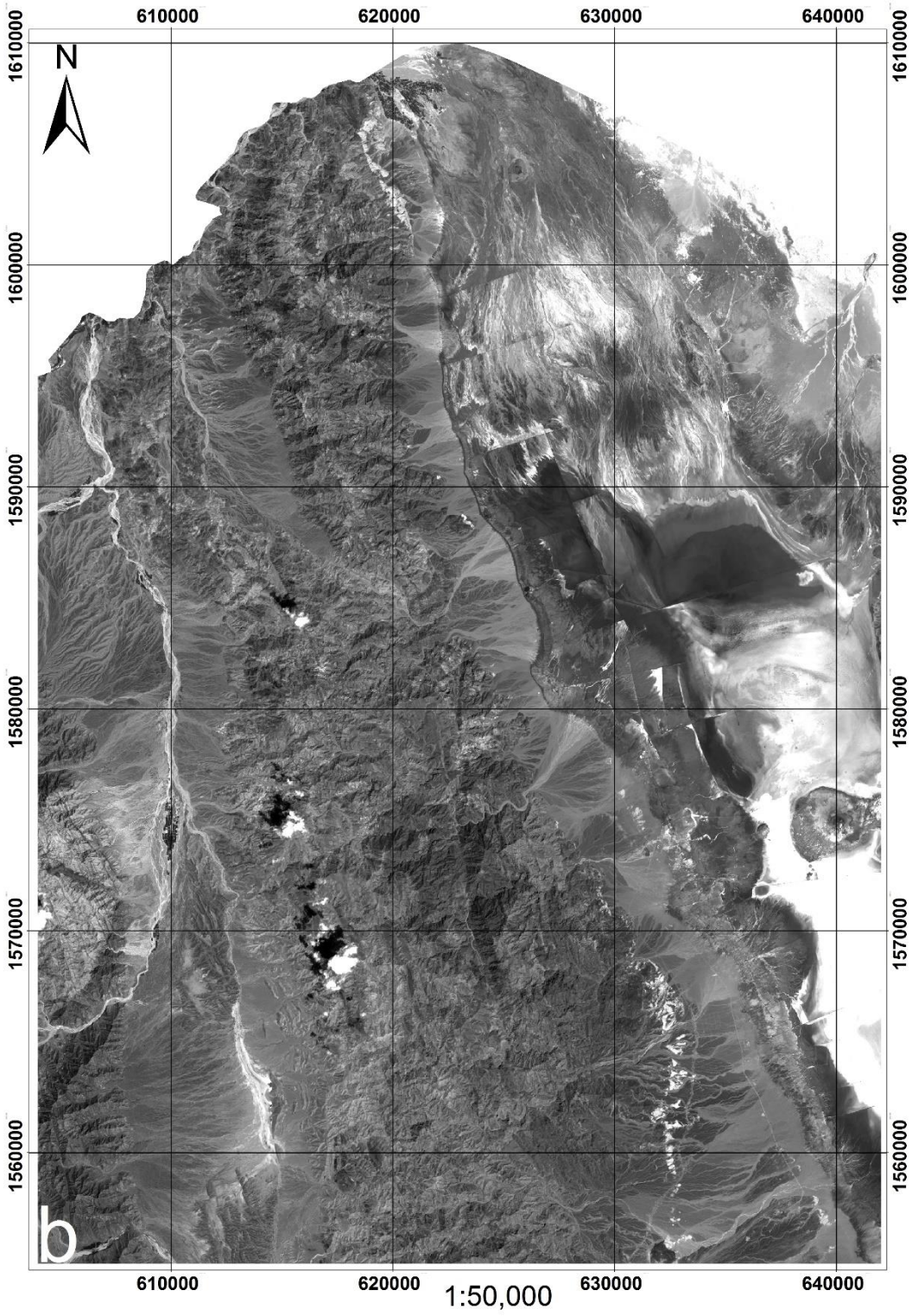

Fig. 4.9 (continued)

4.2.2 Enhancement

Image enhancement techniques were used with an objective to improve the visual appearance or interpretability of satellite images so that the images appear in a form better suited for analysis and extraction of more (geological) information. These techniques modify attributes of an image to make it more suitable for a given task and a specific observer; for geological interpretation in this case, by maximizing clarity, sharpness and details of features of interest. The enhancement techniques applied here are RGB combination and band ratioing. Different authors (for e.g., Sultan et al., 1987; Ali et al., 2012; Gad & Kusky, 2006; Mwaniki et al., 2015) have shown that band combinations and ratioing maximize rock discrimination and structural delineation.

4.2.2.1 RGB (Band Combination) Combination

Landsat images are acquired in grayscale and the human eye is more sensitive to color than greyscale brightness variations, therefore for better display of scenes band combination is important. Band combination is an effective means for visual interpretation of multispectral imagery where bands of data from more than one sensor are merged to produce a single image that displays useful properties from each of the sensors (Lillesand and Kiefer, 1994; Gupta, 2003). Band combination allows to see different features within a scene to execute different types of analysis. Here the rule for band combination: rendering the most informative band for a particular purpose in red, the next in green and the least informative in blue (Drury, 1993) is applied. Since band 1 is designed for studies of coastal water and aerosols, it cannot be used to detect geological features (for e. g., Pour & Hashim, 2015) therefore it is excluded in band combination operations.

Landsat 8 bands 6 and 7 cover different slices of the shortwave infrared, or SWIR. They are particularly useful for geology: rocks and soils that look similar in other bands often have strong contrasts in SWIR (https://landsat.gsfc.nasa.gov/landsat-8/landsat-8-bands/). The SWIR bands are sensitive to changes in the soil and rocks content which subsequently make it possible to differentiate some basic rock types (Amusuk et al., 2016). Hence these bands are applied in many of the band combination operations here.

Several band combinations proposed by different researchers (Qaid and Basavarajappa, 2008; Gül et al., 2012; Saadi & Watanabe, 2008; Mwaniki et al., 2015; Peña and Abdelsalam, 2006; Pour and Hashim, 2015; Ali et al., 2016) and experimented within this study were operated to check their applicability to differentiate rock types within the present study area. Those false colors composites which discriminated lithologies within the study area were applied to map geological features. The RGB color combination images were created based on laboratory spectra of minerals related with lithological units in the study area. The RGB color composite operations performed are 4-3-2, 7-4-2, and 7-6-5. These combinations were selected based on previous success in geological and structural mapping and visual inspection by comparing each of the stretched Landsat 8 band images, first as grey level images, and then as color composites of three bands. The capability of the color composites was assessed by the ability of individual bands to distinguish between different lithologies shown on the regional geologic maps (1:250,000 and 1: 500,000).

Alluvial sediments and old conglomerates were easily mapped employing the natural color band combination (4-3-2) and they appear distinct also in almost all the other false color composite operations tested. The operations were also supported by field observation. In the natural color band combination, recent alluvial sediments appear light grey and are easily identified by their pattern and form: fan shaped form. Old conglomerates look dark grey in 4 3-2 Landsat 8 image (see fig. 4.10b below).

The color composite images of bands 7-4-2, which has proved to have a higher efficacy in geological application (e.g., Ali et al., 2016; Kamel et al., 2016; Saadi & Watanabe, 2008; Peña and Abdelsalam, 2006; Ali et al., 2012; Moufaddal and Rifaat, 2006), enabled to discriminate salt formation and gypsum which otherwise appear similar in other band combinations, for instance they both appear white in 4-3-2 image. In this image salt formation appear markedly green and gypsum appear white (see fig. 4.10a & f below).

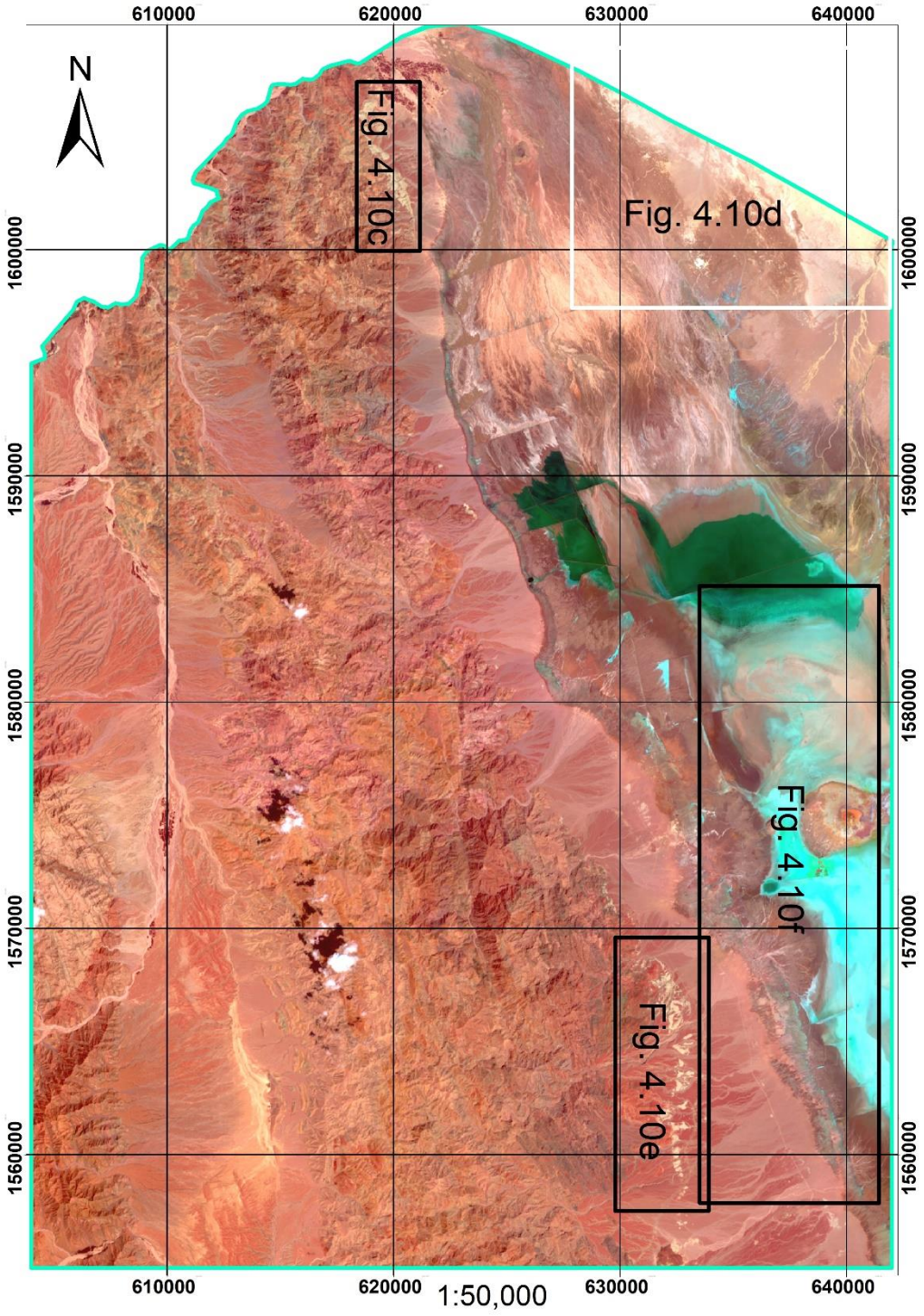

Fig. 4.10 Landsat 8 7-4-2 image (a) and larger scale view of various lithologies mapped (b) alluvial sediments and old conglomerates in 4-3-2 (c), (d) & (e) gypsum in different parts of the study area (f) salt formation and salt mixed with mud.

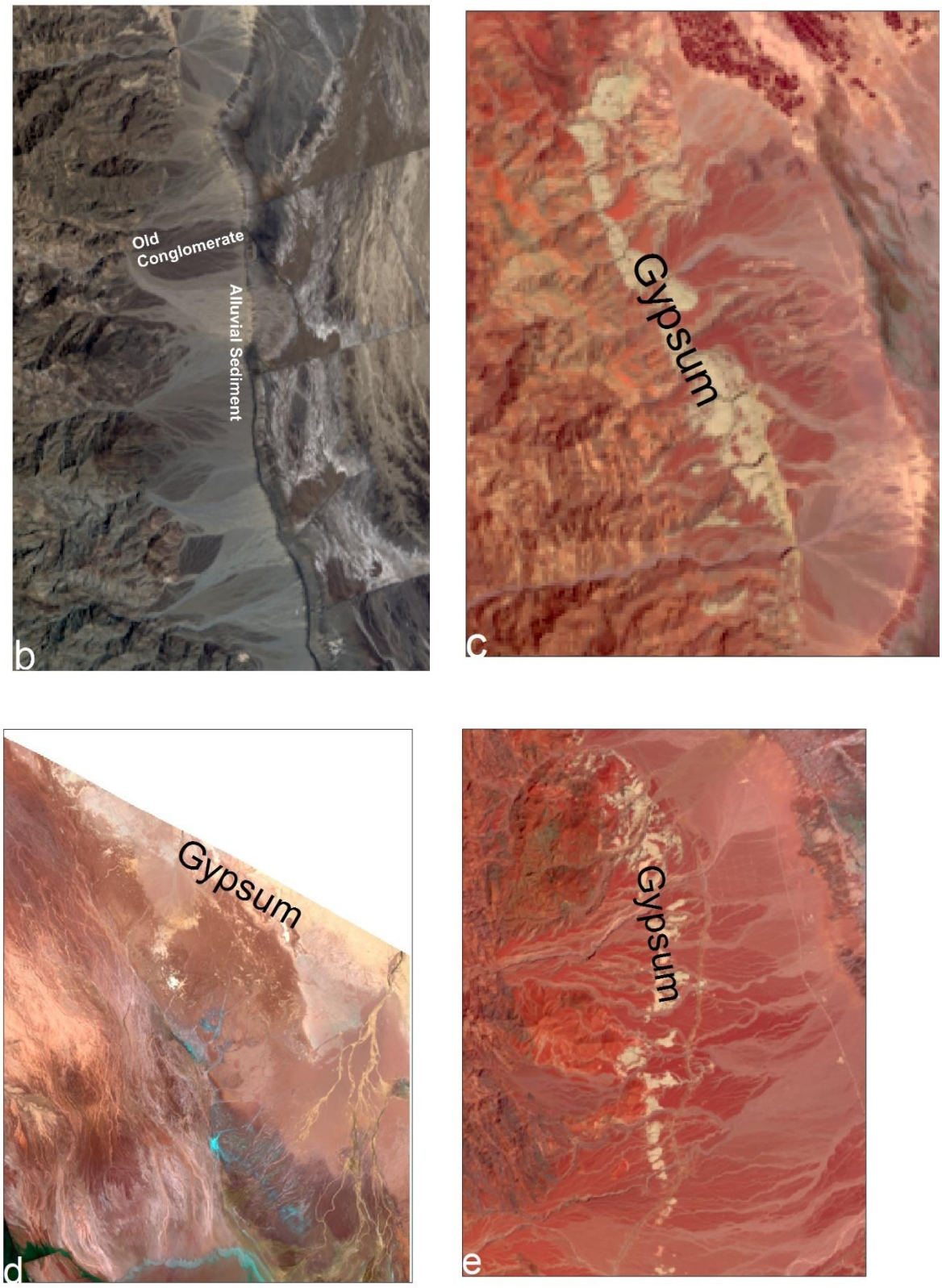

Fig. 4.10 (continued)

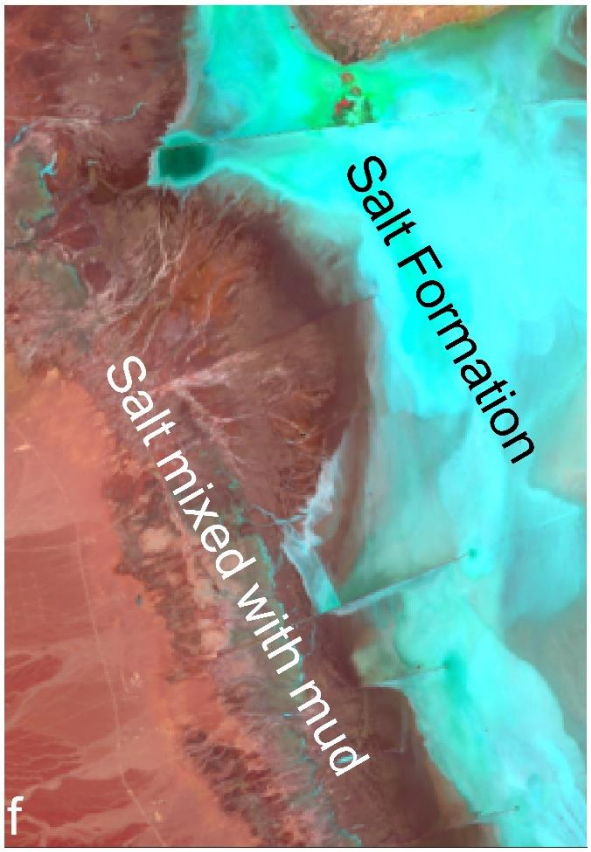

Fig. 4.10 (continued)

Phyllite look clearly light greenish grey in the natural band combination. But somehow it appears similar to the alluvial sediment. To clearly discern phyllite from alluvial sediments the False Color Composite (FCC) 7-6-5 is operated (see fig 4.11). In the 7-6-5 combination phyllite appears distinctly light yellowish green.

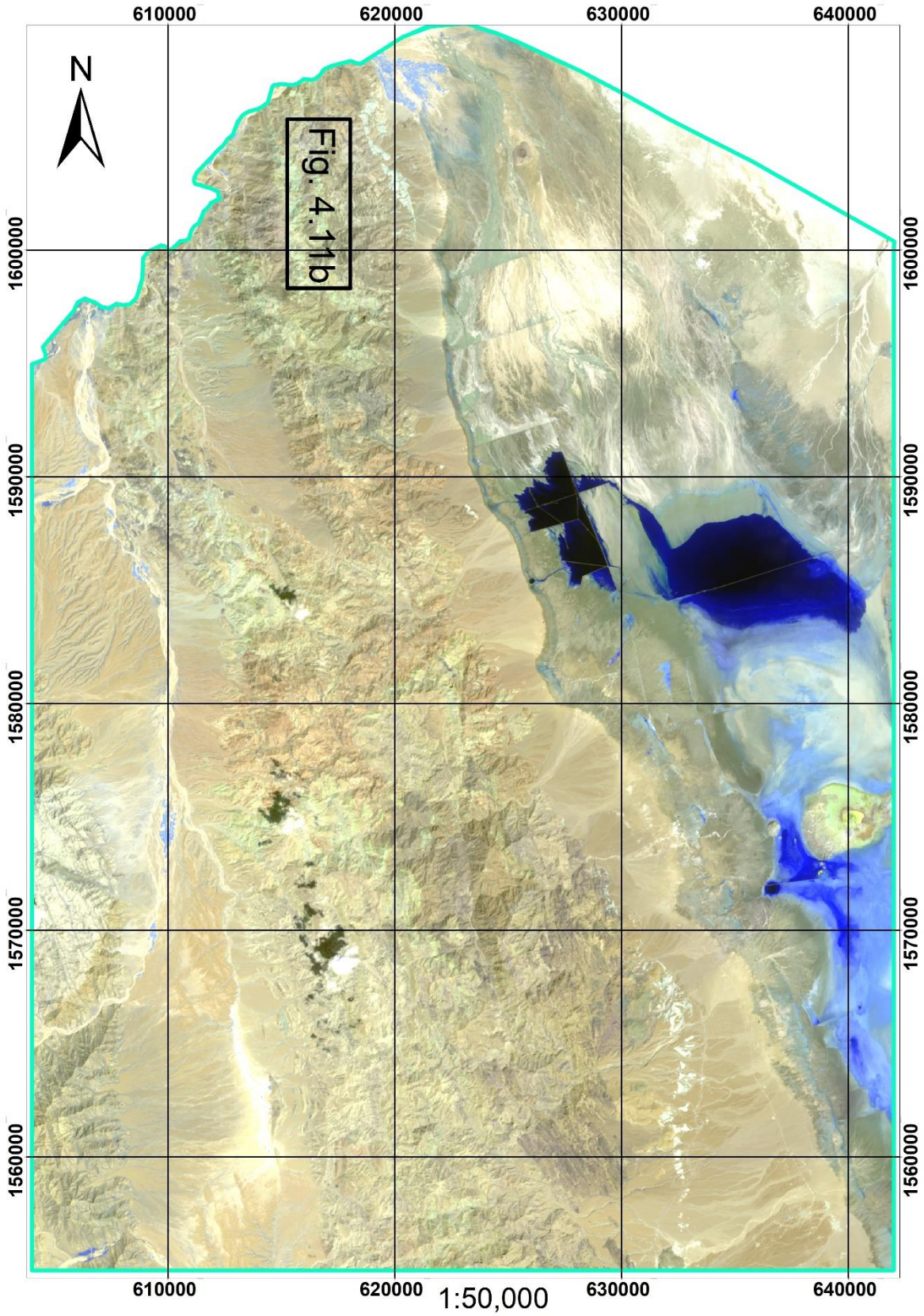

Fig. 4.11 false colour composite of bands 7-6-5 (b) Phyllite appear light yellowish green

Fig. 4.11 (continued)

4.2.2.2 Band Ratioing

Band ratioing is image enhancement technique where the Digital Number (DN) value in one band or more is divided by the corresponding DN value in another band or more for each pixel where the resulting DN values represent the ratio image. Band ratios are useful for highlighting certain features or materials that cannot be seen in raw bands. They are effective in reducing effects of illumination directed from the sun, slope and shadows to the marked degree (Sabins, 1987; Gupta, 2003; Lillesand and Kiefer, 1994).

Band ratio images are effective in enhancing the spectral response of different minerals and rocks and their efficacy have been shown in several studies (Ali et al. 2012; Mshiu, 2011; Sabins 1999; Sultan et al. 1987; Amusuk et al., 2016; Ali and Pour, 2014; Pour and Hashim,

2014; Kamel et al., 2016; Adiri et al., 2016; Amusuk et al., 2016; Gad & Kusky, 2006; Garba and Bhaskar, 2015; Simon et al., 2016). Various ratios were created and those ratios that contain greater geological information were used in this analysis by setting them in RGB. RGB band ratio images used in the current study and proved to be very effective in the lithological discrimination are 4/2, 6/7, 6/5 and 5/7, 3/5, 3/2 (Figs. 4.12, and 4.13). These ratio images enabled to discriminate between sandstone and limestone in the central part of the study area. These lithologies appear similar in many of the band combination operations tested. They both appear brown, for example, in the 7-4-2 band combination. Hence, it is difficult to distinguish sandstone and limestone. However, in the RGB band ratio image after many trials 4/2, 6/7, 6/5 (Fig. 4.12), sandstone appears light greenish grey in colour while limestone has deep purple colour. This made it easy to discriminate sandstone which appears similar to other lithologies, for example, phyllite in another band combination as in 7-4-2 and 4-3-2. Whereas in the band ratio image 5/7, 3/5, 3/2 (fig.4.13) sandstone appears in dark green colour while the associated limestone rock appears deep purple.

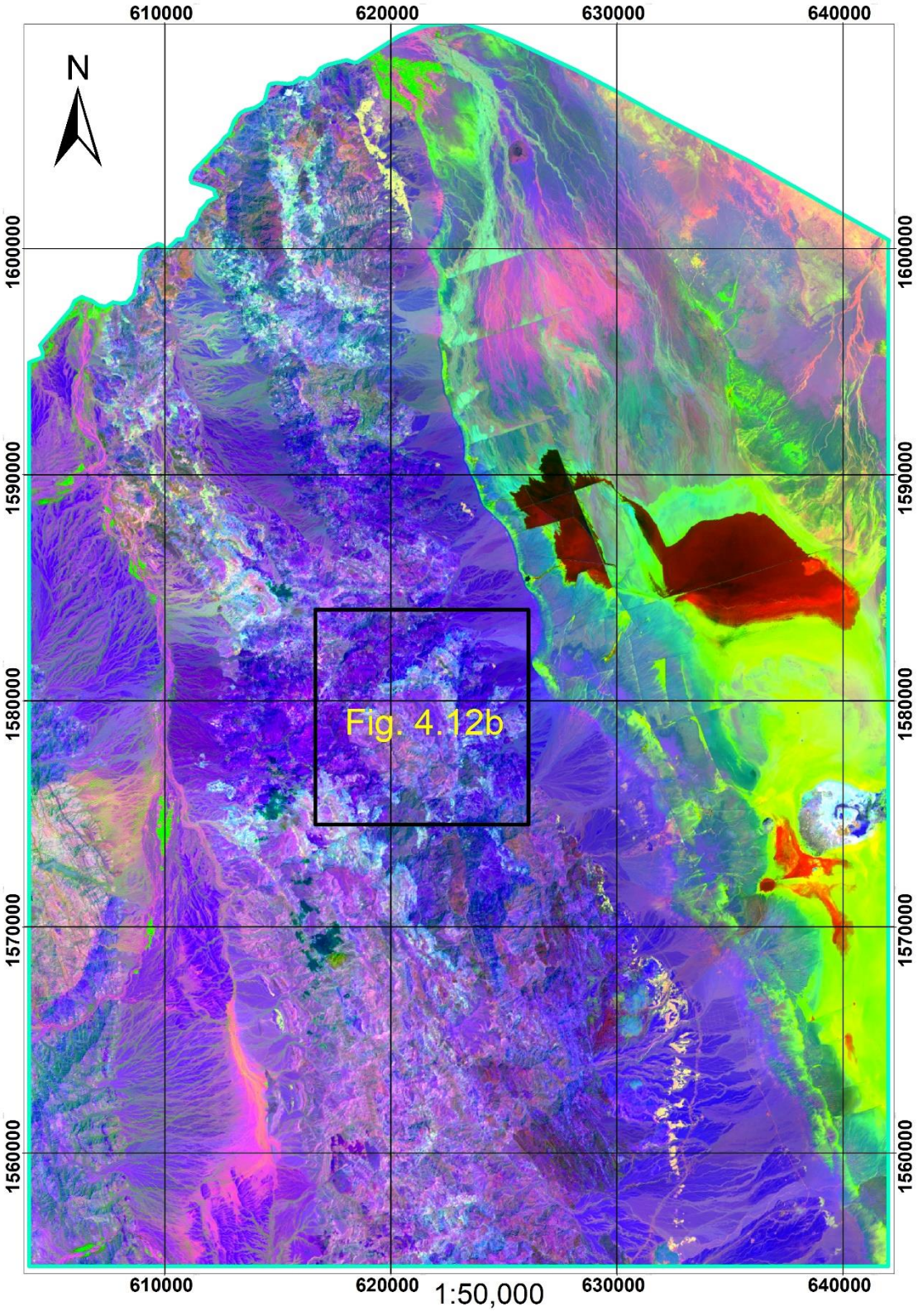

Fig. 4.12 Landsat 8 4/2, 6/7, 6/5 RGB band ratio image (a) (b)limestone appear light purple and sandstone appear light greenish grey

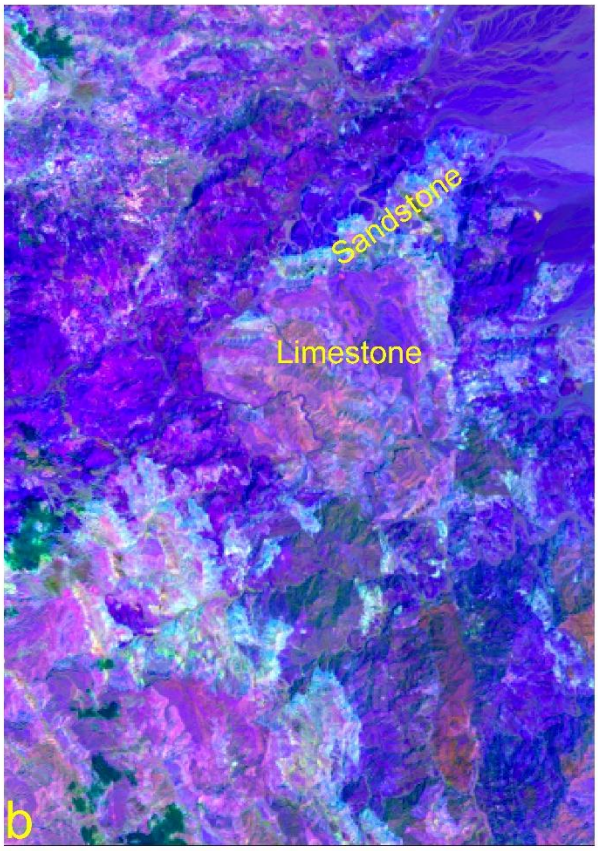

Fig. 4.12 (continued)

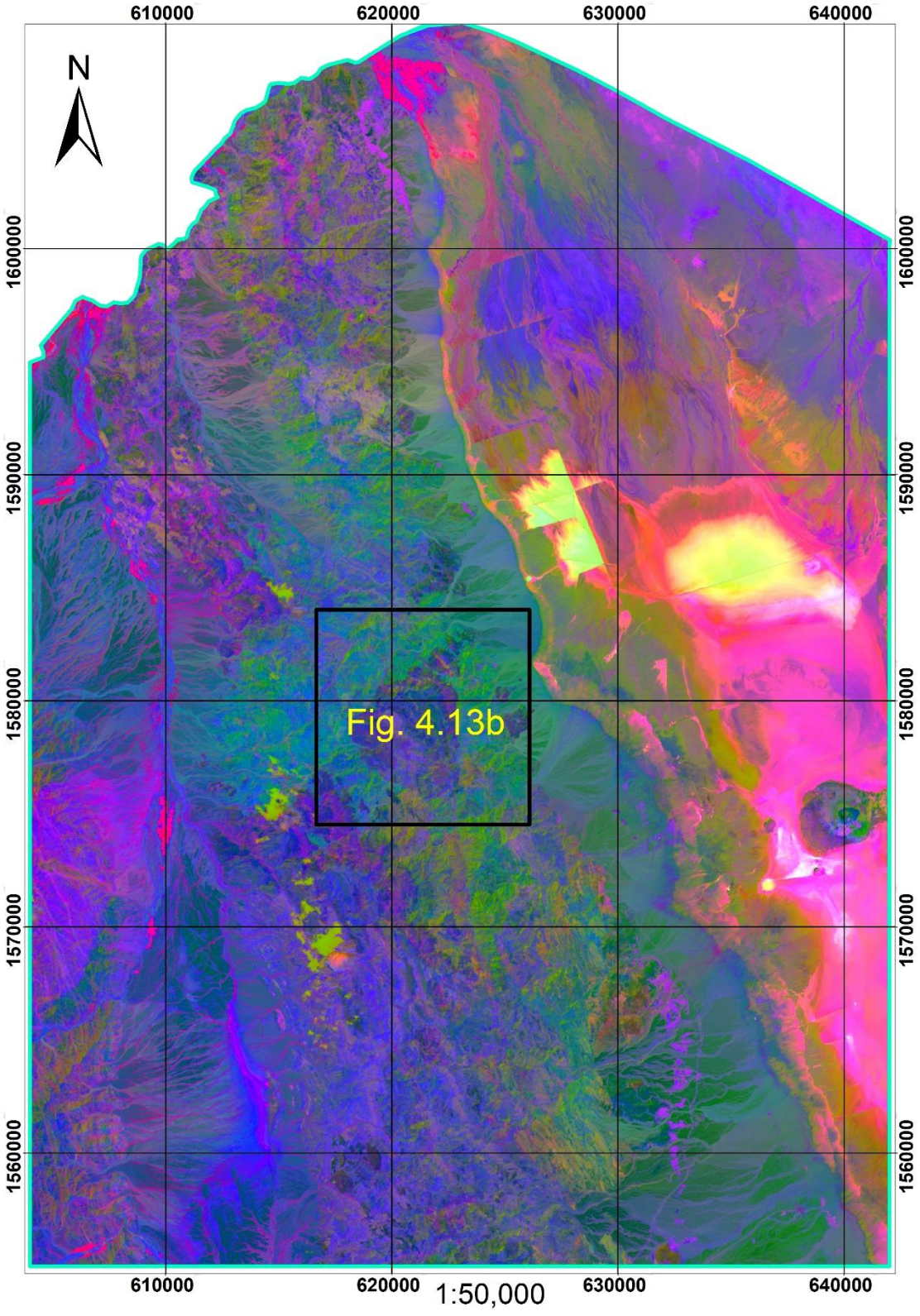

Fig. 4.13 Landsat 8 5/7, 3/5, 3/2 RGB band ratio image (a) (b)limestone appear deep purple and sandstone appear dark green

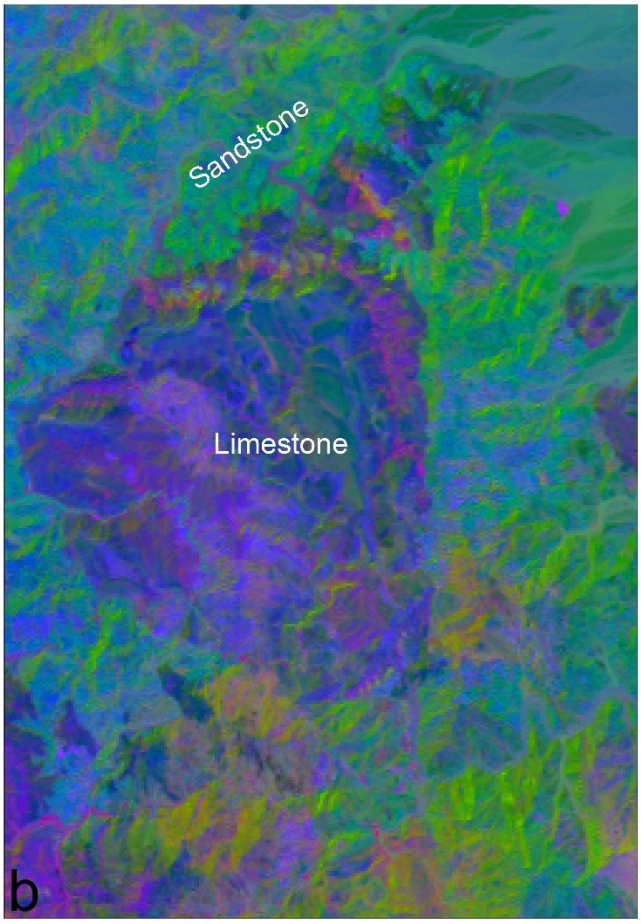

Fig. 4.13 (continues)

4.2.2.3 Manual Extraction of Structures from SRTM DEM

The faults mapped here from satellite imagery and SRTM DEM are identified based on break in slope, abrupt change in stream course, aligned ridges (see fig. 4.14), and incision of alluvial fans. The remote sensing data is supported by field observation and existing regional maps and literature. Cross sections from the DEM along different parts of the study (see fig. 4.15) area also allowed to determine the downthrow direction of faults mapped.

Fig. 4. 14 Ridges aligned parallel to the general trend of the study area (a) and fault scarp on the western margin of the Depression

Available Regional geological map at a scale of 1:500,000 (Barberi et al., 1973) and 1: 250,000 (Brinckmann et al., 1970) were overlain in a GIS in image form. The maps were overlain on natural (4-3-2) and various false colour composite of Landsat 8 imagery and hill-shaded SRTM

DEM. This served as a quick check on the reliability or otherwise of the existing maps, and the amount of information likely to be added by remote sensing interpretation. Identified faults were interactively digitized in the SRTM DEM and Landsat 8 image using Global Mapper software package version 11. Then the faults were put in a GIS in shapefile form. For manual extraction of structures hill shade was created with the default sun elevation and azimuth angle 45^0 and 315^0 respectively (see fig. 4.16). This hill shaded image eases the extraction of structures by enhancing the SRTM DEM raster image where structures were inferred from tonal shading variation. The structures were plotted into rose diagram (see fig. 4.1g) to define structural trend of the study area.

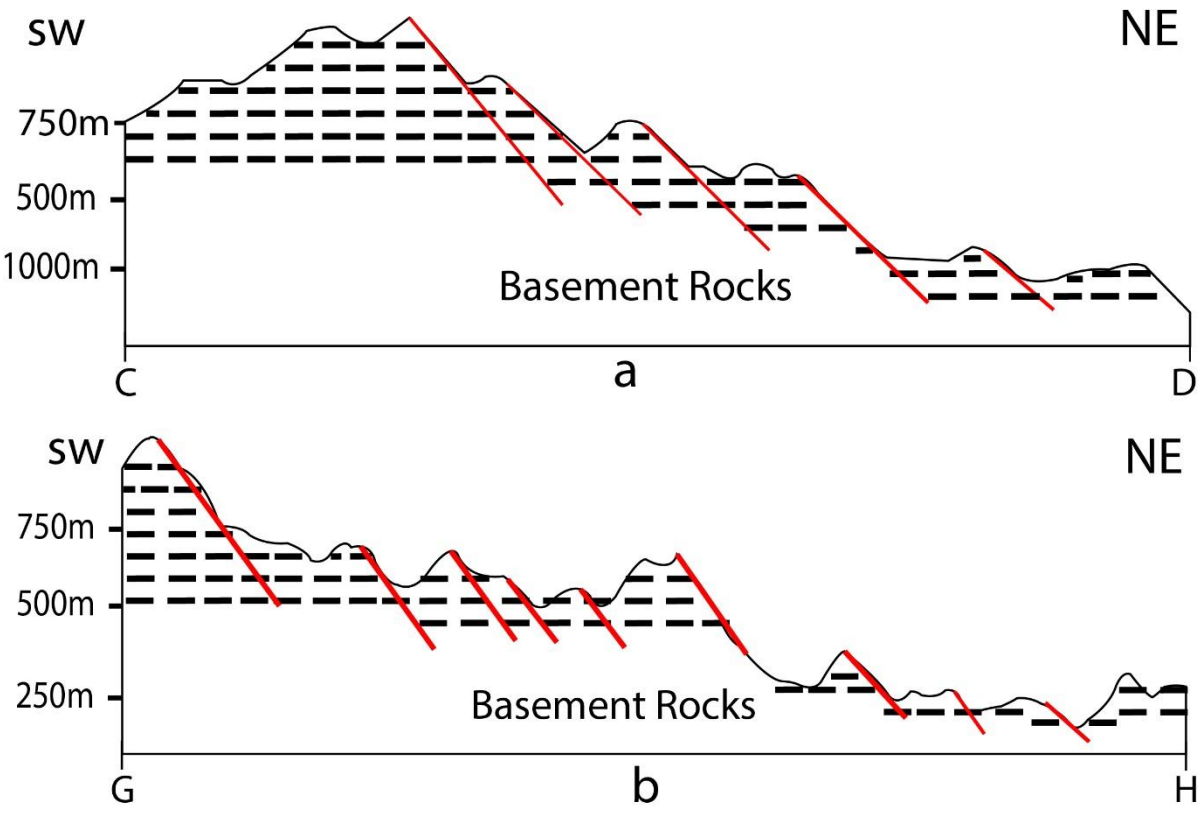

Fig. 4.15. Cross sections along (a) northernmost (b) southmost part of the study area

The satellite image also allowed to identify aligned ridges which follow the general trend of the region and along which faults are delineated (see fig. 4.14a above).

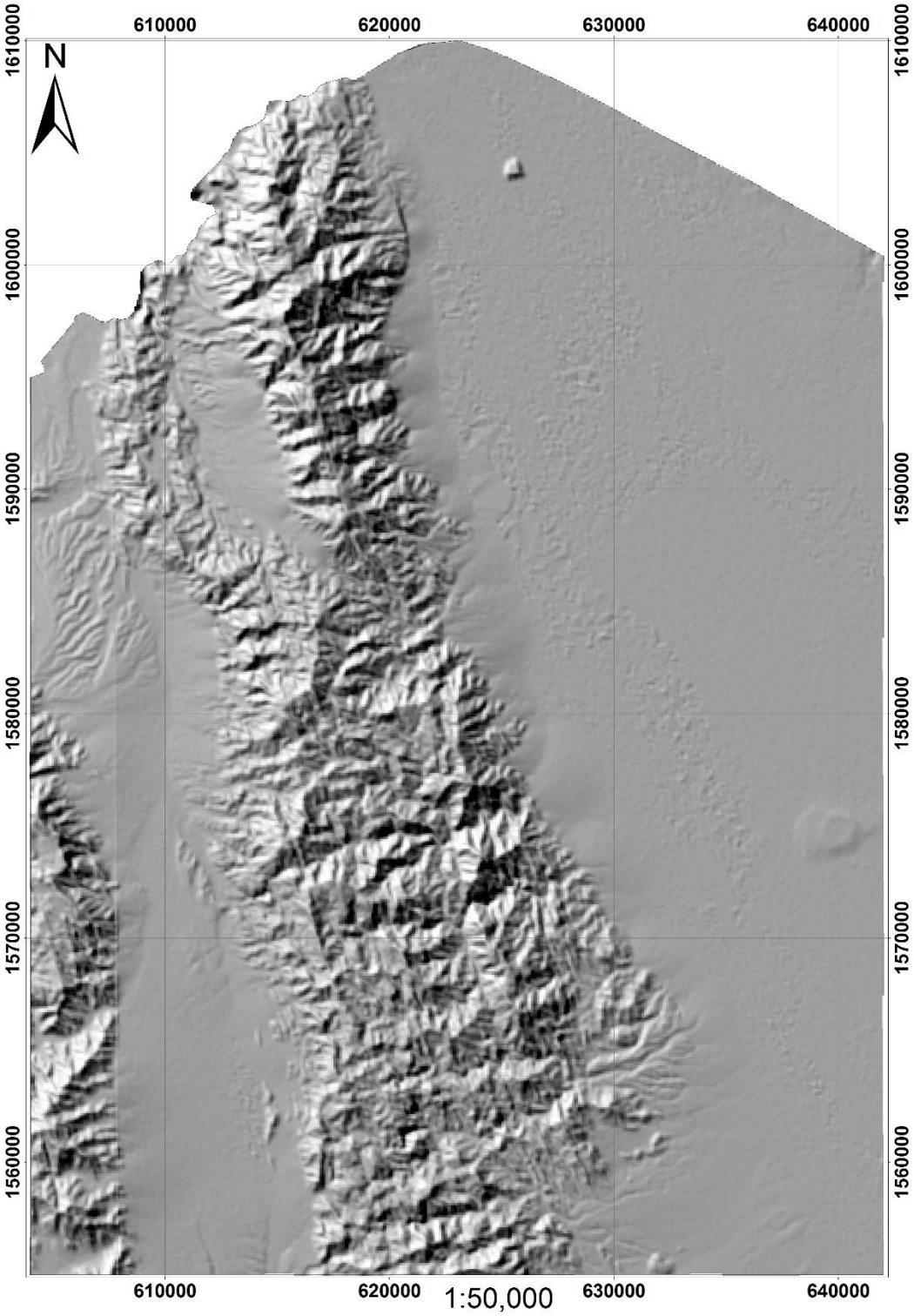

Fig. 4.16 Hill shade of the study area with the default sun elevation angle 45^0 and azimuth angle 315^0

4.2.2.4 Spectral Reflectance Curve from field observation

From observation made during the field work ground truth was collected where various lithologic units' geographic locations were gathered using ordinary GPS. The distribution of selected observation points for extraction of raster value for each lithologic unit mapped in bands 1 to 7 (see fig. 4.17; refer appendix E) is in such a way that all lithologic units can be represented by at least 1 observation point.

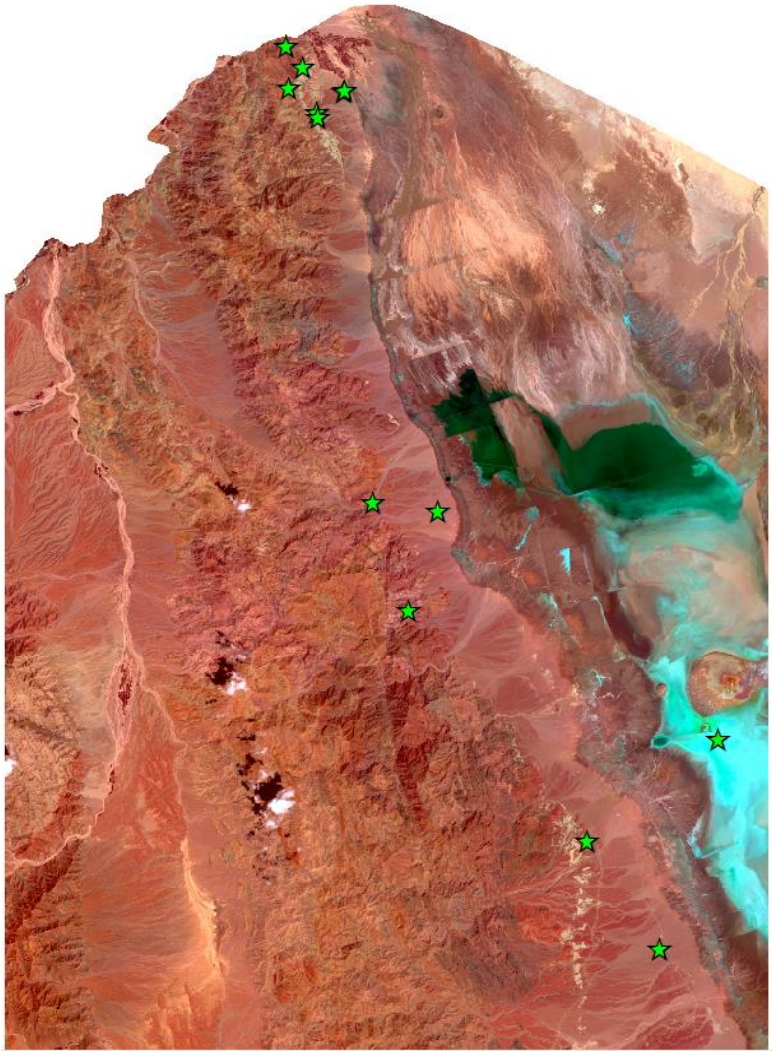

Fig. 4.17 Distribution of observation points used for constructing spectral reflectance curve of rock types mapped in the study area

Here a point shapefile is created from the field observation points and then the spectral value of each lithologic unit is plotted for bands 1-7. For example the salt formation has a high spectral reflectance in Band 5 (see fig. 4.18) low spectral reflectance in band 7. These bands

are used to map salt formation. Following the same principle the other rock types within the study area were mapped along with information gathered from satellite image enhancement techniques and field observation and existing regional geological map.

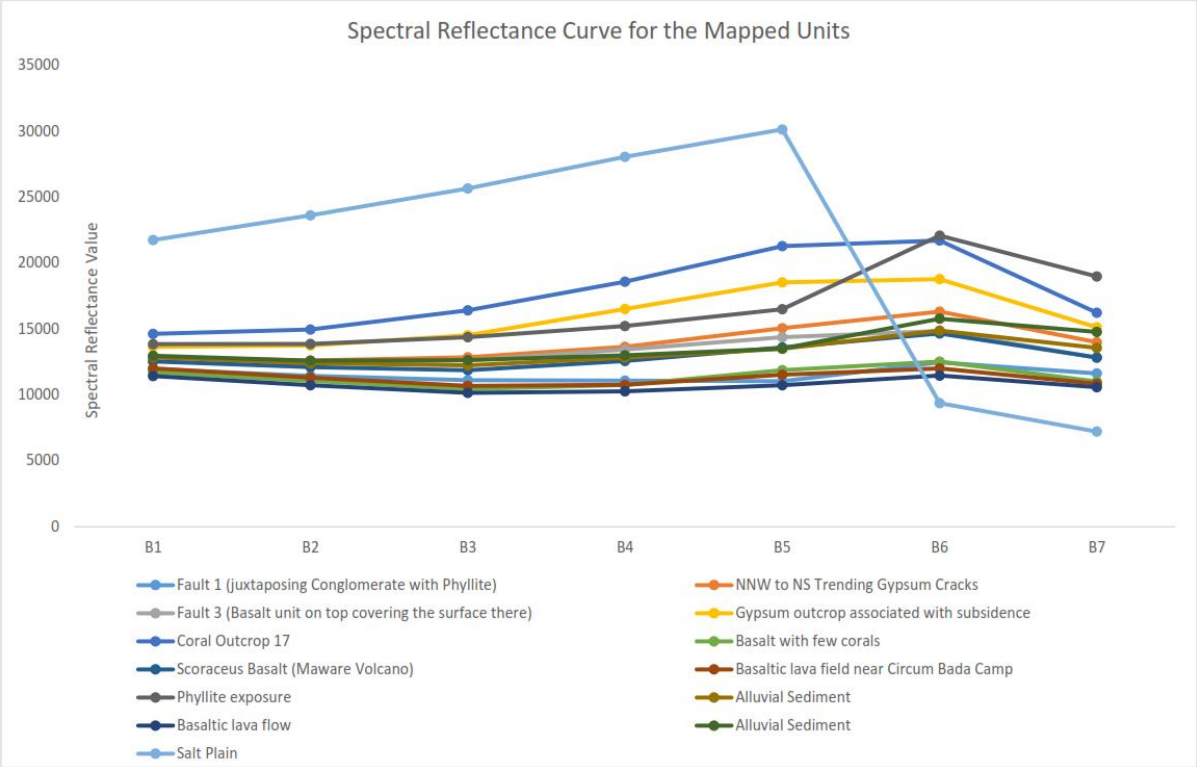

Fig. 4.18 Spectral reflectance curve from field observation points for various lithologic units mapped

4.3 Seismic Data Analysis

It is believed that the western margin of the basin has been affected by repeated normal faulting (e.g., Holwerda & Hutchinson, 1968). However, generally the fault scarp surfaces are rapidly obliterated, being formed in unconsolidated clastic debris and being constantly buried by the influx of new debris. At depth, these surfaces do persist as marked fault surfaces. Seismic data obtained from potash companies in the Danakil Depression is examined to reveal the fault scarp surfaces buried in the subsurface.

Potash projects in the study area conducted seismic investigations for various reasons: to assess the efficacy of the seismic method in the Danakil basin; to set parameters for a possible 2D production survey; to establish the continuity of the potash horizons in the deposit over the exploration area and the overall structure of the deposit; to aid in positioning drilling locations

and to outline any possible hazards such as faults or collapse structures which might impact future drilling/mining operations. (BHP, 2012; Allana, 2012; Circum, 2015).

Allana Potash acquired a total of 5 seismic lines, of which 2 were run approximately perpendicular to the structure of the Danakil graben and 3 were run parallel to the structure at different distances from the assumed graben shoulder (see fig. 4.19 & 4.20 below).

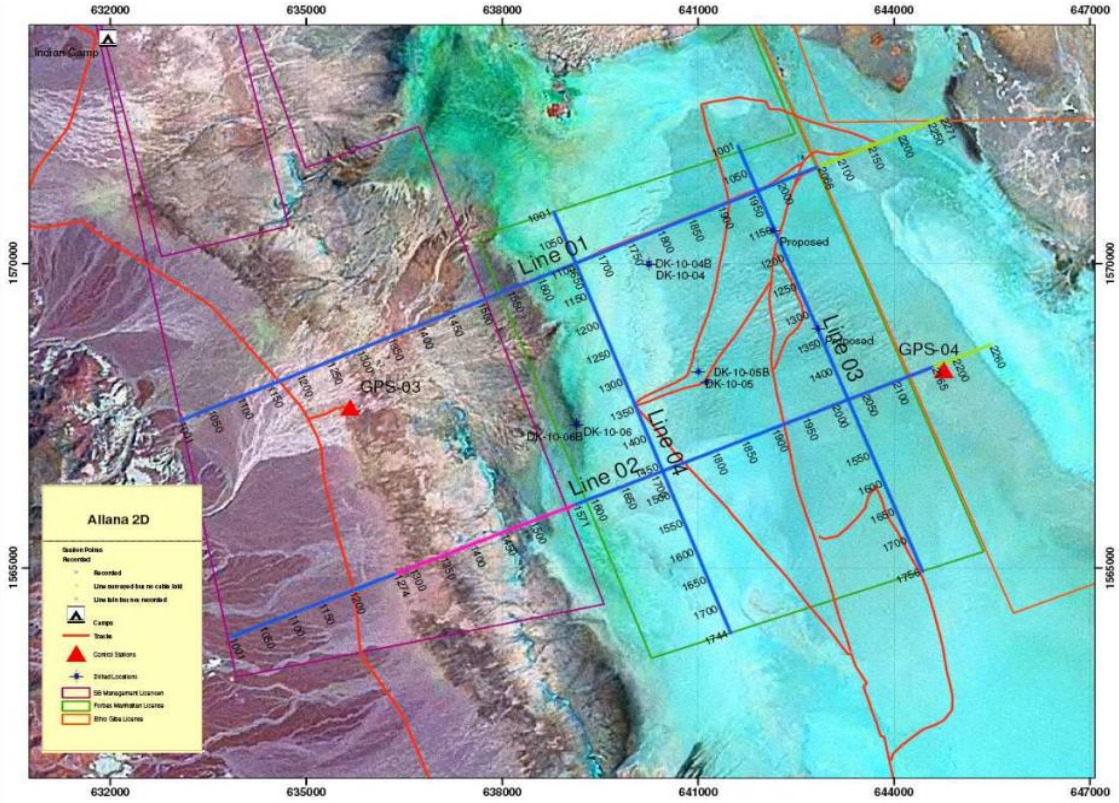

Fig. 4.19 Satellite image of Danakil area with position of seismic survey lines (marked in blue) (Allana, 2012)

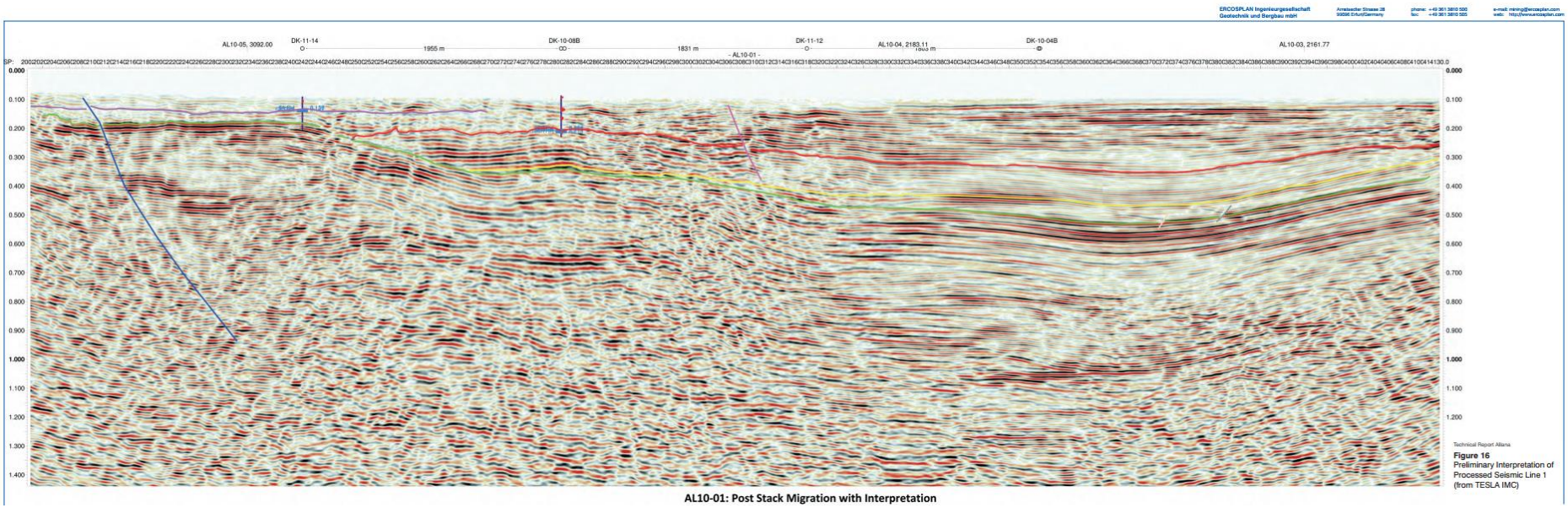

(a)

Fig. 4.20 Preliminary interpretation of processed seismic line 1 across the basin (a) seismic line 3 along the basin (b) (Allana, 2012)

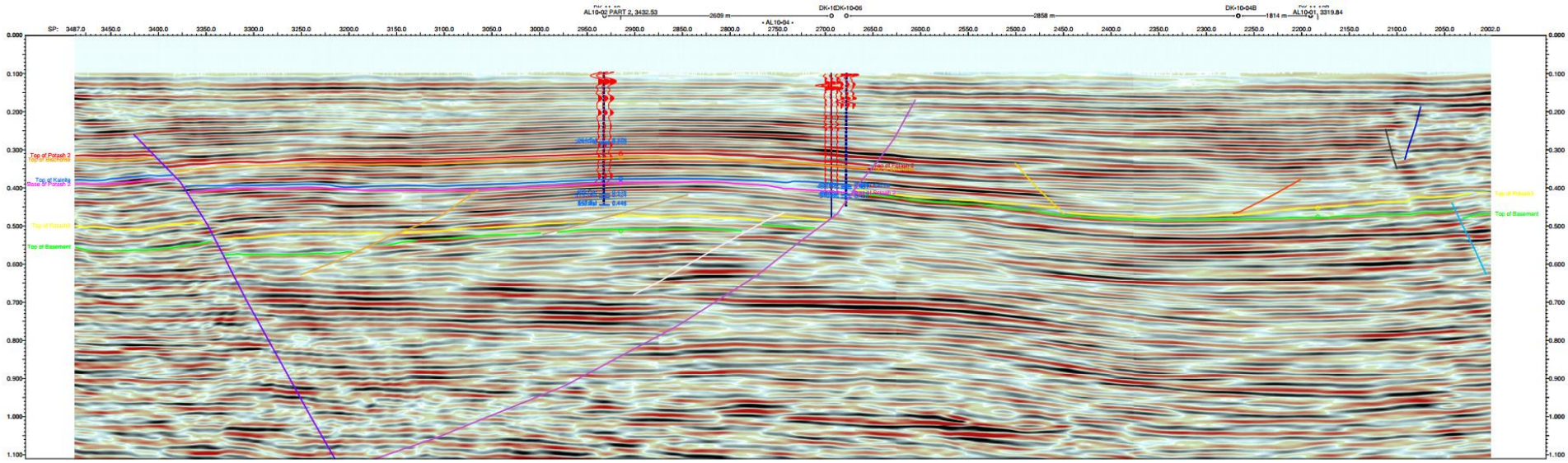

Fig. 4.20 (continued)

On the other side eight seismic lines were acquired by BHP in 2012 as indicated in fig. 4.21 below.

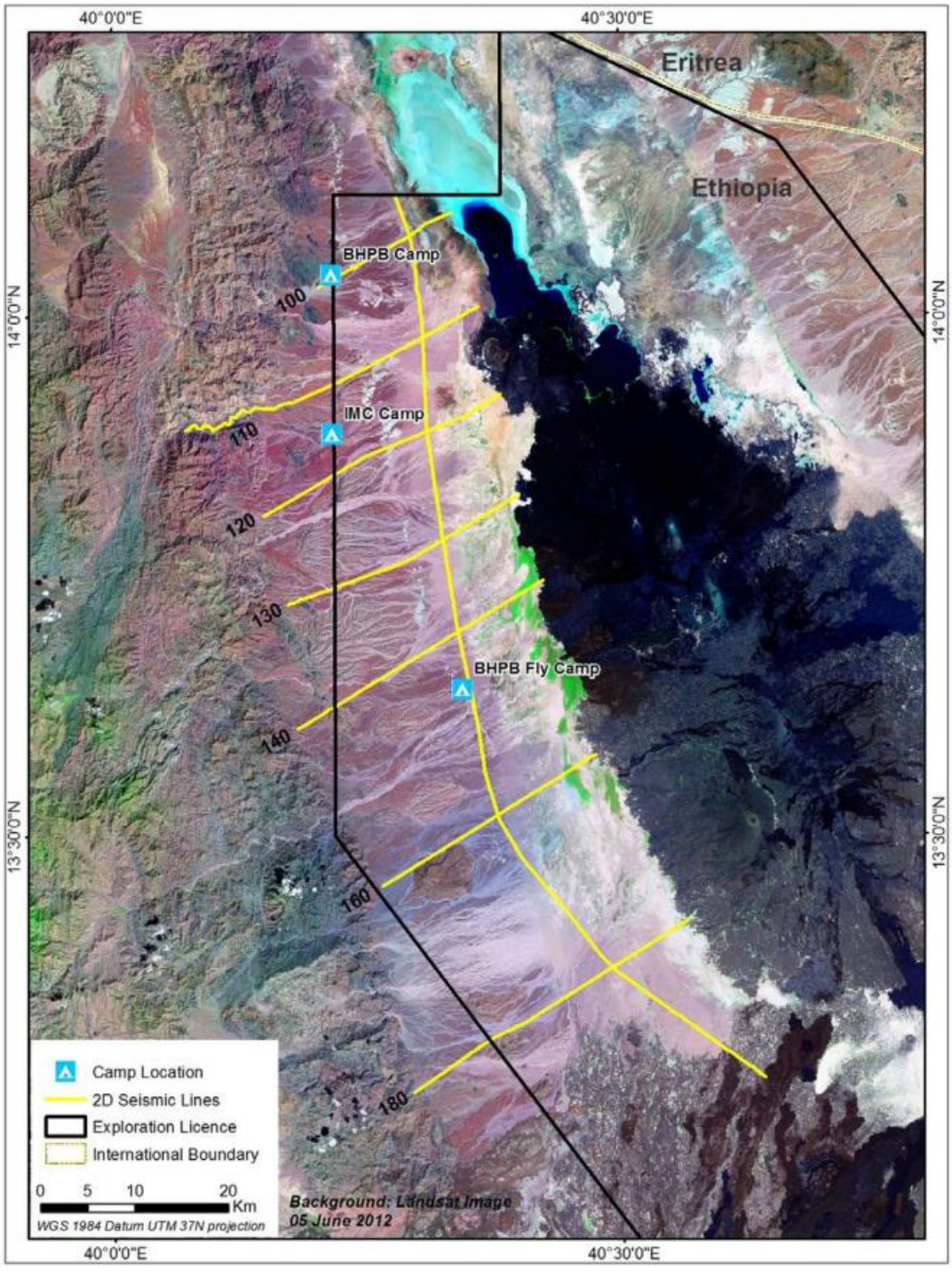

Fig. 4.21 Location of the production seismic survey lines by BHP Billiton. Traverse lines from north to south L100, L110, L120, L130, L140, L160, L180 and north south trending tie line T110 (not labelled in image) (BHP, 2012)

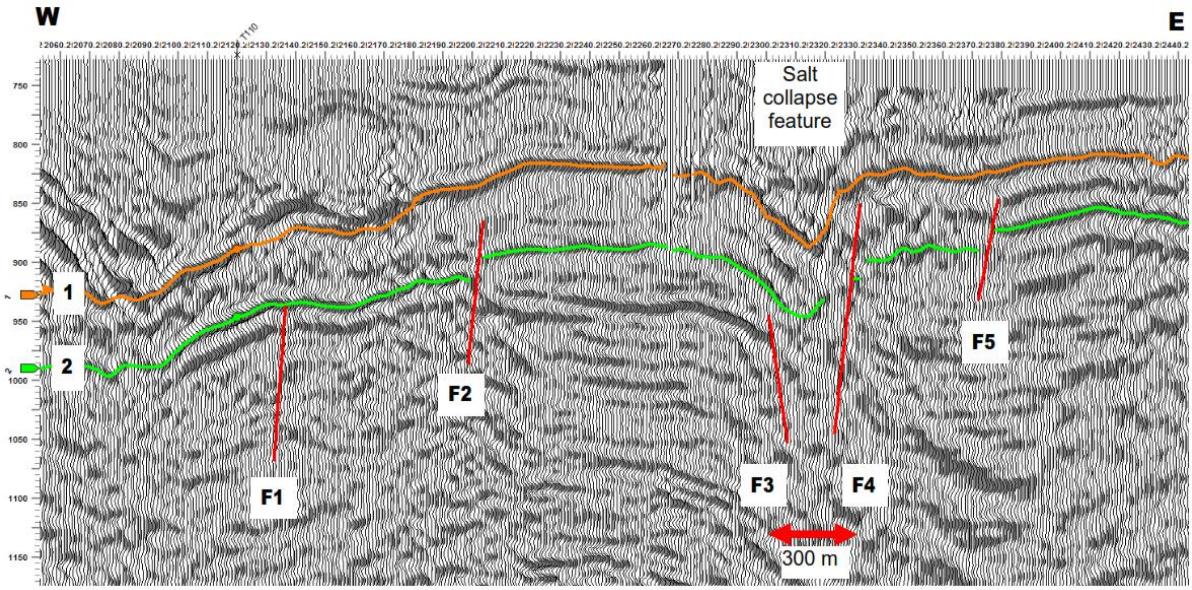

Fig. 4.22 Faulting and salt collapse structures on seismic line 100. Faults are indicated in red. The faults labelled F1, F2 and F5 show normal offset and isochron thickening typical of the basin. Faults F3 and F4 appear related to be a collapse feature (BHP, 2012b).

Circum (2015) carried out seismic survey along 9 seismic lines totalling 77.93 km (see fig 4.23 below) in 2014.

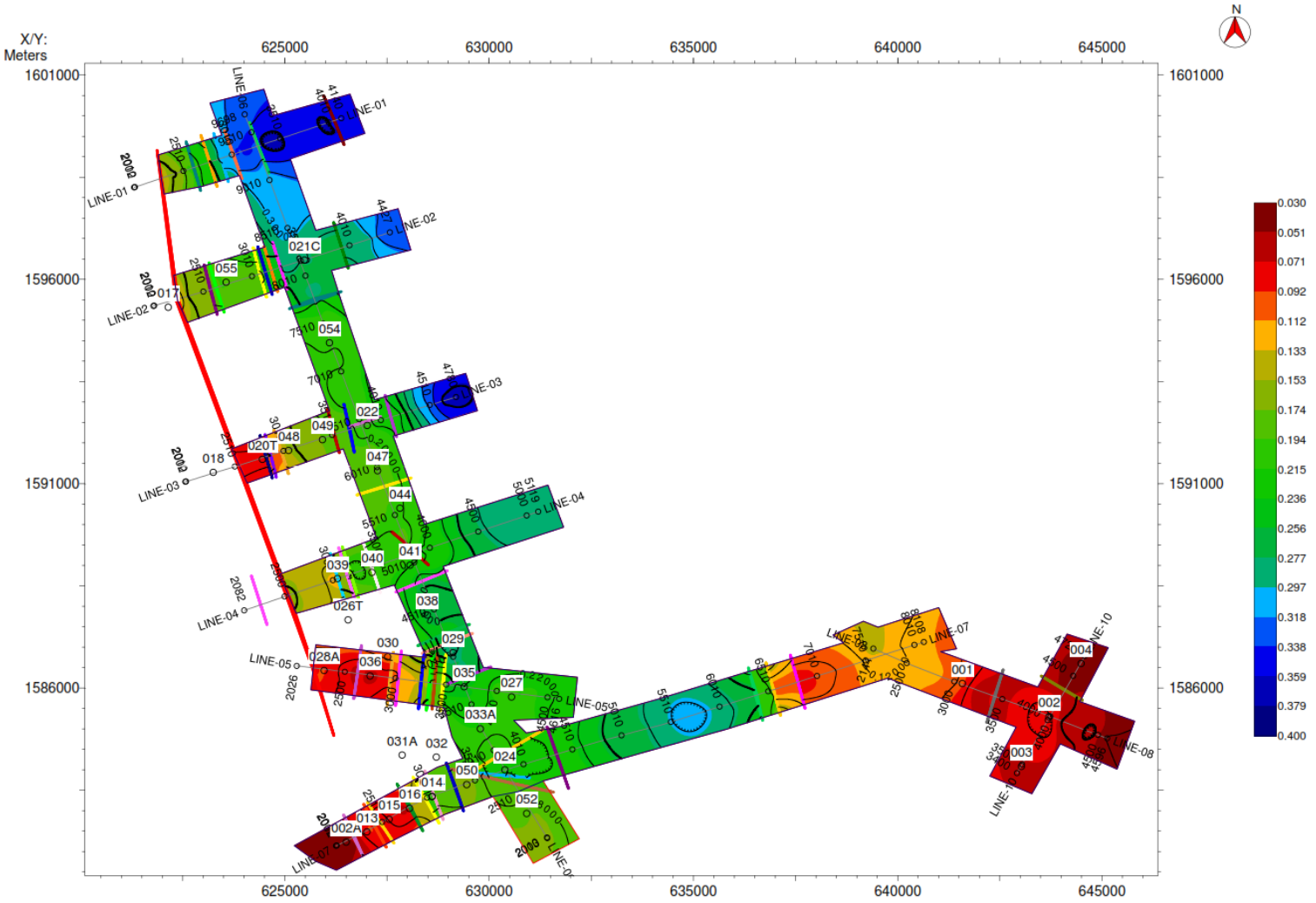

Fig. 4.23 Location of seismic survey lines by Circum Minerals.

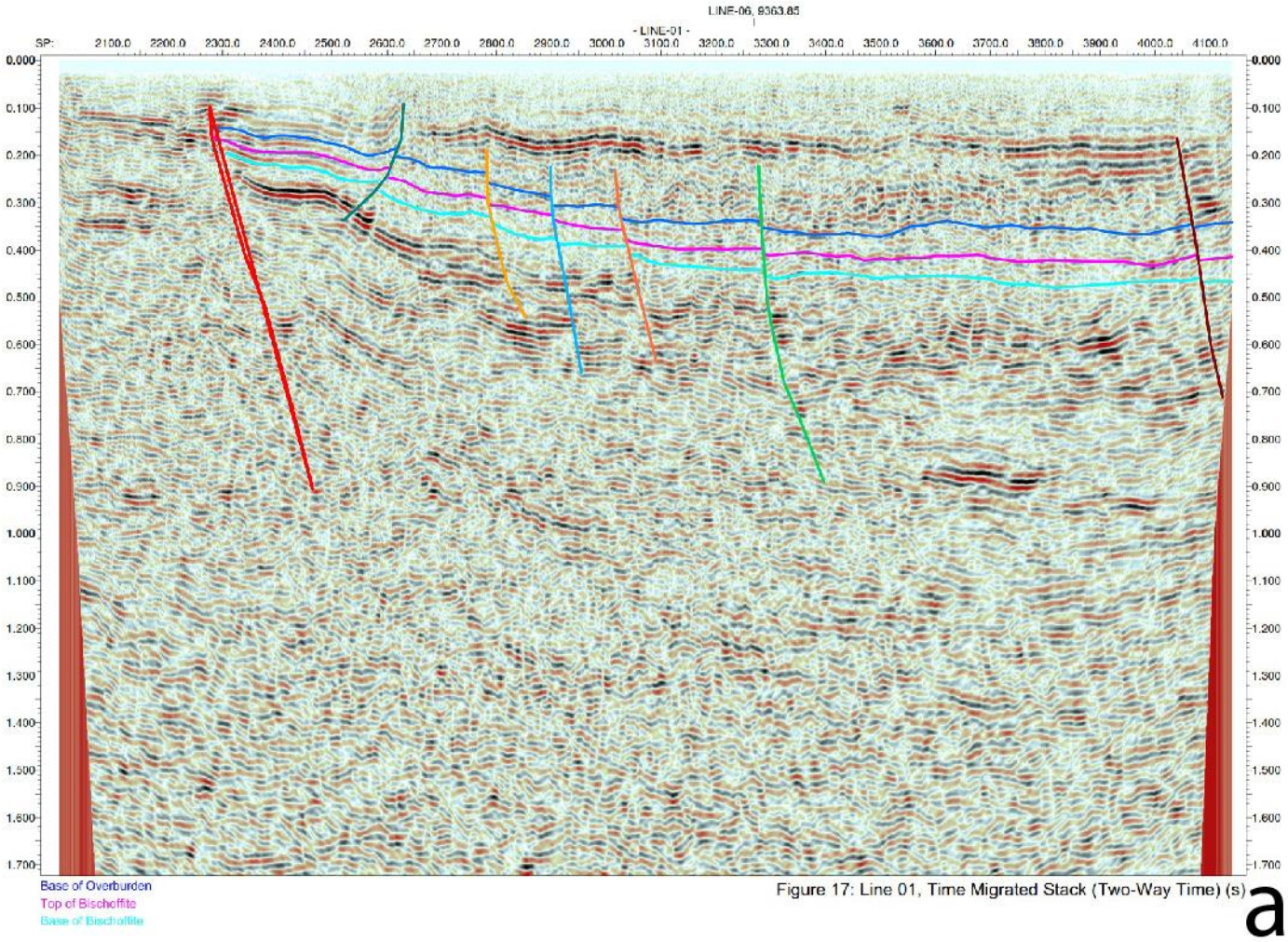

Fig. 4.24 seismic interpretation along line 01 (a) and line 02 (b)(Circum, 2015)

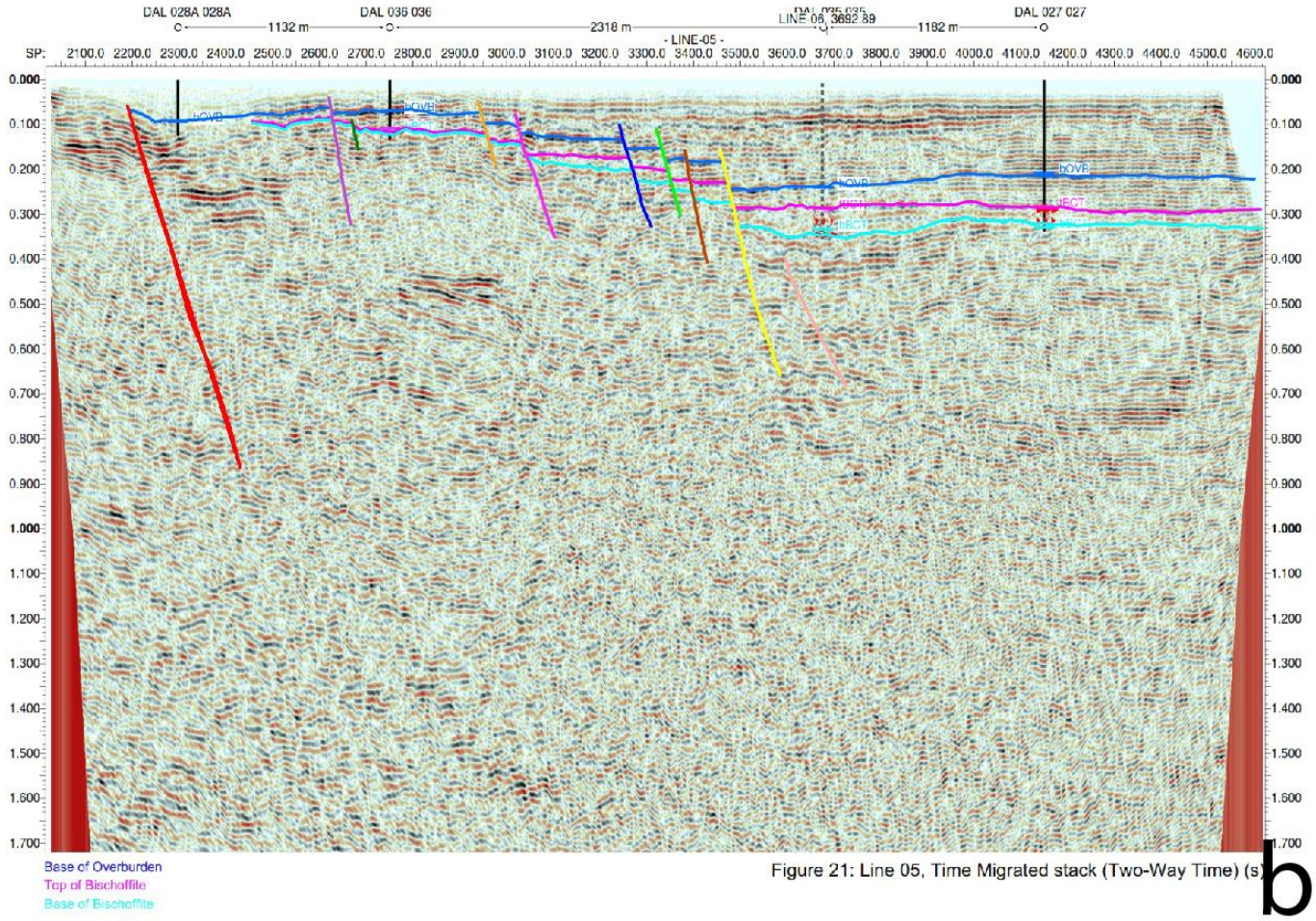

Fig. 4.24 (continued)

CHAPTER 5

DISCUSSION

5.1 Geology and Structural Geology of Dallol Depression

5.1.1 Results from Structural Analysis

Generally, from the analysis of field measurement of faults, there are three different trends: NNW, N-S and NE (See fig. 4.1). Most of the geologic structures: faults, joints and cracks observed in the study area strike NNW bearing the Red Sea (or general) trend. The general trend of these structures reflects the regional tectonic stress trajectories at the time of fracturing. The NE faults affect the alluvial sediments evidencing that they are faults of younger generation (see enclosed geological map). Angular unconformity observed between two conglomerate units indicates a period of active tectonism. The measured foliations (slatey cleavages) trend NNW. The geologic map produced clearly indicate that many of the structures are concentrated in the western margin of the Danakil Depression.

Even though the scarcity of distinctive offset markers in the study area severely limits quantitative analysis, the P- and T-axes can be used as the basis for calculating an "unweight" moment tensor summation by using Bingham statistics in which the P- and T-axes are linked to one another according to Marrett and Allmendinger (1990). Kinematic analysis of fault-slip data revealed that the extension axis is NE-SW and the shortening axis is NW-SE (see fig. 4.5c). The extension direction coincides with the regional extension direction (Keir et al., 2013). The analysis also indicated that the sense of movement is oblique slip with dominant dip slip component; the faults being normal left lateral faults.

Principal axes of stress determined from dynamic analysis of conjugate set of faults indicated that these set of faults were formed under stress condition where the maximum principal stress (σ_1) was oriented NW and the minimum principal stress (σ_3) was trending SW (refer fig. 4.7). The orientation of σ_1 is parallel to the NNW–SSE Red Sea trend. The tensional stress represented by σ_3 is parallel to the overall extension direction across the Red Sea rift (Keir et al., 2013).

Differential GPS elevation measurements and DEM extracted elevations indicate that altitudes for a given coral reef sequences vary greatly from the south (-30m) to the north (+170 m) (refer fig. 4.7). The variation systematically increases towards north. The quantified vertical

movement on the western margin of the Danakil Depression for the geologic time from 200ka to the present ranges from 0.008 cm/yr to 0.09 cm/yr (see table 5.1). This explains the isolation of the Dallol Depression from the Red Sea. The marine incursion of the Dallol is controlled by the continuous uplifting process in combination with the sea level drop.

Table 5.1 outcrops for which deformation rate has been calculated

Outcrop with Sequence A	Relative distance S-N (m)	Sea level at deposition of MIS7 (m)	Actual elevation of MIS7 (m)	(D) Total displacement of MIS7 (m)	Subsidence/uplift rate R (z/200ky * 100) (cm/yr)
CO3/11	0	-10	-32	-22	-0.011
CO1	18	-10	6.7	16.7	0.008
CO12	18.5	-10	8.2	18.2	0.009
CO7	19	-10	10.1	20.1	0.010
CO14	20	-10	20	30	0.015
CO4	23.5	-10	38.8	48.8	0.024
CO6	36.5	-10	103.2	113.2	0.057
CO18	65	-10	170.1	180.1	0.090
CO16	66.5	-10	110	120	0.060
CO19	68.5	-10	93.8	103.8	0.052

5.1.2 Results from Remote Sensing Data Analysis

Geological map of the study area was a result of interpretation of Landsat 8 and SRTM (Shuttle Radar Topography Mission) data (refer enclosed geological map). The band combination and band ratioing enhancement techniques made images interpretable to extract geologic information. These enhancement techniques applied on the acquired Landsat 8 images lead to the easier identification of the geologic units in the study area. This was accomplished accompanied by existing regional 1:250,000 and 1: 500,000 geological maps and verification and confirmation of ground trothing or field observation. Basement rocks, gypsum and associated coral reefs, basalt, alluvial sediments and conglomerates, salt formation, limestone and sandstone were identified.

The RGB band combination which is found to be the best in discriminating most of the lithologies within the study area is 7-4-2. Using this band combination salt formation, gypsum, conglomerate, alluvial sediments and salt mixed with mud were identified. This study made use of band ratio images to further discriminate lithologies where the best ratios were 4/2, 6/7, 6/5 and 5/7, 3/5, 3/2. These band ratio RGB colour composite images enabled to discriminate between sandstone and limestone as well as further confirm the other lithology discriminations

from band combination operation. Band ratio image 4/2, 6/7, 6/5 best discriminate almost all lithologies. This is because this band ratio operation used bands 6 and 7 (geology band, Mwaniki et al., 2015) which better discriminate lithologies. In this image sandstone appears distinctly bright (refer fig. 4.12) since it is light toned in SWIR range (Gupta, 2003). This made it easy to discriminate sandstone which appears similar with other lithologies, for example, phyllite in another band combination as in 7-3-1or 4-3-2. Alluvium is mapped by making use of the 5/4, 6/5, 7/6 band combination where it appears red and forming unique pattern on the satellite image; alluvial sediments were easily recognized on the satellite image from their fan pattern. The detailed mapping of the coral reefs and evaporites was based on satellite image where distinction is made only between coral reefs and evaporites and other lithologies as substrates. Generally, on the satellite image the substrate appear dark, evaporite appears lighter and coral reefs appear brownish.

Several shaded relief maps were created for the present study to delineate structures. This technique is effective in creating images that enhance geomorphic features thus simplifying structure extraction. After several tests, the best shaded relief which lead to the easy extraction of structures was the one with 45^0 and 135^0 sun elevation and azimuth angles respectively (see fig. 5.1). This shaded relief clearly shown the structures in the study area by enhancing subtle morphological variation supported by optical remote sensing data. Many of the structures delineated from the DEM data are found at the western margin of the Dallol Depression. Rose diagram of these structures reflect prevalence of NNW trend (refer fig. 4.1g). The mapped structures follow the regional trend. The evolution of these structures is related to the Red Sea rift tectonics.

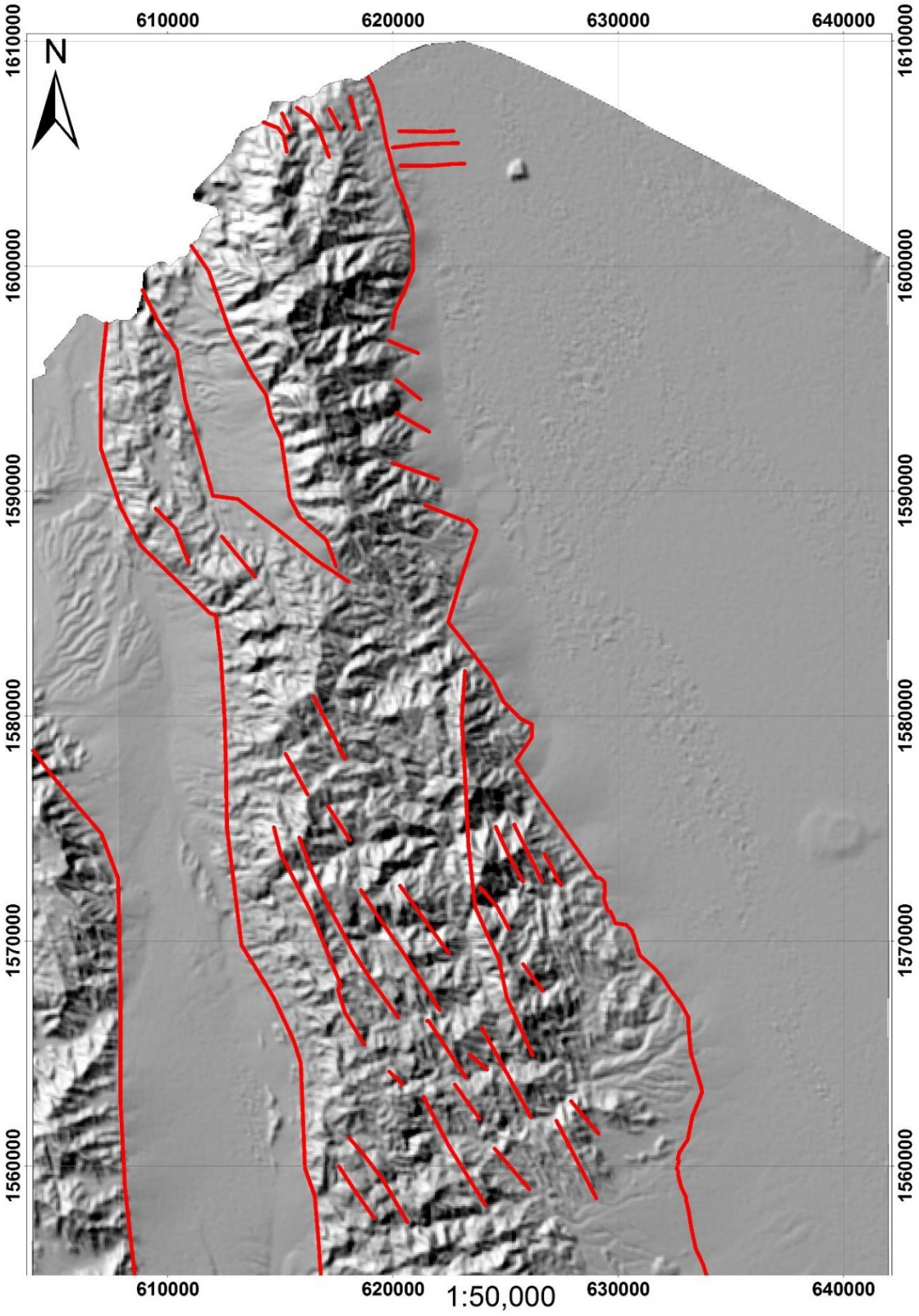

Fig. 5.1 Hill shade of the study area with the default sun elevation angle 45^0 and azimuth angle 315^0 with its respective structures

There are also structures trending N-S and E-W but these structures are subordinate. E-W trending fault are observed cutting through recent alluvial sediments which imply that they are of younger generation.

Along the SW part of the study area DEM 3D path profile (see fig. 5.2) revealed existence of marginal graben. This graben is bounded on both of its sides by faults trending NNW. The centre of this marginal graben is filled with alluvial sediment and the blocks are constituted of Basement rock.

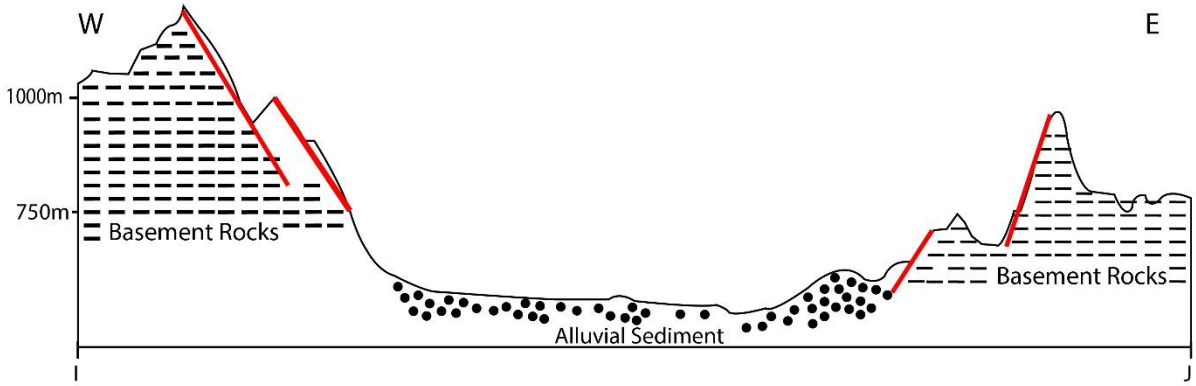

Fig. 5.2 Cross section along marginal graben in the SW part of the study area

Constructions of cross sections from DEM: one from the northern-most part (fig. 4.1.5a) and another from the southern-most part (fig. 4.1.5b) of the study area indicate steps of faulting dipping to the centre of the basin within a general trend of NNW (see fig. 5.1 and 4.1). Based on this manual extraction of lineaments, it is confirmed that these lineaments represent fault lines.

5.1.3 Results from Seismic Data Analysis

The faults interpreted from seismic data which run across the basin (Allana, 2012; BHP, 2012b; Circum, 2015) can be correlated to the fault interpreted from the remote sensing data and field data. These faults bound the basin along the western margin. These structures which are found along the western margin of the study area are subsurface continuation of faults (refer fig. 4.20; 4.21; 4.22 and 4.24) observed in the field and from Landsat and DEM data and demarcate the basin boundary. These faults are active but lack sufficient energy to rupture the surface (i.e., blind normal faults), or that these faults were active during the early stages of Afar rifting, but have now been concealed by rapid sedimentation associated with alluvial fan deposits in the study area.

Seismic data from Allana (2012) allowed identification of 47 normal faults along all the 4 seismic lines: two along the basin and two across the basin. The normal faults identified trend NE, NNW, NW and N-S. The two dominant trends are NW and NE with only two of them trending NNW and N-S. The identified faults are mainly in the west/ centre west of the survey

area (refer fig. 4.19) particularly where the deltaic areas descend into the basin itself. Throw of the normal faults range from 5 to 155m (refer appendix F). The two largest throws, 105 and 155m, were seen on line 4 (refer fig. 4.19) which runs parallel to the margin. Preliminary interpretation indicates that east of DH 10-08B and west of DH 10-12 the salt and basement reflectors are disturbed (see fig. 4.20 above). This imply that major fault zone exists, and it separates the shallow graben flank from the deeper graben centre. According to Allana (2012) seismic data revealed that there is evidence of the basin rising in the extreme east.

There is a general similarity between the structural trends of the studied area from field investigation and remote sensing and the orientations of the subsurface structural features from seismic data. The measured structural features and structures extracted from remote sensing data probably represent an upward continuation of subsurface buried structures.

The observation that raised coral reefs are found in the study area can be explained by the existence of faults with a throw of 5-155 m (Allana, 2012) or reaching >240m (Circum, 2015) from seismic data and elevation data from DEM. It is observed that coral reefs in the north of the study area are elevated than the coral reefs in the south of the study area. This is due to much higher uplifting related to normal faulting in the north than in the south.

According to BHP (2012b) numerous smaller faults are delineated from the seismic data and most appear to be normal faults related to the basin extension and growth, some may be collapse features due to the solution and removal of underlying salt (fig. 4.22).

Seismic lines from Circum exhibit faulting (refer fig 4.24 a & b). The interpreted faults have throw ranging from 10m to >240m with downthrow generally to the centre of the basin (Circum, 2015).

5.2 Structural Control on the Marine Incursion of the Dallol Depression

Bonatti et al. (1971) hypothesised that Dallol Depression was isolated from the Red Sea at ~32 ky based on the youngest coral reef dating they determined. They suggested this because this time roughly correspond to the uprising dome of the Alid volcano at ~36 ky (Duffield et al., 1997). However detailed analysis of sedimentary succession around Dandiero Basin, which is bounded by the slopes of Alid volcano on its north side, reported no marine sediments (Abbate et al., 2004). This indicates that the Dallol Depression connection with the Red Sea was not

through the Gulf of Zula. Hence the desiccation of the marine incursion of the Dallol Depression cannot be explained by this hypothesis. Besides the youngest coral reefs dated are 120 ky (Foubert et al., 2015; Jaramillo-Vogel et al., 2015). This implies that the final desiccation took place 120 ky. The uplift rates determined explain the isolation of the Depression from the Red Sea in combination with the sea level drop. Here as suggested by Holwerda & Hutchinson (1968) Danakil Depression could have been flooded by Red Sea water influx from the east. On the eastern side of the Depression west of Danakil Block satellite images revealed that there is evaporites and coral reef exposures. Seismic data also support this hypothesis which revealed that there is evidence of the basin rising in the extreme east.

5.3 Pleistocene History of the Danakil Depression

Geologic history of the Danakil Depression began from its sinking. Based on radiometric age determination the Depression started sinking in the lower Miocene (23-25 my). From its birth to the present time volcanism, marine incursion, lacustrine, evaporitic and continental deposition took place contemporaneously (Barberi et al., 1972a). After the onset of the graben structure and probably up to the Pleistocene, a salt unit has been deposited inside the central part of the graben area. U/Th dating of coral reefs within the Depression revealed that the Depression has been flooded at least twice during the Pleistocene period (Foubert et a., 2015; Jaramillo-Vogel et al., 2015). According to Foubert et al. (2015), Jaramillo-Vogel et al. (2015) and Balemwal Atnafu et al. (2015) the intermediate period between the two marine event sequences is represented by lacustrine sedimentation.

CHAPTER 6

CONCLUSION AND RECOMMENDATION

6.1 Conclusion

In this study fieldwork, remote sensing and seismic method were employed to map lithologies and structures in the Dallol Depression and evaluate structural control on the Red Sea incursion of the Depression. Consequently, conclusions drawn from this research are listed in points below

1. The geologic map produced from integrated field work, remote sensing and seismic data indicate that there are basement rocks: phyllite & slate and Mesozoic sandstone and limestone and Quaternary volcanics and sediments: basalt, pyroclastic fall deposits, alluvial sediments and conglomerates, gypsum and associated corals and salt formation. This shows that the northern Danakil Depression and the western margin may represent the complete sequence of rocks spanning from the Neoproterozoic to the Holocene.
2. Remote sensing data: Landsat 8 and SRTM DEM enabled to map the lithologies and structures of the study area accompanied by ground trothing of satellite image with an advantage of low cost and large area coverage. Band combination and band ratioing played a significant role in discriminating and identifying different rock types by delivering good quality images that can be used to validate and update existing regional maps. Comparison of enhancement techniques shows that band ratio combination performed better both in the visualization and discrimination ability than band combination.
3. The DEM from SRTM was the most important source for identifying structures. The map produced shows that there are three general trends of structures: NNW, NS and NE in which NNW trending structures dominate. The evolution of the NNW structures is related to the Red Sea/Danakil rift tectonics. Most of the faults are extensional.
4. Accurate delineation of geological boundaries and tracing regional tectonic structures is major problem faced in conventional geological mapping. This study demonstrated the potential of digital image processing techniques for tackling this problem.
5. The Red Sea incursion and flooding of the Dallol Depression is controlled by regional structures mapped within the study area. Uplift and sea level drop lead to the desiccation of the Depression from the Red Sea.

6. This study has shown that Landsat 8 imagery and SRTM data are useful and applicable to regionally map lithologies and structures in arid areas like the Dallol Depression where there

are sparse vegetative coverage and poor accessibility due to some reasons. The use of remotely sensed data for geological mapping adds compliments to the traditional mapping process.

7. The detection of lineaments from digital elevation models shows that the main orientations correspond to the directions of the main regional tectonic structures: NNW-SSE Red sea.
8. Field measurement of structures generally reveal similar orientations to those structures obtained from remote sensing analysis.
9. It is still possible that different rock types even after operating enhancement techniques might produce similar expression. For this reason, one must be cautious and the information extraction should be supported by ground verification and available geological maps.
10. If similar study could be conducted in the east margin of the Depression it would further clarify the structural control on the marine incursion and flooding history of the Depression observed from field investigation, remote sensing, elevation measurement and seismic data.

6.2 Recommendation

The Afar Depression is quite a good site to employ remote sensing techniques for geological studies since it lacks vegetation cover and has poor hospitality due to its climatic condition. Hence it is recommended to take advantage of this lack of vegetation and soil cover to undergo further investigation of the province using remote sensing. In the future, the regional geologic map of the whole Danakil Depression even the whole Afar region can be updated by applying the remote sensing methodologies employed here and elsewhere. Advanced image enhancement techniques could give more information to map lithologies and structures. It is recommended to use radar data or DEM data with spatial resolution better than the DEMs used in the present study which will improve much better structural interpretation. Available raw (or not processed) seismic data from potash companies can be used to study subsurface geologic structures to constrain the complete geologic history of the study locale.

Moreover, Danakil Depression is an interesting locale to study plate separation since it is proposed that a new oceanic crust will form in the near geologic time. There are changes made of the infrastructure development related to the salt mine activity that the region is becoming more accessible this days to undergo fieldwork.

The quaternary alluvial gravels can be used as quarry sites due to their surface occurrence and proximity to the new road under construction around the potash company sites in the

Depression since these are one of the preferred aggregates used for construction, buildings, highways, airport runways, and other structures (Mansour & Madkour, 2015)

REFERENCES

Abbate, E., Beraki Woldehaimanot, B., Bruni, P., Falorni, P., Papini, M., Sagri, M., Simret Girmay and TeweldeMedhin Tecle. (2004). Geology of the Homo-bearing Pleistocene Dandiero basin (Buina region, Eritrean Danakil Depression). *Rivista Italiana di Paleontologia Stratigrafia.* **110**: 5-34.

Abbate, E., Bruni, P. and Sagri, M. (2015). *Landscape and Landforms of Ethiopia*, Springer, Neatherland, 33-64pp.

Abbate, E., Passerini, P. and Zan, L. (1995). Strike-slip faults in a rift area: A transect in the Afar Triangle, East Africa. *Tectonophysics*. **241**: 67-97.

Adiri, Z., Harti, A., Jellouli, A., Machaa, L. and Bacha, E (2016). Lithological mapping using Landsat 8 OLI and Terra ASTER multispectral data in the Bas Drâa inlier, Moroccan Anti Atlas. *J. Appl. Remote Sens*. **10**: 1-14.

Alebachew Beyene and Abdelsalam, M. G. (2005). Tectonics of the Afar Depression: a review and synthesis. *J. Afr. Earth Sci.* **41:** 41-59.

Ali, E., Abdegalil, M. Y. and Musa, A. E. (2016). Assessment of image ratio technique for gold exploration in arid region using Landsat ETM+7: limitations and possible source of misinterpretations. *Int. J. Geosci. and Geomatic.* **4**: 17-23.

Ali, E. A., El Khidir, S. O., Babikir, I. A.A. and Abdelrahman, E.M. (2012). Landsat ETM+7 digital image processing techniques for lithological and structural lineament enhancement: case study around Abidiya area, Sudan. *The Open Remote Sensing Journal.* **5**: 83-89.

Ali, A. S. O. and Pour, A. B. (2014). Lithological mapping and hydrothermal alteration using Landsat 8 data: a case study in Ariab mining district, red sea hills, Sudan. *Intl. J..Basic Appl. Sci.* **3***:* 199-208.

Allana Potash Corporation (2012). Updated resource report for the Danakil potash deposit, Afar State/Ethiopia. Retrieved from http://google.ch/url?sa=t&source =web&rct =j&url=http://otciq.com/otciq/ajax/showFinancialReportByld.pdf%3Fid%3D99671& ved=0ahUKEwiduoqRhK_PAhXlORoKHbtoDzQQFggzMAk&usg=AFQjCNFRZZP jN5WWo_5YmBX3t_7-w3s_yg on 27.09.2016.

Allmendinger, R.W. (2012). StereoWin Version 8. Retrieved from http://www. geo.cornell. edu/geology/faculty/RWA/programs.html. on 28.05.2015

Allmendinger, R. W. (2016). FaultKinWin Version 7.5. A Program for Analyzing Fault Slip Data for Windows^{TM} Computers. Retrieved from http://www.geo.cornell.edu/geology/ faculty/RWA/programs.html. on 28.05.2015.

Al-Shumaimri, M. S. (2012). Application of digital image processing techniques to geological and geomorphological features of Southwest Jordan. *J. Geogr. Geol*. **4**: 41-48.

Ameha Atnafu, Tesfaye Kidane, Rowland, J. and Bachtadse, V. (2013). Counterclockwise block rotation linked to the southward propagation and overlap of sub-aerial Red Sea rift segments, Afar Depression: insight from Paleomagnetism. *Tectonophysics.* **593**: 111-120.

Amusuk, D. J., Hashim, M., Pour, A. B. and Musa, S. I. (2016). Utilization of Landsat-8 data for lithological mapping of basement rocks of plateau state north central Nigeria **In:** *Proceeding International Conference on Geomatic and Geospatial Technology*, P 42. Kuala Lumpur, Malaysia.

Anderson, E., 1951. *The Dynamics of Faulting and Dyke Formation with Applications to Britain*, 2nd ed., Oliver and Boyd, Edinburgh, 140 PP.

Angelier, J. (1984). Tectonic analysis of fault slip data sets. *J. Geophys. Res.* **89**: 5835-5848.

Atalay Ayele, Jacques, E., Kassim, M., Tesfaye Kidane, Omar, A., Tait, S., Nercessian, A., Chabalier, J. B. and King, G. (2007). The volcano-seismic crisis in Afar, Ethiopia, starting September 2005. *Earth Planet. Sci. Lett*. **255**: 177-187.

Atalay Ayele, Keir, D., Ebinger, C., Wright, T. M., Stuart, G. W., Buck, W. R., Jacques, E., Ogubazghi, G. and Sholan, J. (2009). September 2005 mega-dike emplacement in the Manda-Harraro nascent oceanic rift (Afar Depression). *Geophys. Res. Lett*. **36**: L20306.

Augustithis, S. S. (1980). On the textures and treatment of the sylvite ore from the Danakil Depression, salt plane (piano del sale), Tigre, Ethiopia. *Chem. Erde*. **39**: 91-95.

Balemwal Atnafu, Tesfaye Kidane, Foubert, A., Vogel, D. J., Schaegis, J. C. and Henriet, J. P. (2015). Ocean history from Afar. News Article in Earth & Space Science News, Editors: Richman, B. T., Cohen, C. M. S., Gordon, W. S., Stein, C. A., Fuentes, J. D. and Halpern, D. *Eos*. **96** (2): 12-14.

Barberi, F., Borsi, S., Ferrara, G., Marinelli, G. Santacrose, R., Tazieff, H. and Varet, J. (1972a). Evolution of the Danakil Depression (Afar, Ethiopia) in light of radiometric age determinations. *J. Geol*. **80**: 720-729.

Barberi, F., Borsi, S., Ferrara, G., Marinelli, G. and Varet, J. (1970). Relations between tectonics and magmatology in the northern Danakil Depression (Ethiopia). *Phil. Trans. Roy. Soc. Lond. A*. **267**: 293-311.

Barberi, F. and Varet, J. (1970). The Erta Ale volcanic range (Danakil Depression, northern Afar, Ethiopia). *Bull. Volcanol.* **34**: 848-917.

Barberi, F. and Varet, J. (1977). Volcanism of Afar: small scale plate tectonics implications. *Geol. Soc. Am. Bull*. **88**: 1251-1266.

Barberi, F., Marinelli, G., Santacroce, R., Tazieff, H., Varet, J., Chedeville, E., Faure, H. and Giglia, G. (1973). Geology of Northern Afar (Ethiopia*). Rev. Geogr. Phys. Géol. Dyn*. **15:** 443-489.

Barberi, F., Tazieff, H. and Varet, J. (1972b). Volcanism in the Afar Depression: its tectonic and magmatic significance. *Tectonophysics*. **15**: 19-29.

Barisin, I., Leprince, S., Parson, B. and Wright, T. (2009). Surface displacements in the September 2005 Afar rifting event from satellite image matching: asymmetric uplift and faulting. *Geophys. Res. Lett*. **36**: L07301.

Barrat, J. A., Fourcade, S., Jahn, B. M., Cheminée, J. L. and Capdevile, R. (1998). Isotope (Sr, Nd, Pb, O) and trace element geochemistry of volcanics from Erta ‘Ale range (Ethiopia). *J. Volcano. Geotherm. Res*. **80**: 85-100.

Bastow, I. D., Nybalde, A. A., Staurt, G. W., Rooney, T. O. and Benoit, M. H. (2008). Upper mantle seismic structure beneath the Ethiopian hot spot: Rifting at the edge of the African low-velocity anomaly. *Geochem. Geophys. Geosyst*. **9**: Q12022.

Bastow, I. D., Stuart, G. W., Kendall, J. M. and Ebinger, C. J. (2005). Upper-mantle seismic structure in a region of incipient continental breakup: northern Ethiopian rift. *Geophys. J. Int*. **162**: 479-493.

Bekele Abebe, Acocella, V., Tesfaye Korme and Dereje Ayalew. (2007). Quaternary faulting and volcanism in the Main Ethiopian Rift. *J. Afr. Earth Sci*. **48**: 115-124.

Beyth, M. (1991). "Smooth" and "rough" propagation of spreading Southern Red Sea - Afar depression. *J. Afr. Earth Sci*. **13**: 157-171.

Black, R., Morton, W. H. and Varet, J. (1972). New data on Afar tectonics. *Nature Physical Science*. **240:** 170-173.

Billi, P., Semunesh Golla, and Dawit Tefferra (2015). Ethiopian Rivers. World Geomorphological Landscape, Editor: Billi, P. *Landscape and Landforms of Ethiopia*, Springer Science + Business Media Dordrecht. 89-116.

Boggs, S. (2006). *Principles of sedimentology and stratigraphy.* Pearson Prentice Hall, New Jersey, 662pp.

Bonatti, E., Cipriani, A. and Lupi, L. (2015). The Red Sea: Birth of an ocean. Springer Earth System Sciences. Editors: Rasul, N. M. A. and Stewart, I. C. F. *The Formation, Morphology, Oceanography and Environment of a Young Ocean Basin*. **19**: 29-44

Bonatti, E., Emiliani, C., Ostlund, G. and Rydell, H. (1971). Final Desiccation of the Afar Rift, Ethiopia. *Science*. **172**: 468-469.

Bosworth, W., Huchson, P. and McClay, K. (2005). The Red Sea and Gulf of Aden basins, *J. Afr. Earth Sci*. **43**: 334-378.

Bosworth W., Huchon, P. and McClay, K. (2012). The Red Sea and Gulf of Aden basins. Editors: Roberts, D. G. and Bally, A. W. *Phanerozoic Passive Margins, Cratonic Basins and Global Tectonic Maps*. Elsevier, Amsterdam. 63-139.

Bridge, D. L., Mickus, K., Gao, S. S., Abdelsalam, M. G. and Abera Alemu. (2012). Magnetic stripes of a transitional continental rift in Afar. *Geology*. **40**: 203-206.

Brinckmann, J., Käding, K.-CH., Knetsch, G., Kürsten, M., Mayrhofer, H. and Richert-Bernburg, G. (1970). Geological sketch map of the Danakil Depression. Bundesanstalt für Bodenforschung, Hannover.

Brinckmann, J. and Kürsten, M. (1972). Stratigraphie and undtektonik der Danakhil-Senke (NE Äthiopien). *Beih. Geol. Jb*. **116**: 5-86.

Broken Hill Proprietary (BHP) (2012a). A report on Danakil Potash Project (September 2008-September 2012). Unpublished technical report, BHP, Housten, USA, 41pp.

Broken Hill Proprietary (BHP) (2012b). Final report on seismic interpretation. Unpublished technical report, Housten, USA, 40pp.

Carniel, R., Jolis, E. M. and Jones, J. (2010). A geophysical multi-parametric analysis of hydrothermal activity at Dallol, Ethiopia. *J. Afr. Earth Sci*. **58:** 812-819.

Chorowicz, J. (2005). The East African rift system. *J. Afr. Earth Sci*. **43**: 379-410.

Chu, D. and Gordon, R. G. (1998). Current plate motions across the Red Sea. *Geophys. J. Int*. **135**: 315-328.

Circum Minerals Potash Ltd. (CMP) (2015). Interpretation of seismic data from the Dallol area. Unpublished technical report, CMP, Addis Ababa, Ethiopia, 24PP.

Clynne, M. A., Duffield, W. A., Fourneir, R. O., Woldegiorgis, L., Janik, C. J., Kahsai, G., Lowenstern, J. B., Weldemariam, K., Smith, J. G. and Tesfai, T. (2005). A Geological and Geochemical Reconnaissance of the Alid Volcanic Center, Eritrea, East Africa. **In:** *Proceedings World Geothermal Conference*. Antalya, Turkey.

Chatterjee, R. S. (2003). Structural pattern of Holenarsipur Supracrustal Belt, Karnataka, India as observed from digitally enhanced high resolution multi-sensor optical remote sensing data aided by field survey. *Intl. J. Appl. Earth Obser. Geoinform.* **4**: 195-215.

Cochran, J. R. and Martinez, F. (1988). Evidence from the northern Red Sea on the transition from continental to oceanic rifting. *Tectonophysics*. **153**(1-4):25-53.

Collet, B., Taud, H., Parrot, J. F., Bonavia, F. and Chorowicz, J. (2000). A new kinematic approach for the Danakil block using a Digital Elevation Model representation. *Tectonophysics*. **316**: 343-357.

Corti, G. (2009). Continental rift evolution: from rift initiation to incipient break-up in the Main Ethiopian Rift, East Africa. *Earth-Sci. Rev*. **96**: 1-53.

Corti, G., Bastow, I. D., Keir, D., Pagli, C. and Baker, E. (2015). Rift related morphology of the Afar Depression. World Geomorphological Landscape, Editor: Billi, P. *Landscape and Landforms of Ethiopia*, Springer Science + Business Media, Dordrecht. 251-274.

Courtillot, V. (1982). Propagating rifts and continental breakup. *Tectonics.* **1**: 239-250.

Courtillot, V., Achache, J., Landre F., Bonhommet, N., Montigny, R., and Féraud, G. (1984). Episodic spreading and rift propagation: new paleomagnetic and geochronologic data from the Afar nascent passive margin. *J. Geophys. Res*. **88**: 3315-3333.

Courtillot, V., Armijo, R. and Tapponnier, P. (1987). Kinematics of the Sinai triple junction and a two-phase model of Arabia-Africa rifting. Editors: Coward, M.P., Dewey, J. F. & Hancock, P. L. Continental Extensional Tectonics. *Geological Society Special Publication*, London. 559-573.

Courtillot, V., Galdeano, A. and Le Mouel, J.L. (1980). Propagation of an accreting plate boundary: a discussion of new aeromagnetic data in the gulf of Tadjoura and Southern Afar. *Earth Planet. Sci. Lett.* **47**: 144-160.

d'Acremont, E., Leroy, S., Beslier, M.O., Bellahsen, N., Fournier, M., Robin, C., Maia, M. and Gente, P. (2005). Structure and evolution of conjugate passive margins of the eastern Gulf of Aden from seismic reflection data. *Geophys. J. Int.* **160:** 869–890.

Darrah, T. H., Tedesco, D., Tassi, F., Vaselli, O., Cuoco, E and Poreda, R. J. (2013). Gas Chemistry of the Dallol Region of the Danakil Depression in the Afar region of the northern-most East African Rift. *Chem. Geol.* **339**:16-29.

Dauteuil, O., Huchon, P., Quemeneur, F., and Souriot, T. (2001). Propagation of an oblique spreading centre: the western Gulf of Aden. *Tectonophysics*. **332**: 423-442.

Doubre, C., Manighetti, I., Dorbath, C. and Bertil, D. (2007). Crustal structure and magmato-tectonic processes in an active rift (Asal-Ghoubbet, Afar, East Africa): 2. Insights from the 23-year recording of seismicity since the last rifting event. *J. Geophys. Res*. **112**: B05406.

Drury, S. A. (1993). *Image interpretation in geology*. Chapman and Hall, London,

Duffield, W. A., Bullen, T. D., Clynne, M. A., Fournier, R. O., Janik, C. J., Lanphere, M. A., Lowenstern, J. G., WeldeGiorgis, L., Kahsai, G., W/Mariam, K., and Tesfai, T. (1997). Geothermal potential of the Alid volcanic center, Danakil Depression, Eritrea. *US Geological Survey Open-File Report*. 97–291 pp.

Eagles, G., Gloaguen, R. and Ebinger, C. (2002). Kinematics of the Danakil microplate. *Earth Planet. Sci. Lett.* **203**: 607-620.

Ebinger, C. J., and Hayward, N. J. (1996). Soft plates and hot spots: Views from Afar. *Journal of Geophysical Research: Solid Earth*. **101**: 21859-21876.

Ebinger, C., Atalay Ayele, Keir, D., Rowland, J., Gezahegn Yirgu, Wright, T., Manahloh Belachew and Hamling, I. (2010). Length and Timescales of Rift Faulting and Magma Intrusion: The Afar Rifting Cycle from 2005 to Present. *Annu. Rev. Earth Planet. Sci*. **38**: 437-464.

Ebinger, C. J., Keir, D., Atalay Ayele, Calais, E., Wright, T. j., Manahloh Belachew, Hammond, J. O. S., Campbell, E. and Buck, W. R. (2008). Capturing magma intrusion and faulting processes during continental rupture: seismicity of the Dabbahu (Afar) rift. *Geophys. J. Int.* **174**:1138–1152.

Fazzini, M., Bisci, C., and Bill, P. (2015). The climate of Ethiopia. World Geomorphological Landscape, Editor: Billi, P. *Landscape and Landforms of Ethiopia*, Springer Science + Business Media, Dordrecht. 65-88.

Ferguson, D. J., Maclennan, J., Bastow, I. D., Pyle, D. M., Jones, S. M., Keir, D., Blundy, J. D., Plank, T. and Gezahegn Yirgu. Melting during late-stage rifting in Afar is hot and deep. (2013). *Nature Lett*. **499**: 70-74.

Field, L., Blundy, J., Calvert, A., and Gezahegn Yirgu. (2013). Magmatic history of Dabbahu, a composite volcano in the Afar rift, Ethiopia, *Geol. Soc. Am. Bull*. **125**: 128-147.

Field, L., Barnie, T., Blundy, J., Brooker, R. A., Keir, D., Elias Lewi and Saunders, K. (2012). Integrated field, satellite and petrological observations of the November 2010 eruption of Erta Ale. *Bull. Volc.* **74**: 2251-2271.

Franzson H., Helgadóttir, H. M. and Óskarsson, F. (2015). Surface exploration and first conceptual model of the Dallol geothermal area, northern Afar, Ethiopia. **In:** *Proceedings World Geothermal Congress*, pp. 1-11. Melbourne, Australia.

Foubert, A., Jaramillo-Vogel D., Eisenhauer, A., Schaegis, J. Balemwal Atnafu and Tesfaye Kidane (2015). Coral reefs and microbial deposits in an active rift setting: insights from the Danakil Depression (Afar, Ethiopia). **In**: *Proceedings of the 15th Bathurst Meeting*, pp. 53-54. Edinburgh, UK.

Gad, S. and Kusky, T. (2006). Lithological mapping in the Eastern Desert of Egypt, the Barramiya area, using Landsat thematic mapper (TM). *J. Afr. Earth Sci*. **44**: 196-202.

Garba, S. I. and Bhaskar, A. (2015). Mapping of hydrothermal altered mineral zones by multispectral and hyper-spectral data analysis -a Case study of Bauchi, Nigeria. *Intl. J. Earth Sci. engineer*. **08**: 550-556.

Gezahegn Yirgu, Ebinger, C. and Maguire, P. K. H. (2006). The Afar volcanic province within the East African Rift system: introduction. *Geol. Soc. Lond. Spec. Publ*. **259**: 1-6.

Gibson, I. L. and Tazieff, H. (1970). The structure of Afar and the northern part of the Ethiopian Rift. *Phil. Trans. Roy. Soc. Lond. A.* **267**: 331-338.

Gonfiantini, R., Bosri, S., Ferrari, G. and Panichi, C. (1973). Isotopic composition of waters from the Danakil Depression (Ethiopia). *Earth & Planet. Sci. Lett*. **18**: 13-21.

Gül, M., Gürbüz, K., and Kalelioğlu, Ö. (2012). Lithology Discrimination in Foreland Basin with Landsat TM. *J. Indian Soc. Remote Sens.***40**: 257-269.

Gupta, R. (2003). *Remote Sensing Geology, 2nd ed*. Berlin Heidelberg: Springer-Verlag, 655 pp.

Gupta, A. and Scholz, C. H. (2000). Brittle strain regime transition in the Afar depression: Implications for fault growth and seafloor spreading. *Geology*. **28**: 1087-1090.

Hamling, I. J., Ayele, A., Bennati, L., Calais, E., Ebinger, C. J., Keir, D. and, Gezahegn Yirgu. (2009). Geodetic observations of the ongoing Dabbahu rifting episode: new dyke intrusions in 2006 and 2007. *Geophysical Journal International*. **178**: 989-1003.

Hammond, J. O. S. (2011). The nature of the crust beneath the Afar triple junction: Evidence from receiver functions. *Geochem. Geophys. Geosyst.* **12**: Q12004.

Hayward, N. J. and Ebinger, C. J. (1996). Variations in the along axis segmentation of the Afar Rift system. *Tectonics*. **15**: 244-257.

Hébert, H., Deplus, C., Huchon, P., Khanbari, K. and Audin, L. (2001). Lithospheric structure of a nascent spreading ridge inferred from gravity data: The western Gulf of Aden. *J. Geophys. Res.* **106**: 26,345-26,363.

Hofmann, C., Courtillot, V., Feráud, G., Rochette, P., Gezahegn Yirgu, Endale Ketefo and Pik, R. (1997). Timing of the Ethiopian flood basalt event and implications for plume birth and global change. *Nature*. **389**: 838-841.

Hofstetter, R. and Beyth, M. (2003). The Afar Depression: interpretation of the 1960-2000 earthquakes. *Geophys. J. Int*. **155**: 715-732.

Holwerda, J. G. and Hutchinson, R. W. (1968). Potash-bearing evaporites in the Danakil area, Ethiopia. *Econ. Geol.* **63**: 124-150.

Horsefield, W. T. (1980). Contemporaneous movement along crossing conjugate normal faults. *J. Struc. Geol.* **2**: 305-310.

http://accuweather.com/en/et/dalol/126842 accessed on 10.10.2016

http://earthexplorer.usgs.gov accessed on 06.03.2016.

http://landsat.usgs.gov/about_ldcm.php accessed on 06.03.2016.

http://landsat.usgs.gov/ldcm_vs_previous.php accessed on 06.03.2016.

http://www.yongtechnology.com/ accessed on 06.04.2016.

Hutchinson, R. W. and Engels, G. G. (1970). Tectonic significance of regional geology and evaporite lithofacies in northeastern Ethiopia. *Phil. Trans. Roy. Soc. Lond. A.* **267**: 313-329.

Jaramillo-Vogel D., Foubert, A., Schaegis, J. Balemwal Atnafu and Tesfaye Kidane (2015). The nature and significance of microbialites deposited in the Danakil Depression. **In**: *Proceedings of the 15th Bathurst Meeting*, pp. 53-54. Edinburgh, UK.

Johanson, D. C. and Taieb, M. (1976). Plio-Pleistocene hominid discoveries in Hadar, Ethiopia. *Nature*. **260**: 293-297.

Jones, J., Carniel, R., Harris, J. L. A. and Malone, S. (2006). Seismic characteristics of variable convection at Erta 'Ale lava lake, Ethiopia. *Volcanol. and Geotherm. Res.* **153**: 64-79.

Kalb, J. (2001). *Adventures in the bone trade: the race to discover human ancestors in Ethiopia's Afar Depression*. Springer-Verlang, Berlin, 389 pp.

Kamb, W. B. (1959). Ice petrofabric observations from Blue Glacier, Washington in relation to theory and experiment. *J. Geophys. Res.* **64**: 1891–1909. For contour

Kamel, M., Youssef, M., Hassan, M, and Bagash, F. (2016). Utilization of ETM+ Landsat data in geologic mapping of wadi Ghadir-Gabal Zabara area, Central Eastern Desert, Egypt. *Egypt. J. Remote Sens. Space Sci*. **19**: 343-360.

Keir, D., Bastow, I. D., Corti, G., Mazzarini, F. and Rooney, T. O. (2015). The origin of along-rift variations in faulting and magmatism in the Ethiopian Rift. *Tectonics*. **34**: 464-477.

Keir, D., Bastow, I. D. Pagli, C. and Chambers, E. L. (2013). The development of extension and magmatism in the Red Sea rift of Afar. *Tectonics*. **607**: 98-114.

Keir, D., Hamling, I.J., Atalay Ayele, Calais, E., Ebinger, C., Wright, T. J., Jacques, E., Kassim Mohamed, Hammond, J.O.S., Manahloh Belechew, Baker, E., Rowland, J.V., Elias Lewi and Bennati, L. (2009). Evidence for focused magmatic accretion at segment centers from lateral dike injections captured beneath the Red Sea rift in Afar. *Geology*, **37**(1): 59-62.

Klaus, R. (2015). Coral Reefs and Communities of the Central and Southern Red Sea (Sudan, Eritrea, Djibouti, and Yemen). *The Red Sea*, Editor(s): Rasul, N. M. A. and Stewart, I. C. F., Springer-Verlang, Berlin. 409-451.

Lillesand, T. M., and Kiefer, R. W. (1994). *Remote sensing and image interpretation*, 3rd ed., John Wiley and Sons, Inc, New York, 750 pp.

Manahloh Belachew, Ebinger, C. and Coté, D. (2013). Source mechanisms of dike-induced earthquakes in the Dabbahu-Manda Hararo rift segment in Afar, Ethiopia: implications for faulting above dikes. *Geophys. J. Int.* **192**: 907-917.

Manahloh Belachew, Ebinger, C., Coté, D., Rowland, J. V., Hammond, J. O. S. and Atalay Ayele. (2011). Comparison of dike intrusions in an incipient seafloor-spreading segment in Afar, Ethiopia: Seismicity perspectives. *J. Geophys. Res*. **116**: B06405.

Makris, J. and Ginzburg, A. (1987). The Afar Depression: transition between continental rifting and seafloor spreading. *Tectonophysics*. **141**: 199-214.

Manighetti, I., Tapponnier, P., Courtillot, V., Gruszow, S. and Gillot, P. Y. (1997). Propagation of rifting along the Arabia-Somalia plate boundary: The gulfs of Aden and Tadjoura. *Journal of Geophysical Research: Solid Earth,* **102**(B2):2681-2710.

Manighetti, I., Tapponnier, P., Gillot, P. Y., Jacques, E., Courtillot, V., Armijo, R., Ruegg, J. C. and King, G. (1998). Propagation of rifting along the Arabia-Somalia plate boundary: Into Afar. *J. Geophys. Res*. **103**: 4947-4974.

Mansour, A. M. and Madkour, H. A. (2015). Raised Coral Reefs and Sediments in the Coastal Area of the Red Sea. Editors: Rasul, N.M.A. and Stewart, I.C.F. *The Red Sea*, Springer-Verlag, Berlin. 379-393.

Makris, J., & Ginzburg, A. (1987). The Afar Depression: transition between continental rifting and sea-floor spreading. *Tectonophysics*. **141**: 199-214.

Marrett, R. and Allmendinger, R. W. (1990). Kinematic analysis of fault-slip data. *J. Struc. Geol.*. **12**: 973-986.

McKenzie, D. P., Davies, D. and Molnar, P. (1970). Plate tectonics of the Red Sea and East Africa. *Nature*. **226**: 243-248.

Miruts Hagos. (2010). Geochemical and petrographic studies of the volcano-tectonic evolution of northern Afar: implications for the structural setup of the actively expanding Erta'Ale Depression. Unpublished PhD Thesis, Universität wein, Vienna, Austria, 239 pp.

Miruts Hagos, Koeberl, C. and Vries, B. W. (2016). The Quaternary volcanic rocks of the northern Afar Depression (northern Ethiopia): perspectives on petrology, geochemistry, and tectonics. *J. Afr. Earth Sci*. **117**: 29-47.

Mock, C., Arnaud, N. O., Cantagrel, J. M. and Gezahegn Yirgu. (1999). $^{40}Ar/^{39}Ar$ thermochronology of the Ethiopian and Yemeni basements: reheating related to the Afar plume? *Tectonophysics*. **314**: 351-372.

Mohr, P. (1989). Nature of the crust under Afar: new igneous, not thinned continental. *Tectonophysics*. **167**: 1-11.

Moufaddal, W. and Rifaat, A. E. (2006). Identifying geomorphic features between Ras Gemsha and Safaga, Red Sea Coast, Egypt, using remote sensing techniques. *Mar. Sci*. **17**: 105-128.

Mshiu, EE. (2011). Landsat remote sensing data as an alternative approach for geological mapping in Tanzania: a case study in the Rungwe volcanic province, south-western Tanzania. *Tanz. J. Sci.* 37: 26-36.

Mwaniki, M. W., Moeller, M. S. and Schellmann, G. (2015). A comparison of Landsat 8 (OLI) and Landsat 7 (ETM+) in mapping geology and visualizing lineaments: A case study of central region Kenya. In: *Proceedings of the 36th International Symposium on Remote Sensing of Environment*, pp. 897-903. Berlin, Germany.

Nobile, A., Pagli, C., Keir, D., Wright, T. J., Atalay Ayele, Ruch, J. and Acocella, V. (2012). Dike-fault interaction during the 2004 Dallol intrusion at the northern edge of the Erta 'Ale ridge (Afar, Ethiopia). *Geophys. Res. Lett.* **39:** L19305.

Pasyanos, M. E. and Nyblade, A. A. (2007). A top to bottom lithospheric study of Africa and Arabia. *Tectonophysics*. **444**: 27-44.

Pedgley, D. E. (1969). Air temperature at Dallol, Ethiopia. *Met. Mag.* **96**: 265-271.

Peña, S. A and Abdelsalam, M. G. (2006). Orbital remote sensing for geological mapping in southern Tunisia: Implication for oil and gas exploration. *J. Afr. Earth Sci*. **44**: 203-219.

Pour, A. B. and Hashim, M. (2015). Hydrothermal alteration mapping from Landsat-8 data, Sar Cheshmeh copper mining district, south-eastern Islamic Republic of Iran. *J. Taibah Univ. for Sci.* **9**: 155-166.

Pugh, D. T. and Abdualnaja, Y. (2015). Sea-level change. *The Red Sea*, Editor(s): Rasul, N. M. A. and Stewart, I. C. F., Springer-Verlang, Berlin. 317-328.

Pürschel, M., Gloaguen, R. and Stadler, S. (2013). Geothermal activities in the Main Ethiopian Rift: Hydrogeochemical characterization of geothermal waters and geothermometry applications (Dofan-Fantale, Gergede-Sodere, Aluto-Langano). *Geothermics*. **47**: 1-12.

Qaid, A. M and Basavarajappa, H. T. (2008). Application of Optimum Index Factor Technique to Landsat-7 Data for Geological Mapping of North East of Hajjah, Yemen. *American-Eurasian J. Sci. Res.***3**: 84-91.

Raharimahefa, T. and Kusky, T. M. (2006). Structural and remote sensing studies of the southern Betsimisaraka Suture, Madagascar. *Gondw. Res*. **10**: 186-197.

Redfield, T. F., Wheeler, W. H., and Often, M. (2003). A kinematic model for the development of the Afar Depression and its paleogeographic implications. *Earth and Planetary Science Letters.* **216**: 383-398.

Rohling, E. J., Foster, G. L., Grant, K. M., Marino, G. Roberts, A. P., Tamisiea, M. E. and Williams, F. (2009). Sea-level and deep-sea-temperature variability over the past 5.3 million years. *Nature*. 508: 477-481.

Rowland, J. V., Baker, E., Ebinger, C. J., Keir, D., Tesfaye Kidane, Biggs, J., Hayward, N. and Wright, T. J. (2007). Fault growth at a nascent slow-spreading ridge: 2005 Dabbahu rifting episode, Afar. *Geophys. J. Int*. **171**: 1226-1246.

Saadi, N. M. and Watanabe, K. (2008). Assessing image processing techniques for geological mapping: a case study in Eljufra, Libya. *Geocarto International*. **24**: 241-253

Sabins, F. F. (1999). Remote sensing for mineral exploration. *Ore Geology Reviews*. **14**: 157-183

Samson Tesfaye, Harding, D. J. and Kusky, T. M. (2003). Early continental breakup boundary and migration of the Afar triple junction, Ethiopia. *Geol. Soc. Am. Bull.* **115**: 1053-1067.

Schaegis, J-C., Foubert, A., Jaramillo-Vogel, D., Ermias Filfilu, Perrochet, L., Balemwal Atnafu and Tesfaye Kidane. (2016). Characterization of a hypersaline lake in an active rift setting: Lake Afdera in the Danakil basin (NE Afar, Ethiopia). **In**: *Proceedings of the 24th meeting of Swiss Sedimentologists*, pp. 36. Fribourg, Switzerland.

Seleshi Bekele, Aster Denekew, Makonnen Loulseged, Loiskandl W, Mekonnen Ayana and Tena Alamirew (2007). Water resources and irrigation development in Ethiopia. Unpublished Working Paper 123, International Water Management Institute, Colombo, 78 pp.

Simon, N., Ali, C. A., Mohamed, K. R. and Sharir, K. (2016). Best band ratio combinations for the lithological discrimination of the Dayang Bunting and Tuba Islands, Langkawi, Malaysia. *Sains Malaysiana*. **45**: 659–667.

Skovitina, T. M., Lebedeva, E. V., Shchetnikov A. A., Selezneva, E. V., E. V., Angelelli, F. and Mikhalev, D. V. (2012). Morphological Landscapes of Ethiopia. *Geog. & Natur. Res.* **33**(3): 246-251.

Solomon, S. and Ghebreab, W. (2006). Lineament characterization and their tectonic significance using Landsat TM data and field studies in the central highlands of Eritrea. *J. Afr. Earth Sci*. **46**: 371-378.

Souriot, T. and Brun, J.P. (1992). Faulting and block rotation in the Afar triangle, East Africa: The Danakil "crank-arm" model. *Geology*. **20**: 911-914.

Stab, M., Bellahsen, N., Pik, R., Quidelleur, X., Dereje Ayalew and Leroy, S. (2015). Modes of rifting in magma-rich settings: Tectonomagmatic evolution of Central Afar.

American Geophysical Union. Retrieved from http://onlinelibrary. wiley.com /doi/10. 1002/2015TC003893/pdf on 01.10.2016.

Stern, R. J. (1994). Arc Assembly and continental collision in the Neoproterozoic East African Orogen: Implications for the consolidation of Gondwanaland. *Annu. Rev. Eart Planet. Sci*. **22:**319-321.

Sultan, M., Arvidson, R. E., Sturchio, N. C. and Guiness, E. A. (1987). Lithological mapping in arid regions with Landsat thematic mapper data: Meatiq DOM, Egypt. *Geol. Soc. Am. Bull*. **99**: 748–762**.**

Tadiwos Chernet (2012). Dallol Volcano and Danakil Depression, Ethiopia. In: *Magmatic Rifting and Active Volcanism Conference*, pp. 11-13, Addis Ababa, Ethiopia.

Talbot, C. J. (2008). Hydrothermal salt – but how much? *Mar. & Petrol. Geol*. **25**: 191-202.

Tapponnier, P., Armijo, R., Manighetti, I., and Courtillot, V. (1990). Bookshelf faulting and horizontal block rotations between overlapping rifts in southern Afar. *Geophy. Res. Lett.* **17**: 1-4

Thurmond, A. K., Abdelsalam, M. G. and Thurmond, J. B. (2006). Optical-radar-DEM remote sensing data integration for geological mapping in the Afar Depression, Ethiopia. *J. Afr. Earth Sci*. **44**: 119-134.

Tilahun Mammo (2004). Mapping the crust-mantle boundary beneath Afar Depression, *Gondw. Res*. **3**: 855-861.

United Nations Development Program (UNDP) (1973). Geology, geochemistry, and hydrology of hot springs of the East African Rift System within Ethiopia. Unpublished technical report, UNDP, New York, USA, 274 pp.

United States Geological Survey (USGS) (2016). Landsat 8 (L8) data user's handbook. Retrieved from http://landsat.usgs.gov/l8handbook.php on 19.09.2016.

Van deer Meer, F. D., van der Werff, H. M. A., van Ruitenbeek, F. J. A. Hecker, C. A. Bakker, W. H., Noomen, M. F., van der Meijde, M., Carranza, E. J. M., de Smeth, J. B. and Woldai, T. (2012). Multi- and hyperspectral geologic remote sensing: A review. *Intl. J. App. Earth Obser. Geoinfor.* **14**: 112–128.

Varet, J. (2006). The Afar triangle, a future "gulf region" for geothermal energy? I**n:** *Proceedings of the 1st African Rift Geothermal Conference*, pp. 7-13. Addis Ababa, Ethiopia.

Varet, J. (2010). Contribution to favorable geothermal site selection in Afar triangle. **In:** *Proceedings of the 3rd African Rift Geothermal Conference*, pp. 139-155. Djibouti, Djibouti.

Varet, J. and Gasse, F. (1978). Geology of central and southern Afar (Ethiopia and Djibouti Republic). *CNRS, Paris,* pp. 118.

Varet, J., Tadiwos Chernet, Girma Weldetinsae and Arnason, K. (2012). Exploring for geothermal sites in northern and central Afar (Ethiopia). **In:** *Proceedings of the 4th African Rift Geothermal Conference*. Nairobi, Kenya.

Vye-Brown, C., Sparks, R. S. J., Elias Lewi, Getnet Mewa, Asfawossen Asrat, Loughlin, S. C., Meek, K. and Wright, T. J. (2016). Ethiopian volcanic hazards: a changing research landscape. *Magmatic rifting and active volcanism*, Editors: Wright, T. J., Atalay Ayele., Ferguson, D. J., Tesfaye Kidane and Vye-Brown, C. Geological Society, London, Special Publications. **420**:

Waltham, T. (2005). Extension tectonics in the Afar triangle. *Geology Today*. **21**: 101-107.

Wang, Z., Erb, A. M., Schaaf, C. B., Sun, Q., Liu, Y., Yang, Y., Shuai, Y., Casey, K. A. and Román, M. O. (2016). Early spring post-fire snow albedo dynamics in high latitude boreal forests using Landsat-8 OLI data. *Remote Sensing of Environment*. **185**; 1-13

Warren, J. K. (2016). *Evaporites: a geological compendium, 2nd ed.*, Springer, Berlin, 1813 pp.

White, T. D., Suwa, G. and Berhane Asfaw. (1994). Australopithecus ramidus, a new species of early hominid from Aramis, Ethiopia. *Nature*. **371**: 306-312.

Williams, F. M. (2016). *Understanding Ethiopia: Geology and Scenery*. Springer, Berlin, 343 pp.

Winter, J. D. (2001). *An introduction to igneous and metamorphic petrology, 4th ed*., Prentice Hall, New Jersey, 697 pp.

Wolfenden, E., Ebinger, C., Gezahegn Yirgu, Deino, A. and Dereje Ayalew. (2004) Evolution of the northern Main Ethiopian rift: birth of a triple junction. *Earth Planet. Sci. Lett.* **244**, 213–228.

Wolfenden, E., Ebinger, C., Gezahegn Yirgu, Renne, P. R. and Kelley, S. P. (2005). Evolution of a volcanic rifted margin: Southern Red Sea, Ethiopia. *Geol. Soc. Am. Bull*. **117**: 846–864.

Wright, T. J., Sigmundsson, F., Pagli, C., Manahloh Belachew, Hamling, I. J., Brandsdóttir, B., Keir, D., Pedersen, R., Atalay Ayele, Ebinger, C., Einarsson, P., Elias Lewi and Calais, E. (2012). Geophysical constraints on the dynamics of spreading centres from rifting episodes on land. *Nature Geoscience*. **5**: 242-250.

Wright, T. M., Ebinger, C., Biggs, J., Atalay Ayele, Gezahegn Yirgu, Keir, D. and Stork, A. (2006). Magma-maintained rift segmentation at continental rupture in the 2005 Afar dyking episode. *Nature Lett*. **442**: 291-294.

www.csa.gov.et/images/documents/pdf_files/nationalstatisticsabstract/2006/total.pdf accessed on 04.02.2016.

www.csa.gov.et/images/documents/pdf_files/nationalstatisticsabstract/2007/2007%20population.pdf accessed on 04.02.16.

Yasin Mohammed (2008). Political history of the Afar in Ethiopia and Eritrea. *Afrika Spectrum*. **42**: 39-65.

Zeresenay Alemseged, Wynn, J. G., Kimbel, W. H., Reed, D., Geraads, D. and Bobe, R. (2005). A new hominin from the Basal Member of the Hadar Formation, Dikika, Ethiopia, and its geological context. *J. Hum. Evol.* **49**: 499-514.

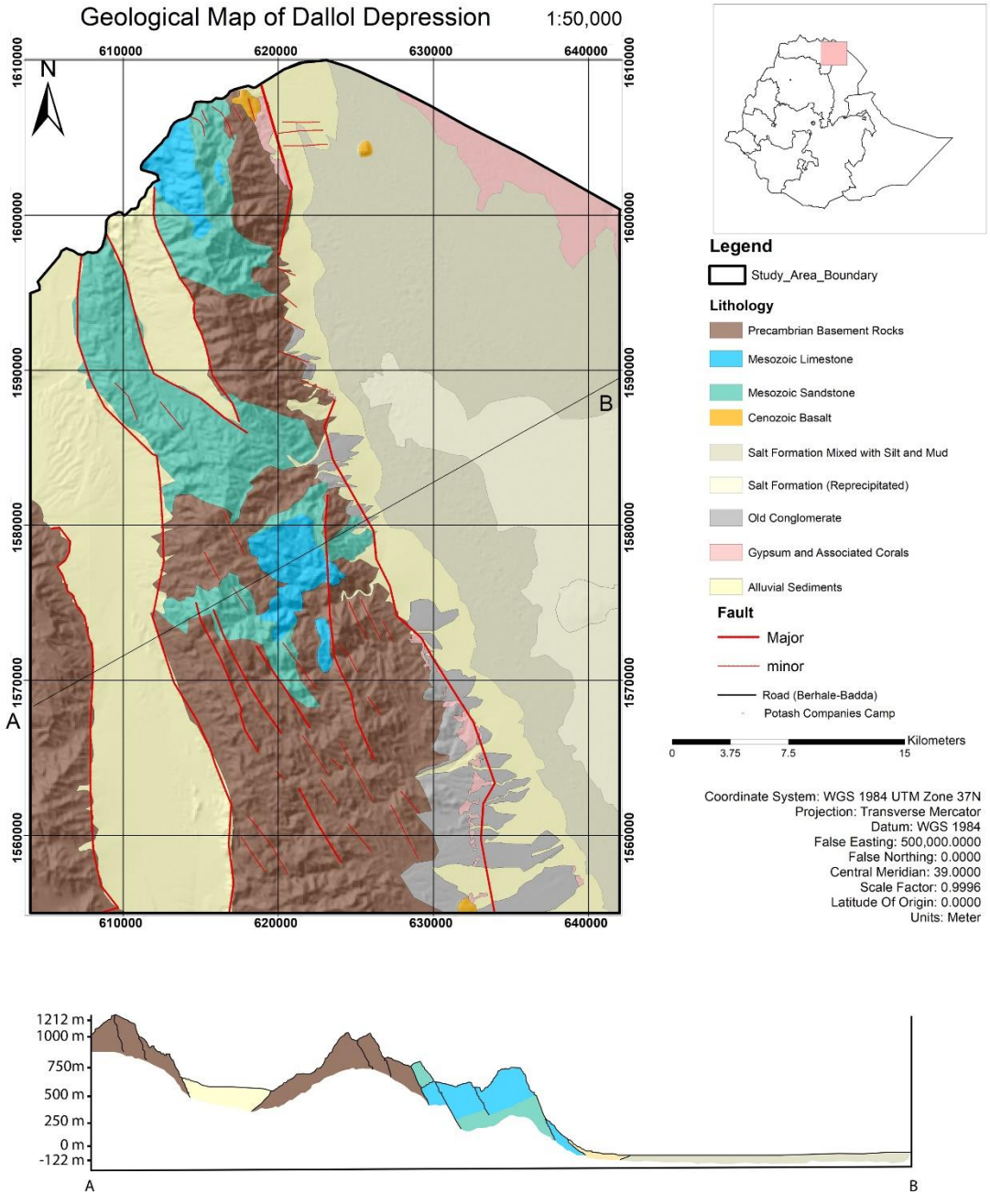
Geological Map of Dallol Depression
1:50,000
610000
620000
630000
640000
1610000
1600000
1590000
1580000
1570000
1560000
N
A
B
Legend
Study_Area_Boundary
Lithology
Precambrian Basement Rocks
Mesozoic Limestone
Mesozoic Sandstone
Cenozoic Basalt
Salt Formation Mixed with Silt and Mud
Salt Formation (Reprecipitated)
Old Conglomerate
Gypsum and Associated Corals
Alluvial Sediments
Fault
Major
minor
Road (Berhale-Badda)
Potash Companies Camp
Kilometers
0
3.75
7.5
15
Coordinate System: WGS 1984 UTM Zone 37N
Projection: Transverse Mercator
Datum: WGS 1984
False Easting: 500,000.0000
False Northing: 0.0000
Central Meridian: 39.0000
Scale Factor: 0.9996
Latitude Of Origin: 0.0000
Units: Meter
1212 m
1000 m
750m
500 m
250 m
0 m
-122 m
A
B

Structural Map of Dallol Depression

1:50,000

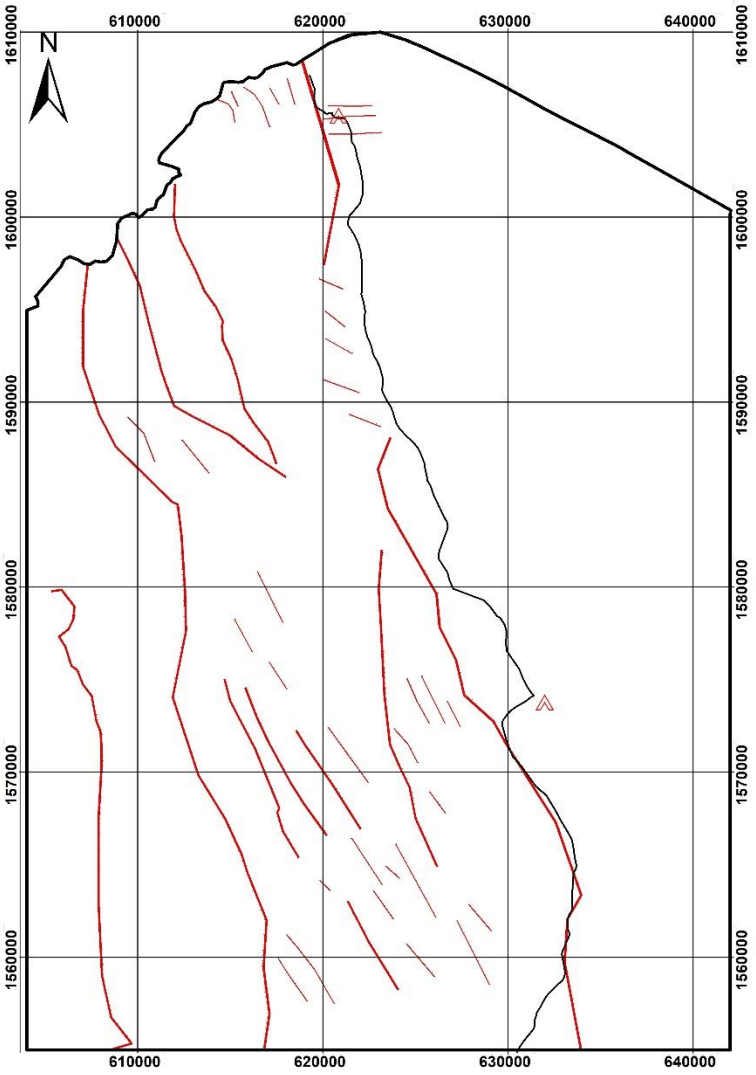

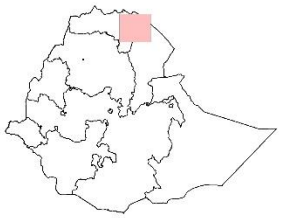

Legend

Study_Area_Boundary

Fault

Major

minor

Road (Berhale-Badda)

Potash Companies Camp

Kilometers

0 3.75 7.5 15

Coordinate System: WGS 1984 UTM Zone 37N
Projection: Transverse Mercator
Datum: WGS 1984
False Easting: 500,000.0000
False Northing: 0.0000
Central Meridian: 39.0000
Scale Factor: 0.9996
Latitude Of Origin: 0.0000
Units: Meter

Appendix A

Observation Points

Observation Points				
No.	**Easting**	**Northing**	**Remark**	**Note**
1	632164	1555488	Basalt exposure encrusting coral reefs and associated gypsum	CO1
2	632431	1555871	Gypsum covering coral reefs	Close to CO1
3	633122	1556095	Coral Reef	CO7
4	623873	1578782	Phyllite Exposure	
5	619550	1604396	Gypsum Canyon	crack measurement taken
6	618746	1606854	Basalt exposure forming escarpment	Close by Fault 2
7	632371	1566128	Gypsum associated with subsidence	
8	619283	1606862	Lacustrine sediment	Close by Fault 3
9	618286	1606172	Basalt exposure encrusting coral reefs	CO21
10	620233	1605590	Volcaniclastic	Pyroclastic fall deposit
11	620326	1605469	Volcaniclastic	Pyroclastic fall deposit
12	629435	1571329	Gypsum	Close by Fault 6
13	629288	1571117	Old Conglomerate	Close by CO27
14	632090	1560093	Old Conglomerate	Close by Fault 8
15	623089	1588392	Slate	
16	623089	1588392	Slate	Close by CO28
17	620652	1599162	Gypsum	Close by CO29
18	630558	1559298	Old Conglomerate	Close by Abandoned Mn Mine
19	632234	1560403	Coral Reef	CO4
20	632428	1560684	Gypsum	CO4
21	619175	1603343	Slate	Close by CO19
22	621698	1596092	Recent Alluvial	Alluvial Fan
23	621698	1596092	Recent Alluvial	Alluvial Fan
24	631593	1572309	Recent Alluvial	Alluvial fan
25	636312	1561289	Recent Alluvial	Alluvial Fan
26	639415	1571448	Salt	Dallol Mound
27	641088	1565293	Salt	Dallol Mound

Appendix B

Field Structural Measurements

Faults				
No.	**Strike**	**Dip**	**Remark**	**Set**
1	347	67NE	Juxtapose conglomerate and phyllite	1
2	345	70NE	Contain Mineral Growth; this is small fault to follow it above and difficult to characterize; this is not of same time as the mega fault here with grooves	
3	344	70NE	✓ 70 Rake of the mineral growth on this fault plane from 250 strike direction ✓ 40 rake from 307 strike direction ✓ Rake of striation from 185 strike direction is 700	
4	70	72NNW		
5	307	65NE		
6	190	70E	Fault with drag zone	2
7	185	75E		
8	200	75NE		
9	354	73E	✓ with hardened surface along which fluid moved ✓ Affected conglomerate and sandy material above may be lacustrine ✓ the fault has 25m apparent displacement ✓ Measurement taken on the north side of the stream	3
10	5	70E		
11	165	60E		
12	0	70E		
13	170	70E		
14	350	75NE		
15	340	85NE		
16	330	75NE		
17	30	75SE	Small fault within lacustrine sediment	4
18	0	85W	Conjugate fault set	5
19	0	90E		
20	0	85E		
21	N10E	75E		
22	155	65E		
23	150	70SW		
24	160	75SW		
25	145	87SW		
26	N35E	65E		
27	N15E	65E		
28	335	55SW	Fault within inclined conglomerate unit above an angular unconformity	6
29	N-S	80E	Affecting lacustrine sediment of thickness 20 cm	7
30	15	100		
31	100	80E		
32	325	20NE	Affecting lacustrine sediment	8
33	320	90	Affecting basalt	9

Joints					
No.	**Strike**	**Dip**	**Dip Direction**	**Remark**	**Set**
1	N-S	85	E (90)	Affecting basalt unit below CO1	1
2	150	85	60		
3	310	80	220		
4	310	90	220		
5	200	85	110		
6	170	85	80		

Gypsum Cracks					
No.	**Strike**	**Dip**	**Dip Direction**	**Remark**	**Set**
1	140	65SW	230		1
2	90	60	165	Crack affecting Coral Reefs CO7	2
3	110	47	210		
4	305	67	215		
5	140	65	SW (230)	Gypsum Canyon Cracks	
6	325	80	SW (235)		
7	310	85	SW (220)		
8	305	80	SW (215)		
9	315	87	SW (225)		
10	350	80	SW (260)		
11	160	70	SW (250)		
12	330	85	SW (240)		
13	185	79	SW (275)		
14	155	90	SW (245)		
15	165	90	SW (255)		
16	340	85	SW (250)		
17	178	85	SW (268)		
18	340	85	SW (250)		
19	160	87	SW (250)		
20	318	80	SW (228)		
21	300	84	SW (210)		
22	130	75	SW (220)		
23	160	85	SW (250)		
24	330	85	SW (240)		
25	135	72	SW (225)		
26	300	80	SW (210)		
27	140	90	SW (230)		
28	315	85	SW (225)		
29	145	85	SW (235)		
30	325	80	SW (235)		
31	335	80	SW (245)		
32	330	90	SW (240)		
33	350	90	SW (260)		
34	170	80	SW (260)		
35	340	75	SW (250)		
36	325	85	SW (235)		
37	145	75	SW (235)		
38	180	75	W (270)		
39	320	78	SW (230)		
40	320	80	SW (230)		
41	155	90	SW (245)		

Foliations					
No.	**Strike**	**Dip**	**Remark**	**Note**	**Set**
1	30	15SE	phyllitic foliation	Fault 1 area	1
2	120	70SW	Slatey Cleavage		2
3	110	90SW			
4	115	75SW			
5	140	85SW			
6	140	90SW			
7	110	80SW			
8	135	85SW			
9	120	85SW			
10	150	80SW			
11	140	80SW			
12	155	65SW			
13	155	70SW			
14	150	70SW			
15	110	80SW			
16	105	80SW			
17	130	85SW			
18	135	80SW			
19	120	55SW			
20	150	85SW			
21	135	85SW			

Unconformity			
No.	**Strike**	**Dip**	**Remark**
1	N-S	30E	Angular unconformity between 2 conglomerate unit

Appendix C

Trend of Structures Extracted from DEM

No.	Trend	No.	Trend	No.	Trend	No.	Trend	No.	Trend
1	349	8	319	15	327	22	333	29	325
2	337	9	333	16	331	23	334	30	323
3	331	10	325	17	333	24	327	31	311
4	327	11	331	18	347	25	322	32	313
5	350	12	325	19	333	26	335	33	321
6	325	13	326	20	332	27	331	34	329
7	330	14	324	21	320	28	332		

Appendix D

Description of Spectral Bands of Landsat 8 satellite image

Bands	Spatial Resolution	wavelength	Subsystem
1	30	0.433–0.453	VNIR (Coastal Aerosol)
2	30	0.450–0.515	VNIR (Visible Near Infrared)
3	30	0.525–0.600	VNIR (Visible Near Infrared)
4	30	0.630–0.680	VNIR (Visible Near Infrared)
5	30	0.845–0.885	VNIR (Visible Near Infrared)
6	30	1.560–1.660	SWIR (Visible Near Infrared)
7	30	2.100–2.300	SWIR (Visible Near Infrared)
8	15	0.500–0.680	Panchromatic (Visible Near Infrared)
9	30	1.360–1.390	TIR (Thermal Infrared)
10	100	10.30–11.30	TIR (Thermal Infrared)
11	100	11.50–12.50	TIR (Thermal Infrared)

Appendix E

Spectral Reflectance Values for Lithologic Units of the Study Area

Description	B1	B2	B3	B4	B5	B6	B7	B8
Fault 1 (juxtaposing Conglomerate with Phyllite)	11963	11461	11117	11095	11048	12478	11644	11598
NNW to NS Trending Gypsum Cracks	12854	12619	12861	13660	15062	16331	14007	11792
Fault 3 (Basalt unit on top covering the surface there)	12603	12398	12637	13442	14384	14857	12830	11530
Gypsum outcrop associated with subsidence	13657	13754	14534	16525	18545	18792	15141	14298
Coral Outcrop 17	14643	14969	16419	18597	21307	21722	16250	16865
Basalt with few corals	11726	11068	10453	10758	11894	12539	11023	10539
Scoraceous Basalt (Maraho Volcano)	12546	12117	11879	12576	13604	14673	12850	12045
Basaltic lava field near Circum Bada Camp	12022	11323	10691	10776	11532	12011	10856	10575
Phyllite exposure	13863	13867	14381	15235	16509	22098	18988	15473
Alluvial Sediment	12858	12418	12251	12839	13514	14888	13580	12394
Basaltic lava flow	11432	10741	10164	10281	10744	11480	10596	9642
Alluvial Sediment	12979	12604	12654	13010	13531	15790	14791	12873
Salt Plain	21759	23630	25677	28074	30155	9391	7222	26349

Appendix F

Description of faults identified on five different seismic lines

Allana, 2012

Fault	Seismic Line	Horizons affected	Aparent Downthrow direction	Maximum throw (m)
1	AL10-L05	Top of potash 1 **Top of Basement**	NW	25
2	AL10-L05	Top of potash 2 Top of Bischofite **Top of Basement**	SE	105
3	AL10-L05	Top of potash 1 Top of potash 2 Top of Bischofite	NW	5
4	AL10-L05	Top of Potash 1 **Top of Potash 2** Top of Bischofite	NW	10
5	AL10-L05	Top of Kainite Base of Potash 2 **Top of Basement**	SE	25
6	AL10-L02_Part1 AL10-L02_Part1 AL10-L02_Part1 AL10-L02_Part1, AL10-L05 AL10-L02_Part1, AL10-L05 AL10-L02_Part1, AL10-L05	Top of Potash 1 Top of Potash 2 Top of Bischofite Top of Kainite Base of Potash 2 **Top of Basement**	SE	50
7	AL10-L02_Part1, AL10-L05 AL10-L02_Part1, AL10-L05	**Top of Kainite** Base of Potash 2	ESE	10
8	AL10-L02	Top of Kainite Base of Potash 2 **Top of Basement**	NW	15
9	AL10-L02_Part1, AL10-L05 AL10-L02_Part1, AL10-L05 AL10-L02_Part1, AL10-L05	Top of Kainite Base of Potash 2 **Top of Basement**	NW	20
10	AL10-L05	**Top of Potash 1** Top of Potash 2 Top of Bischofite Top of Kainite Base of Potash 2 Top of Basement	SE	15
11	AL10-L05	Top of Potash 2 Top of Bischofite Top of Kainite Base of Potash 2	NW	5
12	AL10-L02	Top of Kainite Base of Potash 2 **Top of Basement**	SE	10
13	AL10-L02_Part1	Top of Potash 1 **Top of Basement**	SW	25
14	AL10-L02_part1	Top of Potash 1 **Top of Potash 2** Top of Bischofite	SW	25
15	AL10-L02_part1	Top of Potash 1 Top of Potash 2 Top of Bischofite **Top of Basement**	SW	55
16	AL10-L02_part1	**Top of Potash 2**	SW	25

		Top of Bischofite Top of Kainite Base of Potash 2		
17	AL10-L02_part1	Top of Potash 1 **Top of Potash 2** Top of Bischofite	SW	15
18	AL10-L01_part1	Top of Potash 2 Top of Bischofite Top of Kainite Base of Potash 2 **Top of Basement**	NE	65
19	AL10-L01	Top of Basement	SW	5
20	AL10-L01	Top of Potash 2 Top of Bischofite Top of Kainite Base of Potash 2 Top of Potash 3 **Top of Basement**	NE	60
21	AL10-L01	Top of Potash 2 Top of Bischofite Top of Kainite Base of Potash 2 **Top of Potash 3** Top of Basement	NE	70
22	AL10-L01	Top of Potash 2 Top of Bischofite Top of Kainite **Base of Potash 2** Top of Potash 3 Top of Basement	NE	25
23	AL10-L01	Top of Potash 2 Top of Bischofite	SW	20
24	AL10-L01	Top of Potash 2 Top of Bischofite Top of Kainite Base of Potash 2 **Top of Potash 3** Top of Basement	SW	90
25	AL10-L01	Top of Potash 3 Top of Basement	SE	20
26	AL10-L01	Top of Potash 3 Top of Basement	NE	20
27	AL10-L01	**Top of Potash 3** Top of Basement	SW	20
28	AL10-L01	Top of Potash 3	SW	20
29	AL10-L01	Top of Basement	SW	5
30	AL10-L01	Top of potash 3 Top of Basement	NE	25
31	AL10-L01_part2	Top of Potash 2 Top of Bischofite Top of Kainite Base of Potash 2 **Top of Potash 3** Top of Basement	NE	30
32	AL10-L01_part2	**Top of Potash 2** **Top of Bischofite** Top of Kainite Base of Potash 2 Top of Potash 3	NE	35

		Top of Basement		
33	AL10-L01_part2	Top of Potash 2 Top of Bischofite Top of Kainite **Base of Potash 2** Top of Potash 3 Top of Basement	NE	155
34	AL10-L01_part2	Top of potash 3	SE	35
35	AL10-L01_part2	Top of Potash 2 **Top of Bischofite** Top of Kainite Base of Potash 2 Top of Potash 3	SW	25
36	AL10-L01_part2	**Top of Potash 3** Top of Basement	SW	65
37	AL10-L01_part2	Top of Kainite Base of Potash 2 **Top of Potash 3**	SW	20
38	AL10-L04_part2	Top of Potash 2 Top of Bischofite Top of Kainite Base of Potash 2 Top of Potash 3 **Top of Basement**	SW	35
39	AL10-L04	Top of Basement	NW	35
40	AL10-L04	Top of potash 3	NW	20
41	AL10-L04	Top of Potash 2 Top of Bischofite Top of Kainite Base of Potash 2 Top of Potash 3 **Top of Basement**	SE	155
42	AL10-L04	Top of potash 3 **Top of Basement**	SE	30
43	AL10-L04	**Top of Potash 3** Top of Basement	SE	25
44	AL10-L01	Top of potash **Top of Basement**	SE	30
45	AL10-L04	Top of Potash 2 Top of Bischofite Top of Kainite Base of Potash 2 **Top of Potash 3** Top of Basement	NW	70
46	AL10-L03	Top of Potash 3	NW	10
47	AL10-L02_part2	**Top of Bischofite** Top of Kainite	E	30

Appendix G

Geological Map of the Danakil Depression (Northern Afar Ethiopia)

Prepared by Barberi et al. (1973)

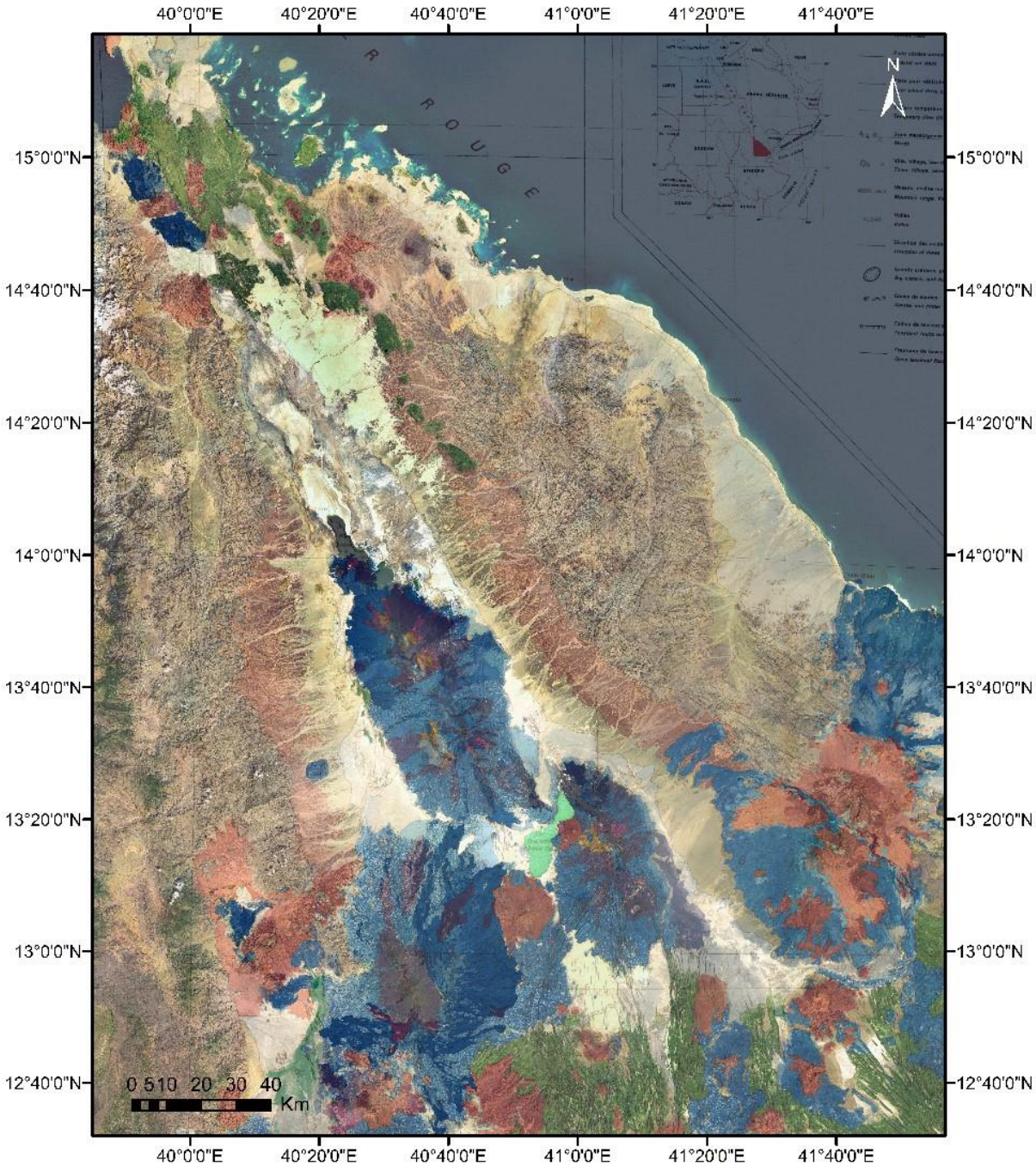

Legend

Part I

Part II

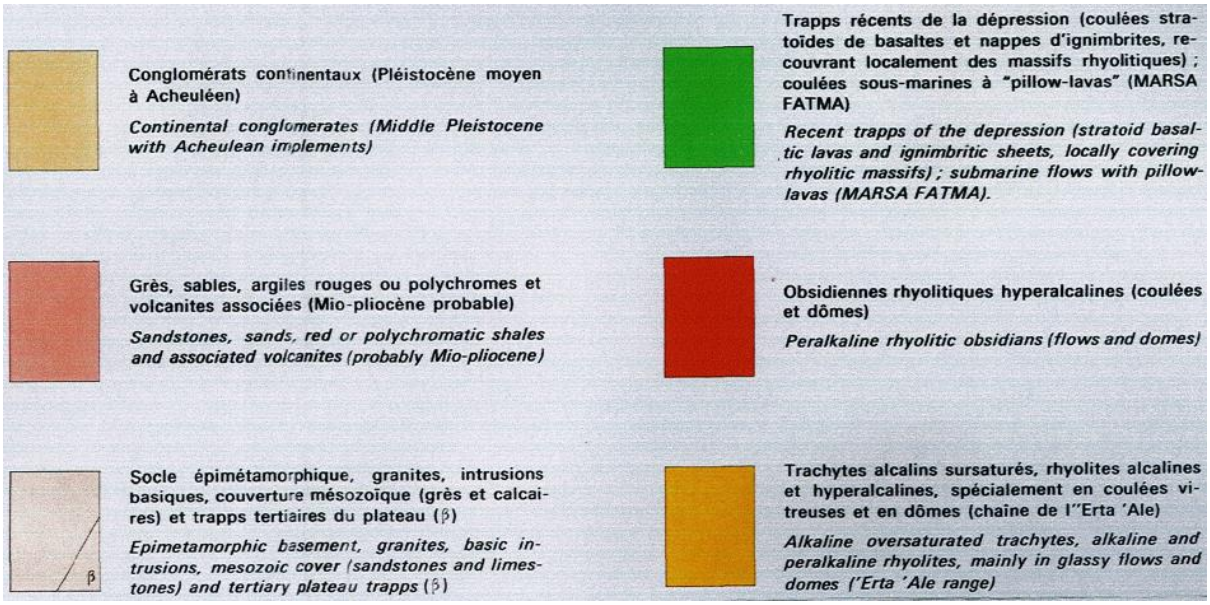
Conglomérats continentaux (Pléistocène moyen à Acheuléen)
Continental conglomerates (Middle Pleistocene with Acheulean implements)
Trapps récents de la dépression (coulées stratoïdes de basaltes et nappes d'ignimbrites, recouvrant localement des massifs rhyolitiques) ; coulées sous-marines à "pillow-lavas" (MARSA FATMA)
Recent trapps of the depression (stratoid basaltic lavas and ignimbritic sheets, locally covering rhyolitic massifs) ; submarine flows with pillow-lavas (MARSA FATMA).
Grès, sables, argiles rouges ou polychromes et volcanites associées (Mio-pliocène probable)
Sandstones, sands, red or polychromatic shales and associated volcanites (probably Mio-pliocene)
Obsidiennes rhyolitiques hyperalcalines (coulées et dômes)
Peralkaline rhyolitic obsidians (flows and domes)
β
Socle épimétamorphique, granites, intrusions basiques, couverture mésozoïque (grès et calcaires) et trapps tertiaires du plateau (β)
Epimetamorphic basement, granites, basic intrusions, mesozoic cover (sandstones and limestones) and tertiary plateau trapps (β)
Trachytes alcalins sursaturés, rhyolites alcalines et hyperalcalines, spécialement en coulées vitreuses et en dômes (chaîne de l''Erta 'Ale)
Alkaline oversaturated trachytes, alkaline and peralkaline rhyolites, mainly in glassy flows and domes ('Erta 'Ale range)

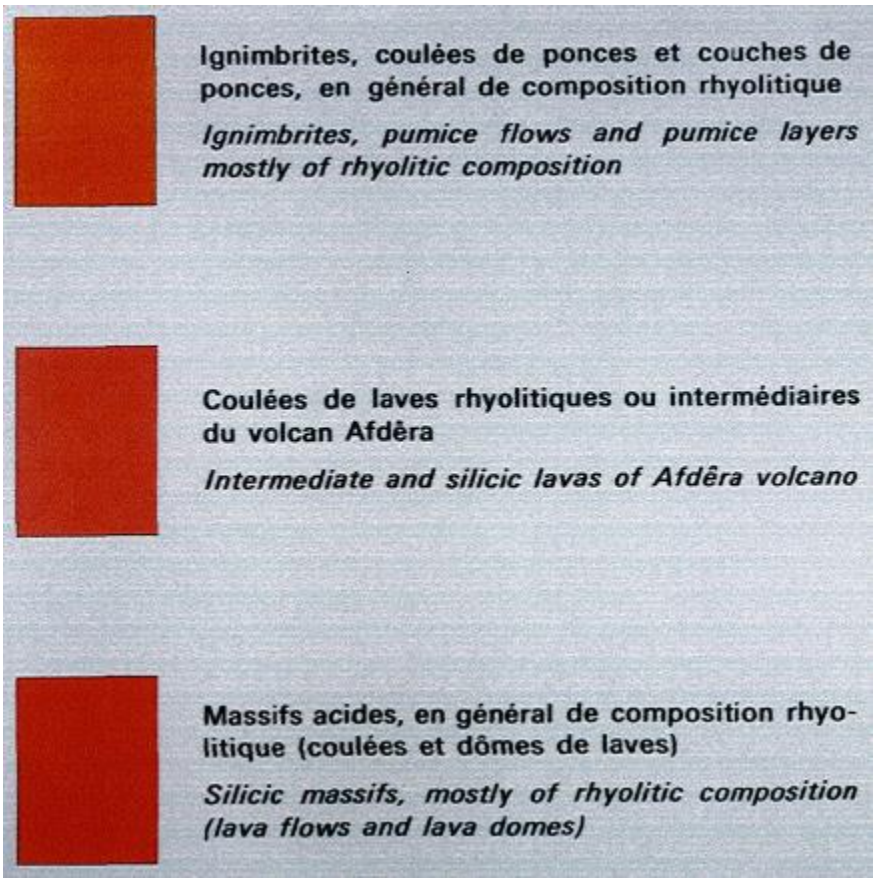
Ignimbrites, coulées de ponces et couches de ponces, en général de composition rhyolitique
Ignimbrites, pumice flows and pumice layers mostly of rhyolitic composition
Coulées de laves rhyolitiques ou intermédiaires du volcan Afdêra
Intermediate and silicic lavas of Afdêra volcano
Massifs acides, en général de composition rhyolitique (coulées et dômes de laves)
Silicic massifs, mostly of rhyolitic composition (lava flows and lava domes)

Appendix H

Red Sea Level Diagram for the Period from 200ka to the Present

Rohling et al., 2009